이학박사학위논문

Application of a Linked Methodology for Probabilistic Evaluation of Three-Dimensional Carbon Dioxide Storage Capacities: A Case Study of the Pohang Basin, Korea

삼차원 이산화탄소 저장 용량의 확률론적 평가를 위한 연계 방법론의 적용: 한국 포항분지 사례연구

2019년 2월

서울대학교 대학원

지구환경과학부

박 재 용

Application of a Linked Methodology for Probabilistic Evaluation of Three-Dimensional Carbon Dioxide Storage Capacities: A Case Study of the Pohang Basin, Korea

지도교수 이준기

이 논문을 이학박사학위논문으로 제출함
2019년 1월

서울대학교 대학원
지구환경과학부
박재용

박재용의 박사학위논문을 인준함
2019년 1월

위원장 이강근 (인)
부위원장 이준기 (인)
위원 김덕진 (인)
위원 김중희 (인)
위원 김영희 (인)

Abstract

Application of a Linked Methodology for Probabilistic Evaluation of Three-Dimensional Carbon Dioxide Storage Capacities: A Case Study of the Pohang Basin, Korea

Jai-Yong Park
School of Earth and Environmental Sciences
The Graduate School
Seoul National University

The linked methodology is applied to perform probabilistic evaluation of individual gas-, liquid-, supercritical-, and whole fluid-phase carbon dioxide (CO_2) storage capacities. In order to perform probabilistic evaluation of individual gas-, liquid-, supercritical-, and whole fluid-phase CO_2 storage capacities, grid-based geologic formation volume, grid-based CO_2 density, and grid-based CO_2 storage capacity are evaluated through three-dimensional geologic modeling and grid-based Monte Carlo simulation sequentially as the linked methodology. The two clastic saline formations, which are the sandstone-dominant Fluvial Conglomerate and Sandstone (FCSS) and Shallow Marine Sandstone (SMSS) in the Pohang Basin, are selected as the target clastic saline formations. The results of the three-dimensional geologic modeling show that the six geologic formations are distributed very complicatedly both onshore and offshore with irregular depths and thicknesses, and they are partly dissected and offset by the eight major faults. The two clastic saline formations SMSS and FCSS are deep and thick at the three prospective areas such as Areas 1, 2, and 3 in the modeling domain. The results of the grid-based Monte Carlo simulation show the following three main contents. First, in the two clastic saline formations SMSS and FCSS, CO_2 exists as gas, liquid, and supercritical phases with the corresponding distinctive density ranges depending on the pressure and temperature with depth. Second, the theoretical individual gas-, liquid-, supercritical-, and whole fluid-phase CO_2 storage capacities all show asymmetric normal distributions. On the other hand, the effective individual gas-, liquid-, supercritical-, and whole fluid-phase CO_2 storage capacities of the saline formations all show log-normal distributions, and their values are much lower than the values of the theoretical individual gas-, liquid-, supercritical-, and whole fluid-phase CO_2 storage capacities. Third, in the SMSS, the grid-wise (elemental) theoretical and effective fluid-phase CO_2 storage capacities are probabilistically higher at Area 1 (mainly as supercritical and liquid phases), intermediate at Area 2 (mainly as liquid and gas phases), and lower at Area 3 (mainly as a gas phase). However, in the FCSS, the grid-wise theoretical and effective fluid-phase CO_2 storage capacities are probabilistically higher at Area 2 (mainly as supercritical and liquid phases), intermediate at Area 1 (mainly as a supercritical phase), and lower at Area 3 (mainly as a gas phase). Finally, four key criteria (parameters) for selecting or ranking the optimal CO_2 storage locations are decided by summarizing and analyzing the results of the three-dimensional geologic modeling and grid-based Monte Carlo simulation. On the basis of the four key criteria (parameters), the overall suitability ranks of Areas 1, 2, and 3 for geologic CO_2 storage are determined to be the first, second, and third, respectively.

Keywords: carbon dioxide, geologic storage, clastic saline formation, fluid-phase storage capacities, three-dimensional geologic modeling, grid-based Monte Carlo simulation, probabilistic evaluation, Pohang Basin

***Student Number*: 2013-22973**

Contents

List of Tables

List of Figures

1. Introduction

1.1. Global warming and geologic storage of carbon dioxide

Recently, global warming, also referred to as climate change, has emerged as significant global issues in scientific, environmental, economical, social, and political terms. It is hypothesized to be caused by the anthropogenic emissions of greenhouse gases. Atmospheric concentrations of greenhouse gases, such as carbon dioxide (CO_2), methane (CH_4), and nitrous oxide (N_2O), have increased since the 18th-century Industrial Revolution. Among the greenhouse gases, carbon dioxide (CO_2) has been recognized as the most contributive greenhouse gas to these global issues because of its huge amount of emissions into the atmosphere.

Geologic storage of CO_2 has been considered as an effective countermeasure for reducing the rate of CO_2 emissions (Holloway, 1997; Metz et al., 2005). Geologic storage of CO_2 involves sequestration of CO_2 in suitable deep geologic formations. There are several potential geological storage options such as saline formations (aquifers), hydrocarbon (oil and gas) reservoirs, and coal beds (Figure 1.1). Saline formations are defined as porous and permeable sedimentary formations that CO_2 can be injected. Saline formation should be overlain by a thick extensive impermeable cap

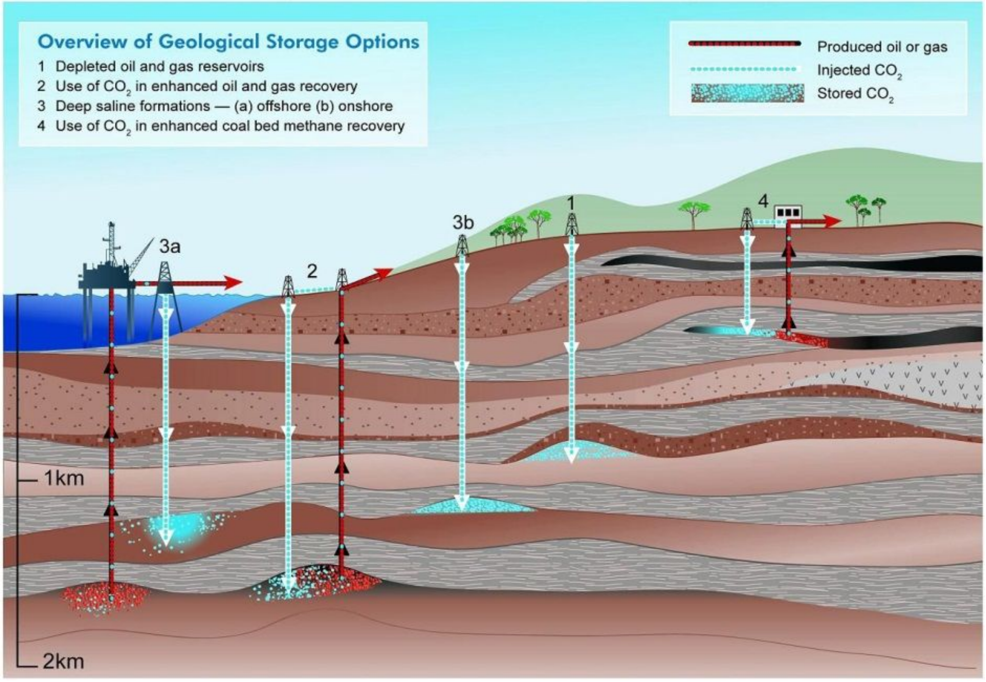

Figure 1.1. Schematic diagram of the geologic CO_2 storage in suitable deep geologic formations (Cook, 1999).

rock to prevent leakage of injected CO_2 into shallow aquifers. Saline formations exist around the world and have the largest potential for CO_2 geologic storage. Hydrocarbon (oil and gas) reservoirs are geologic formations where petroleum and/or natural gas have naturally accumulated. Hydrocarbon (oil and gas) reservoirs are prospective geologic formations for CO_2 geologic storage because of existence of sufficient geologic data for hydrocarbon exploration, verified cap rock, and low pressure of depleted hydrocarbon (oil and gas) reservoirs. Unlike saline formations and hydrocarbon (oil and gas) reservoirs, the primary trapping mechanism in coal beds is adsorption. Injected CO_2 is adsorbed in coal instead of the methane, which naturally occurs in coals, because of higher affinity of coal for CO_2 than methane. While there are uncertainties, hydrocarbon (oil and gas) reservoirs and coal beds are estimated to have a worldwide geologic CO_2 storage capacity of from 675 to 900 Gton and from 3 to 200 Gton, respectively. On the other hand, saline formations (aquifers) are estimated to have a worldwide geologic CO_2 storage capacity of at least 1,000 Gton and some studies suggest it may be an order of magnitude greater than this. Thus, saline formations are believed to have by far the largest capacity for CO_2 storage and are even much more widespread than other options. (Metz et al., 2005). Once CO_2 is injected, it is stored through a series of trapping mechanisms and is finally sequestrated permanently as solid phases (minerals) in the deep subsurface, which is separated from the atmosphere. Such trapping mechanisms are classified into physical (hydrodynamic, structural, stratigraphic, and residual) trapping, solubility (aqueous and ionic) trapping, mineral trapping, adsorption trapping, and others having different operating time frames (Bachu et al., 1994; Hitchon, 1996; Metz et al., 2005) (Figure 1.2). The dominant trapping mechanisms are changed according to time progress from physical (hydrodynamic, structural, stratigraphic, and residual) trapping on time scales of 0 to 10s years, then to solubility trapping on time scales of 10s to 100s years, and finally to mineral trapping on time scales of 100s to 1,000s years (Metz et al., 2005).

To ensure long-term stable, optimal, and maximal geologic CO_2 storage into a target geologic formation or sedimentary basin system (i.e., cap rock (seal), reservoir rocks, bedrocks, and groundwater), its three major performances such as CO_2 storage, seal, and injection capacities have to be evaluated comprehensively and quantitatively in terms of environmental friendliness, safety, and sustainability (Metz et al., 2005). Among the three major capacities, the CO_2 storage capacity is primary and crucial to project planning, site selection, site characterization, and even system designing for geologic CO_2 storage because technical and economical viability of geologic

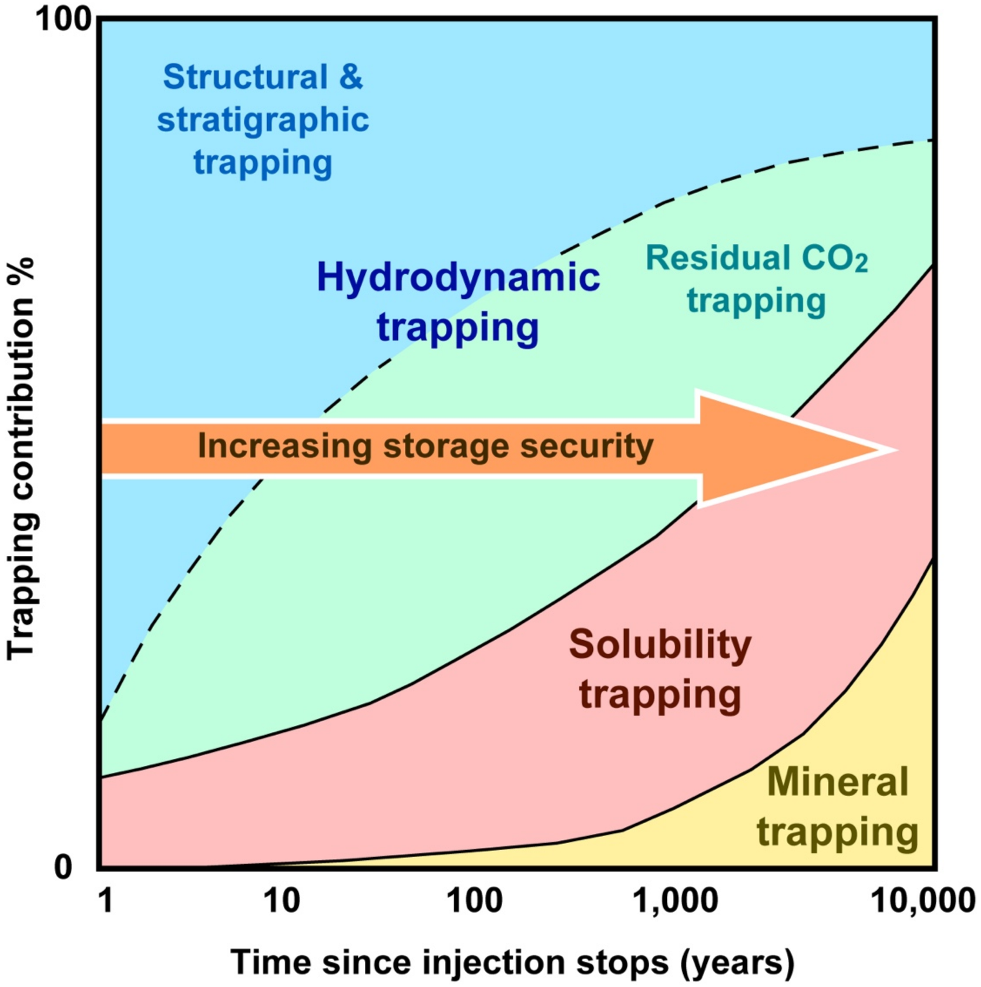

Figure 1.2. Classification of trapping mechanisms and storage security of CO_2 injected into geological formation for geological CO_2 storage (Metz et al., 2005).

CO_2 storage depends highly on the CO_2 storage capacity (CO2CRC, 2008).

The fluid-phase CO_2 storage capacity of a geologic formation (e.g., saline formation, hydrocarbon reservoir, or coal bed) or sedimentary basin system has been classified into four levels in the CSLF methodology as follows: theoretical (potential), effective (realistic), practical (viable), and matched (coincided) CO_2 storage capacities using the concept of a techno-economic resource-reserve pyramid, which is expressed in CO_2 mass (CSLF, 2005; Bachu et al., 2007; Bradshaw et al., 2007; CSLF, 2007, 2008) (Figure 1.3).

First, the theoretical (potential) CO_2 storage capacity represents the whole of the pyramid. It is obtained by occupying the physical limit of the geologic formation or sedimentary basin, such as the entire pore space or the entire pore space minus the irreducible residual saturation of the initial resident fluids (i.e., groundwater, oil, and gas), by CO_2 as described by Eq. (2.1) in Section 2.2. It assumes that the entire volume is accessible and utilized to its full storage capacity for CO_2 to be displaced in the entire pore space or adsorbed at 100% saturation in the entire coal mass. This theoretical CO_2 storage capacity is the maximum upper limit of a CO_2 storage capacity estimate and corresponds to the total resource used by the energy and mining industries. It is an unrealistic number because, in practice, there always will be geological, CO_2 physico-chemical, technological, legal and regulatory,

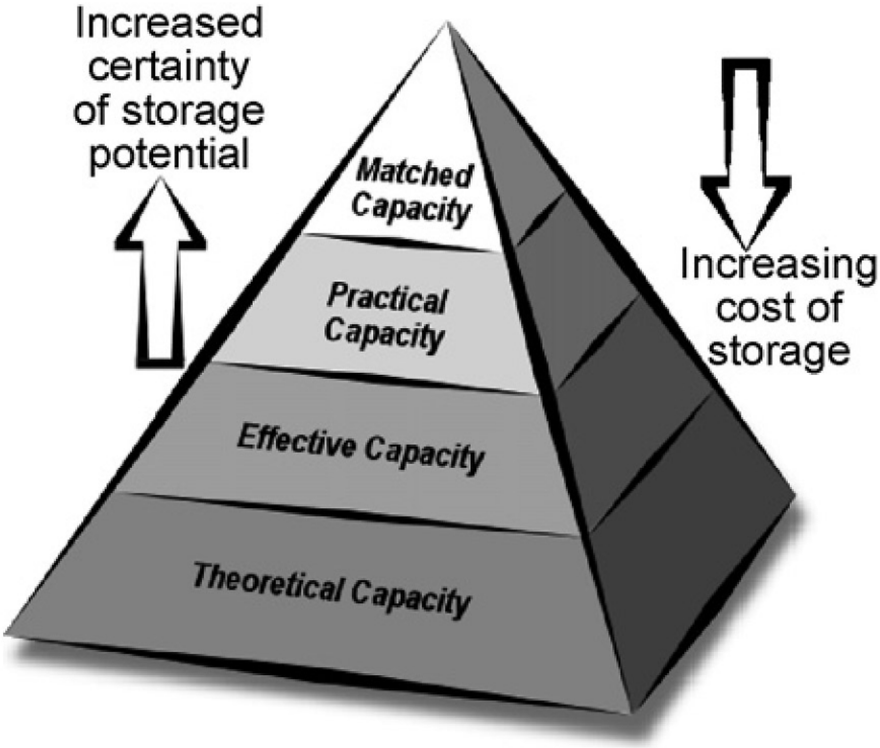

Figure 1.3. Techno-economic resource-reserve pyramid for the CO_2 storage capacities (Bachu et al., 2007).

infrastructural, and general economic limitations that prevent its full utilization.

Second, the effective (realistic) CO_2 storage capacity represents a subset of the theoretical CO_2 storage capacity that can actually be physically accessed to geologic CO_2 storage. It is obtained by applying geological (CO_2 trap heterogeneity) and CO_2 physico-chemical (CO_2 displacement or adsorption) cut-off limits (criteria), such as CO_2 storage capacity coefficients or efficiency factors, to the maximum upper limit of a CO_2 storage capacity estimate as described by Eqs. (2.2) and (2.3) in Section 2.2. This effective CO_2 storage capacity is part of the theoretical CO_2 storage capacity and corresponds to the in-place (discovered) resource used by the energy and mining industries. It usually changes with the acquisition of new data or knowledge, which can be used in determining or enhancing the geological and CO_2 physico-chemical cut-off limits including the CO_2 storage capacity coefficients or efficiency factors.

Third, the practical (viable) CO_2 storage capacity represents a subset of the effective CO_2 storage capacity. It is obtained by considering technological, legal and regulatory, infrastructural, and general economic barriers to geologic CO_2 storage. This practical CO_2 storage capacity corresponds to the reserves used in the energy and mining industries. It is susceptible to rapid changes in technologies, policies, regulations, infrastructures, and economics.

Fourth, the matched (coincided) CO_2 storage capacity represents a subset of the practical CO_2 storage capacity. It is obtained by matching large stationary CO_2 sources with geologic CO_2 storage sites that are adequate in terms of the CO_2 storage capacity (storativity), seal capacity (sealability), injection capacity (injectivity), and supply rate. This matched CO_2 storage capacity is at the top of the pyramid and corresponds to the proved marketable reserves used by the energy and mining industries.

Among the above-mentioned four levels of the fluid-phase CO_2 storage capacity in the CSLF methodology, the theoretical and effective CO_2 storage capacities are generally evaluated at relatively large basin- and regional-scales, while the practical and matched CO_2 storage capacities are evaluated at relatively small local- and site-scales. However, local- and site-scale CO_2 storage capacities have to be estimated more carefully based on numerical reservoir simulations that consider the dynamic aspects of CO_2 injection and CO_2 plume evolution. In this study, the theoretical and effective CO_2 storage capacities are evaluated only because these are primary and geologic estimates and define the upper limits of the practical and matched CO_2 storage capacities, which are secondary and economic estimates. Among the above-mentioned four levels of the fluid-phase CO_2 storage capacity in the CSLF methodology, industrial and academic CO_2 geologic storage stakeholders need to understand and enable comparison between theoretical and effective CO_2 storage capacities. In the stage of project planning and site selection for CO_2 geologic storage, the appropriate scale, such as commercial-, verification-, and pilot-scales, for purpose of research project and target geologic formation or sedimentary basin should be determined. Project planning and site selection only based on the result of the theoretical CO_2 storage capacity are impractical and unworkable because the theoretical CO_2 storage capacity is an unrealistic number. Thus, the result of the effective CO_2 storage capacity should be used at project planning and site selection. However, because of uncertainty of the fluid-phase CO_2 storage efficiency, the theoretical and effective storage capacities should be considered together. On the other hand, the effective CO_2 storage capacity corresponds to the CO_2 storage resource, and the practical CO_2 storage capacity corresponds to the CO_2 storage capacity in the US DOE methodology (NETL, 2007, 2008, 2010, 2012, 2015).

1.2. Previous studies

In order to evaluate the theoretical and effective fluid-phase CO_2 storage capacities of geologic formations (e.g., saline formations, hydrocarbon reservoirs, and coal beds) or sedimentary basin by physical trapping, a variety of approaches has been developed and used. These approaches can be divided into two categories: dynamic and static (NETL, 2008, 2010). The dynamic approach includes the decline/incline curve analysis, material balance, and reservoir simulation approaches (e.g., Nicot, 2008; Birkholzer and Zhou, 2009; Szulczewski and Juanes, 2009; Szulczewski et al., 2012), and the static approach can be divided into volumetrics- and compressibility-based approaches. The dynamic approaches typically require numerous input parameters, and thus they cannot be applied before site-specific data is collected, and field-measured CO_2 injection rates or well testing have been completed (i.e., before CO_2 injection). On the other hand, the static approaches rely on only a few parameters, which are directly related to the geologic formations (e.g., area, thickness, porosity, and compressibility), and thus they are applicable both before and after CO_2 injection or collection of field-measured CO_2 injection rates. As a result, the static approaches have been used more widely and routinely than the dynamic approaches (NETL, 2008, 2010).

The static volumetrics-based approaches (e.g., van der Meer, 1992; CSLF, 2007, 2008; NETL, 2007, 2008; Burruss et al., 2009; van der Meer and Yavuz, 2009; Brennan et al., 2010; NETL, 2010, 2012; Szulczewski et al., 2012;

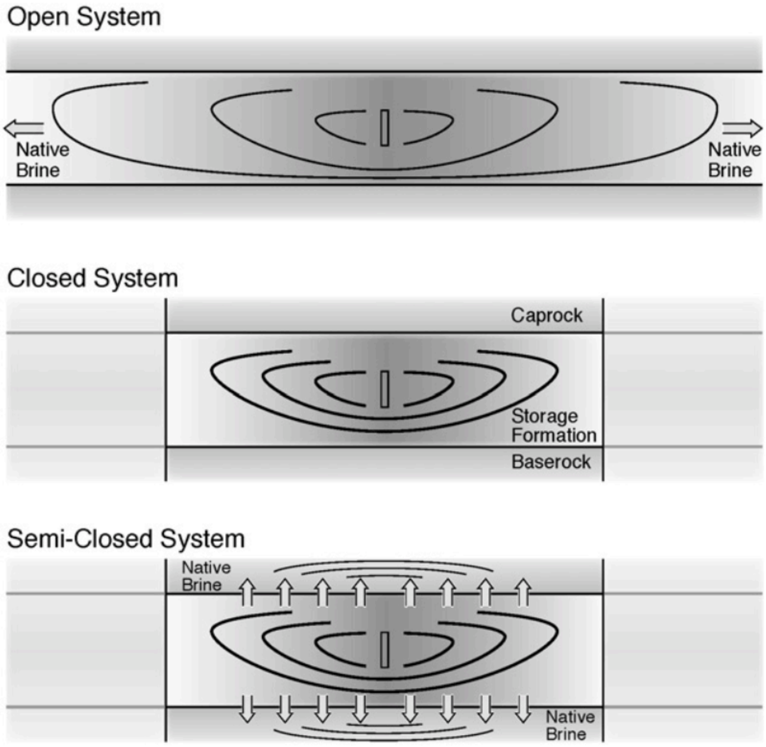

Figure 1.4. Schematic diagrams of open system, closed, and semi-closed systems (not to scale) (Zhou et al., 2008).

Blondes et al., 2013; NETL, 2015) can be applied at basin- and regional-scales saline formation, hydrocarbon reservoir, or coal bed when it is assumed that geologic formations act as open systems (Figure 1.4) so that CO_2 is stored by displacing or managing the initial resident fluids out of the systems. On the other hand, the static compressibility-based approaches (e.g., NETL, 2008; Zhou et al., 2008; Szulczewski et al., 2012) can be only applied at local- and site-scales saline formation if it is demonstrated that saline formation acts as closed and semi-closed systems (Figure 1.4). The static volumetrics- and compressibility-based approaches are similar but in order to consider that CO_2 is stored by compressing the initial resident fluids within the systems, the static compressibility-based approaches require more data such as pore compressibility and native brine compressibility. The very low compressibilities of the native fluids and rocks limit the fluid-phase CO_2 storage capacity of a closed system to a very small percentage of the total pore volume, which is to be available for CO_2 storage if the closed system is transformed into an open system. As a result, the volumetrics-based approaches provide the upper limits for the fluid-phase CO_2 storage capacities of the geologic formations (NETL, 2008, 2010).

A variety of methodologies has been presented and applied to evaluate the theoretical and effective fluid-phase CO_2 storage capacities of geologic formations (all for saline formations and hydrocarbon reservoirs and a few for coal beds) or sedimentary basin by physical trapping in various worldwide CO_2 storage potential assessments using the static volumetrics-based approaches. The theoretical and effective fluid-phase CO_2 storage capacities estimation is classified into eleven major methodologies as follow (NETL, 2012; Goodman et al., 2013; Heidug, 2013): Carbon Sequestration Leadership Forum (CSLF) Task Force for Review and Identification of Standards for CO_2 Storage Capacity Estimation (CSLF, 2005; Bachu et al., 2007; Bradshaw et al., 2007; CSLF, 2007, 2008), United States Department of Energy (US DOE) Capacity and Fairways Subgroup for Carbon Sequestration or Utilization and Storage Atlas of the United States and Canada (NETL, 2007, 2008, 2010, 2012, 2015), Queensland CO_2 Geological Storage Atlas (Bradshaw et al., 2009, 2011; Spencer et al., 2011), Australian Carbon Storage Taskforce (CST, 2009), Federal Institute for Geosciences and Natural Resources (BGR), Germany (Knopf et al., 2010), United States Geological Survey (USGS) National Geologic CO_2 Storage Assessment (Burruss et al., 2009; Brennan et al., 2010; Blondes et al., 2013), Saline-Aquifer CO_2 Sequestration in Japan (Ogawa et al., 2011), Geological Survey of the Netherlands (TNO) (Neele et al., 2011a, 2011b, 2012), Norwegian North Sea CO_2 Storage Atlas (NPD, 2011), United Kingdom CO_2 Storage

Appraisal Project (Gammer et al., 2011), and North American (Canada, United States, Mexico) Carbon Atlas Partnership (NACAP, 2012).

Among the eleven major methodologies, the US DOE methodology (NETL, 2007, 2008, 2010, 2012, 2015) and CSLF methodology (CSLF, 2005; Bachu et al., 2007; Bradshaw et al., 2007; CSLF, 2007, 2008) are basically identical with minor differences in computational formulations in terms of the theoretical and effective fluid-phase CO_2 storage capacities of saline formations, hydrocarbon reservoirs, and coal beds (CSLF, 2008; IEA GHG, 2009) (Section 2.2). In addition, the CSLF methodology has suggested conceptual and mathematical bases for the theoretical and effective aqueous-phase and mineral-phase CO_2 storage capacities of saline formations by solubility trapping (Bachu and Adams, 2003) and mineral trapping, respectively (Bachu et al., 2007; CSLF, 2007, 2008). On the other hand, NETL (2012), Goodman et al. (2013), and Heidug (2013) compared some of these various static volumetrics-based methodologies and summarized.

These eleven conventional static volumetrics-based methodologies for geologic formations (e.g., saline formations, hydrocarbon reservoirs, and coal beds) or sedimentary basin are compared and analyzed in Tables 1.1 and 1.2.

As shown in Tables 1.1 and 1.2, among the eleven conventional static volumetrics-based methodologies, Norwegian North Sea CO_2 Storage Atlas

Table 1.1. Comparison of static volumetrics-based methodologies for volume of geologic formation, total porosity, and geothermal gradient between eleven conventional methodologies and this study.

Methodology	Volume of geologic formation	Total porosity	Geothermal gradient
CSLF	Simple multiplication	Deterministic	Deterministic
US DOE	Simple multiplication	Deterministic	Deterministic
CST	Simple multiplication	Deterministic	Deterministic
CGSS	Simple multiplication	Deterministic	Deterministic
USGS	Simple multiplication	Probabilistic	Probabilistic
BGR	Simple multiplication	Probabilistic	Probabilistic
TNO	Simple multiplication	Deterministic	Deterministic
NPD	Three-dimensional geologic modeling	Deterministic	Deterministic
Japan	Simple multiplication	Deterministic	Deterministic
UK	Simple multiplication	Deterministic	Deterministic
NACAP	Simple multiplication	Deterministic	Deterministic
This study	Three-dimensional geologic modeling	Probabilistic	Probabilistic

Table 1.2. Comparison of static volumetrics-based methodologies for fluid-phase CO_2 density, storage efficiency, and storage capacity between eleven conventional methodologies and this study.

Methodology	Fluid-phase CO_2 density	Fluid-phase CO_2 storage efficiency	Fluid-phase CO_2 storage capacity
CSLF	Deterministic	Deterministic	Deterministic
US DOE	Deterministic	Partial probabilistic	Partial probabilistic
CST	Deterministic	Deterministic	Partial probabilistic
CGSS	Deterministic	Deterministic	Deterministic
USGS	Probabilistic	Partial probabilistic	Partial probabilistic
BGR	Probabilistic	Partial probabilistic	Partial probabilistic
TNO	Deterministic	Deterministic	Deterministic
NPD	Deterministic	Deterministic	Deterministic
Japan	Deterministic	Deterministic	Deterministic
UK	Deterministic	Partial probabilistic	Partial probabilistic
NACAP	Deterministic	Partial probabilistic	Partial probabilistic
This study	Probabilistic	Probabilistic	Probabilistic

(NPD, 2011) only obtains volume of geologic formation from result of the three-dimensional geologic modeling. However, although the volume of geologic formation is obtained from the result of three-dimensional geologic modeling, grid-based CO_2 storage capacity estimation is not performed. On the other hand, the other methodologies obtain volume of geologic formation from simple multiplication of formation area and thickness. United States Geological Survey (USGS) National Geologic CO_2 Storage Assessment (Burruss et al., 2009; Brennan et al., 2010; Blondes et al., 2013) and Federal Institute for Geosciences and Natural Resources (BGR) use probabilistic total porosity, geothermal gradient, and fluid-phase CO_2 storage density, while the other methodologies use deterministic (e.g., average and typical) total porosity, geothermal gradient, and fluid-phase CO_2 storage density. United States Department of Energy (US DOE) Capacity and Fairways Subgroup for Carbon Sequestration or Utilization and Storage Atlas of the United States and Canada (NETL, 2007, 2008, 2010, 2012, 2015), Australian Carbon Storage Taskforce (CST, 2009), United States Geological Survey (USGS) National Geologic CO_2 Storage Assessment (Burruss et al., 2009; Brennan et al., 2010; Blondes et al., 2013), Federal Institute for Geosciences and Natural Resources (BGR), Germany (Knopf et al., 2010), United Kingdom CO_2 Storage Appraisal Project (Gammer et al., 2011), and North American

(Canada, United States, Mexico) Carbon Atlas Partnership (NACAP, 2012) estimate fluid-phase CO_2 storage efficiency and storage capacity partial probabilistically, while the other methodologies estimate fluid-phase CO_2 storage efficiency and storage capacity deterministically.

In these eleven conventional static volumetrics-based methodologies for saline formations or sedimentary basin, the theoretical and effective fluid-phase CO_2 storage capacities are commonly expressed as simple multiplicative combinations of the total pore volume, CO_2 density, and volumetric fluid-phase CO_2 storage efficiency factor. Among them, the total pore volume is also expressed as simple multiplicative combinations of total area, gross formation thickness, and (total) porosity. Although saline formations have three-dimensionally irregular or complex shapes, the simple multiplicative combinations, especially total area and gross formation thickness, can significantly overestimate or underestimate the total pore volume. Thus, making precise assumptions of geologic formation, geologic structures (faults), lithofacies, and geologic properties are important on geologic CO_2 storage researches. In order to get geologic data at deep depth, drilling and boring is generally performed because it is the most precisely and directly. However, sufficient number of drilling and boring data is not acquired due to constraints such as investigation expense, labor, time and other factors (Koo et al., 2006). Thus, research on three-dimensional geologic modeling is being performed widely to visualize three-dimensionally and characterize quantitatively of geologic formation or sedimentary basin. Furthermore, the geologic CO_2 storage capacity estimation at grid (cell, element)-scales based on the result of three-dimensional geologic grid modeling can visualize spatial distribution of the geologic CO_2 storage capacity.

A variety of three-dimensional geologic modeling has been presented to make precise assumption of geologic formation, geologic structures (faults), lithofacies, and geologic properties. First of all, in order to analyze geologic structural characteristics of geologic formation or sedimentary basin, several three-dimensional geologic structure modelings were performed (e.g., Guyonnet-Benaize et al., 2010; Vilain 2010). These researches primarily analyzed borehole, satellite photograph, ground surface geologic map, numerical information, and etc. Three-dimensional geologic structure modeling is then performed to visualize and quantitative characterize the geologic structures (faults) by using discrete smooth interpolation (DSI) algorithm (Mallet, 1989). In order to discretize geologic formation and visualize geologic formation distribution, several three-dimensional geologic grid and geologic formation modeling ware also performed (e.g., Gwak and

Lee, 2001; Kaufmann et al., 2009; Zanchi et al., 2009). In addition, in order to predict spatial distribution of ore body, lithofacies, and rock mass properties, several three-dimensional geologic property modeling were performed (e.g., Kim and Park, 2009; Kim et al., 2010; Wang and Huang, 2012). These researches were performed using interpolation methods, such as inverse distance weighting (IDW) (Shepard, 1968) and kriging (Matheron, 1963) algorithm. However, these interpolation methods cannot handle uncertainty of production. Therefore, conditional simulation of stochastic method was suggested in order to overcome disadvantage of interpolation methods.

Recently, several studies have been used three-dimensional geologic models to estimate geologic CO_2 storage capacity (Probst, 2008; Birkholzer and Zhou, 2009; Kopp et al., 2009; NPD, 2011). These studies were performed three-dimensional geologic modeling or used preliminarily build three-dimensional geologic models. However, the single bulk volume of geologic formation was used at simple multiplicative combination for the total pore volume which cannot reflect three-dimensionally irregular or complex shape of saline formation or sedimentary basin. On the other hand, the three-dimensional geologic grid model was not used to static volumetrics-based methodologies but dynamic approaches (reservoir simulation).

Among the above-mentioned eleven major static volumetrics-based methodologies, CSLF methodology (CSLF, 2005; Bachu et al., 2007; Bradshaw et al., 2007; CSLF, 2007, 2008), US DOE methodology (NETL, 2007, 2008, 2010, 2012, 2015), and USGS methodology (Burruss et al., 2009; Brennan et al., 2010; Blondes et al., 2013) are more well-established compared with the other methodologies. Each of the three methodologies has its own advantages in different aspects.

First, although the fluid-phase CO_2 storage efficiency has discussed in the above mentioned eleven major static volumetrics-based methodologies, the US DOE methodology has presented the most inclusive and comprehensive expression for the fluid-phase CO_2 storage efficiency factor, which is further broken into seven multiplicative fluid-phase CO_2 storage efficiency parameters (terms) (NETL, 2007, 2008; IEA GHG, 2009; NETL, 2010, 2012, 2015) (Section 2.2). A series of Monte Carlo and numerical simulations has also been performed to estimate and compile highly reliable and broadly applicable probability ranges (databases) of the US DOE methodology’s fluid-phase CO_2 storage efficiency parameters and factors for various saline formations in USA, Canada, and other countries including the Average Global Database (AGD) (NETL, 2007, 2008; IEA GHG, 2009; NETL, 2010, 2012, 2015) (Section 2.2). On the other hand, Carbon Sequestration Leadership

Forum (CSLF, 2005; Bachu et al., 2007; Bradshaw et al., 2007; CSLF, 2007, 2008) defines the storage coefficient including mobility, buoyancy, heterogeneity, water saturation, and aquifer strength, but the value of storage coefficient has not suggested. Australian Carbon Storage Taskforce (CST, 2009) has assumed the storage efficiency factor with a single number of 4% in the reason that the fraction of the total pore volume that will be occupied by CO_2 is not well known, and it may vary considerably depending on geology. Queensland CO_2 Geological Storage Atlas (Bradshaw et al., 2009, 2011; Spencer et al., 2011) had suggested storage efficiency (SE) with the range of 0.10% to 0.15% based on reservoir thickness versus CO_2 plume thickness using precalculated residual gas saturation storage efficiency curves for various plume thicknesses. United States Geological Survey (Burruss et al., 2009; Brennan et al., 2010; Blondes et al., 2013) has suggested storage efficiencies including three categories of residual trapping storage efficiencies and buoyant trapping storage efficiency. Federal Institute for Geosciences and Natural Resources (BGR), Germany (Knopf et al., 2010) has suggested storage efficiency factor distributed between 5% to 20% using Monte Carlo simulation. Geological Survey of the Netherlands (TNO) (Neele et al., 2011a, 2011b, 2012) and Norwegian North Sea CO_2 Storage Atlas (NPD, 2011) have assumed the storage efficiency factor with the values of 4%

and about 5%, respectively, based on the literature or numerical simulation results. Saline-Aquifer CO_2 Sequestration in Japan (Ogawa et al., 2011) has also assumed the storage efficiency factor with the value of 12.5% based on the literature. United Kingdom CO_2 Storage Appraisal Project (Gammer et al., 2011) has only considered irreducible water saturation and volumetric sweep efficiency derived from results of a flow simulation model. North American (Canada, United States, Mexico) Carbon Atlas Partnership (NACAP, 2012) has used the US DOE's fluid-phase CO_2 storage efficiency.

Second, the USGS methodology has subdivided sophisticatedly the storage formation pore volume (SF_{PV}) within a storage assessment unit (SAU) (i.e., saline formation) into four different pore volumes (one class for buoyant trapping and three classes for residual trapping) based on five criteria (Figure 1.5). They are the depth limit (between 914 m and 3,962 m), the salinity limit (TDS more than 10,000 ppm), the seal formation (cap rock) limit, the dominant physical trapping mechanisms (buoyant (structural and stratigraphic) trapping and residual trapping), and the injectivity category allotments by permeability (1 millidarcy and 1 darcy) in residual trapping. Among the above-mentioned five criteria, the upper vertical limit of depth is 914 m (3,000 ft) to ensure that CO_2 is in a supercritical phase to minimize the storage volume (i.e., maximize the storage capacity per unit volume). And

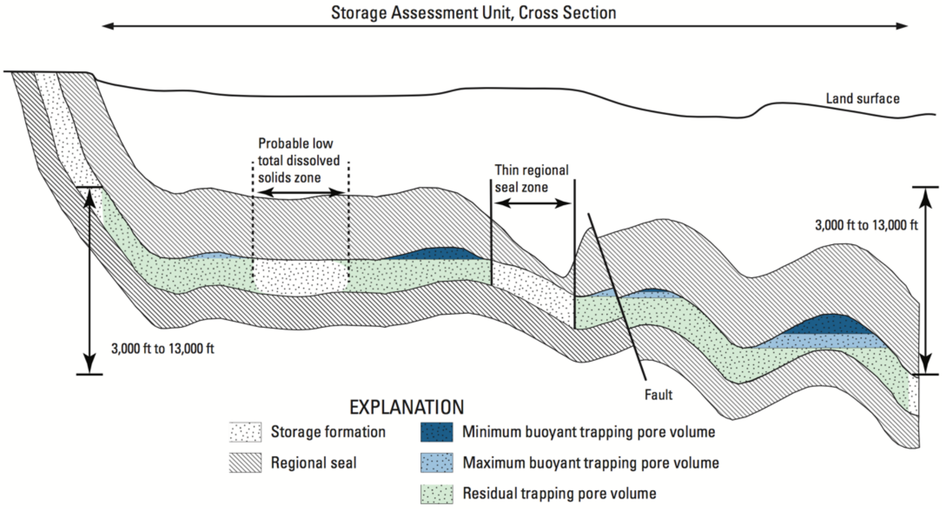

Figure 1.5. Schematic cross section through a storage assessment unit (SAU) illustrating the relation between buoyant and residual trapping styles in the storage formation (Blondes et al., 2013).

the lower vertical limit of depth is 3,962 m (13,000 ft) to consider the potential CO_2 injection depth at pipeline pressures without additional compression at the surface. The salinity (TDS concentration) is limited more than 10,000 mg/L, regardless of depth, to prevent and regulate injection of CO_2 into underground sources of drinking water (USDW). And the residual pore volume is apportioned into three rock classes by permeability (i.e., greater than 1 Darcy, 1 millidarcy to 1 Darcy, and less than 1 millidarcy). Class 1 rock have very high permeability (greater than 1 Darcy) and the highest injectivity value. However, it has less pore-scale residual trapping, due to the lack of small pore throats. Class 2 rock have moderate permeability (1 millidarcy to 1 Darcy) and minor to no injectivity issue. Thus, it has high potential for residual trapping ranging from pore scale to larger scale. Class 3 rock have low permeability (less than 1 millidarcy) and little to no injectivity. Thus, little CO_2 enter this rock without artificial fracturing. As a result, the logically more sophisticated USGS methodology requires more (site-specific) data, detailed information, additional assumptions, complicate procedures, subjective judgments, and professional experiences than the logically more simple US DOE methodology. Thus, the US DOE methodology, which is computationally equivalent to the CSLF methodology (Section 2.2), is adopted in this study because it has the most generalized forms of the fluid-phase CO_2 storage efficiency parameters and factors as well as the highly reliable and broadly applicable big databases for their values.

1.3. Improvements and developments of this study

Before adopting, the US DOE methodology needs further improvement and development in terms of the following three aspects in order to overcome its limitations and increase its applicability and feasibility.

First (three-dimensional geologic modeling for irregular and heterogeneous system), the US DOE methodology for saline formations simplifies the geometries as horizontal layers with uniform thicknesses and assume that the porosity and CO_2 density are spatially homogeneous. Although saline formations are very thick and have three-dimensionally, especially vertically, irregular or complex shapes in most cases, the total pore volume is also expressed as simple multiplicative combinations of total area, gross formation thickness, and (total) porosity. As a result, spatially representative single values can be straightforwardly determined for the thickness, porosity, and CO_2 density, respectively. However, such simplification and assumption can overestimate or underestimate the theoretical and effective fluid-phase CO_2 storage capacities. As a result, the thickness, porosity, and CO_2 density are not constants but variables within saline formations. In particular, the CO_2 density is a function of the pressure and temperature, in turn which are dependent on the depth and location within saline formations. Thus, the theoretical and effective fluid-phase CO_2 storage capacities based on the improved US DOE methodology are better to be evaluated spatially at grid (cell, element)-scales through three-dimensional geologic modeling or other geostatistical spatial discretization of the geometry, porosity, pressure, and temperature (Section 2.1).

Second (estimation of individual gas-, liquid-, and supercritical-phase CO_2 storage capacities), the US DOE methodology for saline formations explicitly recommends considering only saline formations that have the TDS greater than 10,000 ppm and are deeper than 800 m and confined by cap rock. However, the 800-m-depth cutoff is an arbitrary attempt to select a necessary depth to ensure that the pressure and temperature are in excess of the critical point of CO_2, and thus CO_2 is in a high-density liquid or supercritical phase. As a result, the theoretical and effective fluid-phase CO_2 storage capacities can be underestimated or overestimated. The CSLF methodology, which is basically identical to the US DOE methodology (Section 2.2), does not recommend these arbitrary screening criteria (i.e., minimum TDS and depth cutoffs) (CSLF, 2008). Instead, throughout entire saline formations without such arbitrary screening criteria, the fluid-phase CO_2 density and the corresponding CO_2 fluid phase type among gas, liquid, and supercritical phases must be precisely calculated and identified to determine quantitatively optimal locations of CO_2 storage or injection in saline formations. IEA GHG (2009) suggests that the 800-m-depth cutoff is not designed to preclude any potential storage projects shallower than 800 meters but is rather a recognition that because of the low-density gas-phase CO_2 that it would not contribute significantly to overall storage mass of CO_2. High-density liquid- or supercritical-phase CO_2 is injected into the geologic formation at over 800 m depth, it moves upward by buoyancy to the overlying cap rock, which can be located less than 800 m depth. In other words, although CO_2 is injected into the geologic formation at over 800 m depth as liquid- or supercritical-phase, CO_2 is also stored at entire geologic formation or sedimentary basin including less than 800 m depth as gas-, liquid-, and supercritical-phase. Thus, in order to estimate CO_2 storage capacity precisely, the theoretical and effective individual gas-, liquid-, supercritical-, and whole fluid-phase CO_2 storage capacities based on the improved US DOE methodology are all better to be evaluated spatially at grid (cell, element)-scales after three-dimensional geologic modeling of the geometry, porosity, pressure, temperature, and CO_2 density and phases (Section 2.2).

Third (probabilistic evaluation using grid-based Monte Carlo simulation), although the US DOE methodology for saline formations has estimated probabilistically the fluid-phase CO_2 storage efficiency parameters and factors, it has adopted only a set of a low estimate and a high estimate (i.e., P_{15} and P_{85} or P_{10} and P_{90}) of the fluid-phase CO_2 storage efficiency factors and thus has calculated deterministically only a corresponding set of a low value and a high value of the effective fluid-phase CO_2 storage capacities. However, such partially probabilistic or deterministic evaluation can neither overcome insufficient number or lack of input data and their spatially uneven distributions nor reduce complexity and uncertainty of input and output data. Thus, the theoretical and effective individual gas-, liquid-, supercritical-, and whole fluid-phase CO_2 storage capacities based on the improved US DOE methodology are all better to be evaluated probabilistically through grid-based (wise) Monte Carlo simulations after three-dimensional geologic modeling of the geometry, porosity, pressure, temperature, and CO_2 density and phases (Section 2.2).

As a whole, as shown in Table 1.1, grid-based geologic formation volume is adopted through three-dimensional geologic modeling to obtain precise volume of irregular or complex shape of saline formation. Grid-based CO_2 density and phases are then calculated using grid-based geologic formation volume and probabilistic (total) porosity and geothermal gradient to estimate individual gas-, liquid-, supercritical- and whole fluid-phase CO_2 storage capacities without arbitrary screening criteria (i.e., minimum TDS and depth cutoffs). Fluid-phase CO_2 storage efficiency factor and gas-, liquid-, supercritical- and whole fluid-phase CO_2 storage capacity is then calculated and evaluated using grid-based Monte Carlo simulation after three-dimensional geologic modeling of the geometry, porosity, pressure, temperature, and CO_2 density and phases.

1.4. Objectives of this study

The first objective of this study is to present a linked methodology of a series of three-dimensional geologic modeling and grid-based Monte Carlo simulation (Section 2), which can overcome the limitations of the US DOE methodology and increase its applicability and feasibility.

The second objective of this study is then to evaluate probabilistically the theoretical and effective individual gas-, liquid-, supercritical-, and whole fluid-phase CO_2 storage capacities of the saline formations in the Pohang Basin using such a linked methodology (Section 3) based on geologic data available to the basin. The Pohang Basin has been identified as one of the most prospective and suitable sedimentary basins in Korea for commercial-scale geologic CO_2 storage. In order to achieve the second objective, a series of three-dimensional geologic modeling (i.e., three-dimensional geologic structure, stratigraphy, grid, formation modeling) (Section 4) and individual gas-, liquid-, supercritical-, and whole fluid-phase CO_2 storage capacity estimation with grid-based Monte Carlo simulation (Section 5) are sequentially performed. In order to identify and present the improvements and developments of fluid-phase CO_2 storage capacity estimation using the linked methodology than the US DOE methodology, fluid-phase CO_2 storage capacity estimation of two saline formations SMSS and FCSS in the Pohang Basin is performed using the US DOE methodology.

The third objective of this study is then to evaluate spatially the theoretical and effective individual gas-, liquid-, supercritical-, and whole fluid-phase CO_2 storage capacities (Section 6) of the saline formations in the Pohang Basin and to determine optimal locations of CO_2 storage by summarizing and analyzing the results of the three-dimensional geologic modeling and CO_2 storage capacity estimation with grid-based Monte Carlo simulation.

2. Linked methodology

2.1. Three-dimensional geologic modeling

A series of three-dimensional geologic modeling (i.e., three-dimensional geologic structure, stratigraphy, grid, formation modeling) is performed using GOCAD (Geological Object Computer Aided Design) (Paradigm, 2014) to establish the three-dimensional geologic structure, stratigraphy, grid, and formation models of the Pohang Basin. GOCAD is a computer aided design (CAD) geologic modeling program for geological, geophysical, reservoir engineering, and other various applications, which was initiated by Mallet and his research group in 1989 (Mallet, 1992a). This geostatistical program is developed based on the discrete smooth interpolation (DSI) technique, which is designed to account for heterogeneous and imprecise data encountered in geology (Mallet, 1989; Mallet, 1992b; Mallet, 1997). Since 2013, GOCAD has been merged with SKUA (Subsurface Knowledge Unified Approach) into the SKUA-GOCAD suite based on the updating vector transform (UVT) algorithm to incorporate and handle difficult and complex geologic structures such as salt domes, overthrusts, and reverse faults.

A series of three-dimensional geologic modeling is subdivided into three-dimensional geologic structure modeling, three-dimensional geologic stratigraphy modeling, three-dimensional geologic grid modeling, three-dimensional geologic formation modeling. First, three-dimensional geologic structure modeling is to build geologic structures (faults) using the discrete smooth interpolation (DSI) technique with the data obtained from analyzed and computerized raw data (i.e., digital topographic map, electronic navigational chart, surface geologic map, offshore geologic cross-sections with geologic structures (faults) and formations). Second, three-dimensional geologic stratigraphy modeling is to build upper surfaces of geologic formations using the discrete smooth interpolation (DSI) technique with the data obtained from analyzed and computerized raw data (i.e., digital topographic map, electronic navigational chart, surface geologic map, offshore geologic cross-sections with geologic structures (faults) and formations). The resultant three-dimensional geologic stratigraphy model (i.e., upper surfaces of geologic formations) can be dissected and offset by the geologic structures (faults). Third, three-dimensional geologic grid modeling is to discretize the modeling domain into hexahedral grid blocks (elements). Forth, three-dimensional geologic formation modeling is to visualize geologic formation distribution by polymerizing three-dimensional geologic structure model, three-dimensional geologic stratigraphy model, and three-dimensional grid model.

In order to clarify the concept of three-dimensional geologic modeling, performed in this study, the procedure of three-dimensional geologic modeling is defined as a workflow chart (Figure 2.1). First, raw data such as digital topographic map and electronic navigation chart (Figure 2.1a), surface geologic map (Figure 2.1b), and offshore geologic cross-sections with geologic structures (faults) and formations (Figure 2.1c) is analyzed and computerized to generate basic computational input data for three-dimensional geologic modeling. The generated basic computational input data are digital elevation model (DEM) with surface geologic map and offshore geologic cross-sections (Figure 2.1d) and virtual boreholes with geologic structures (faults) and formations (Figure 2.1e). Using these generated basic computational input data, a series of three-dimensional geologic modeling (i.e., three-dimensional geologic structure modeling (Figure 2.1f), three-dimensional geologic stratigraphy modeling (Figure 2.1g), three-dimensional geologic grid modeling (Figure 2.1h) and three-dimensional geologic formation modeling (Figure 2.1i)) is performed sequentially to establish the three-dimensional geologic structure, stratigraphy, grid, and formation models.

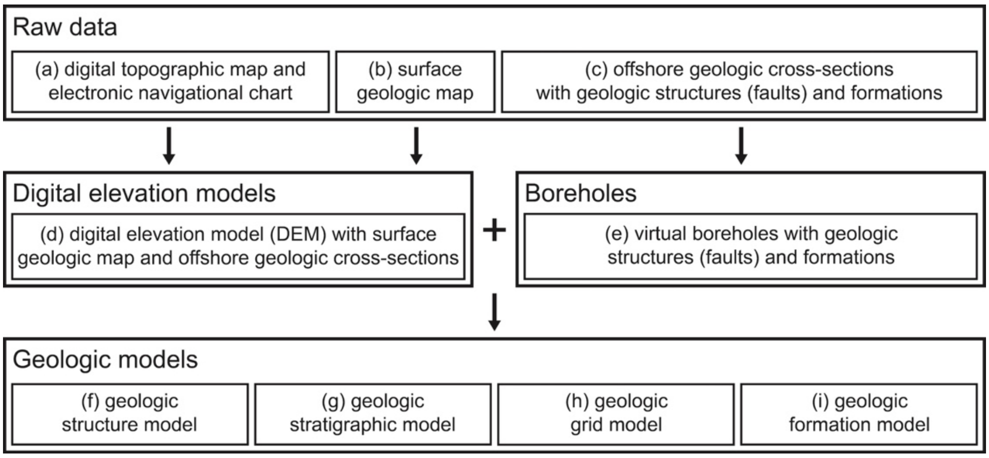

Figure 2.1. Workflow chart of three-dimensional geologic modeling of the Pohang Basin.

2.2. Grid-based Monte Carlo simulation

A series of grid-based (wise) Monte Carlo simulation is performed using Grid Converter (Kim, C.S. et al., 2013) and CO_2-STOR (Kihm et al., 2017) to estimate the theoretical and effective individual gas-, liquid-, supercritical-, and whole fluid-phase CO_2 storage capacities of the clastic saline formations in the Pohang Basin as an open system.

Grid Converter (Kim, C.S. et al., 2013) is a conversion model for grid, material property, and physico-chemical condition information data between three-dimensional geologic modeling programs (e.g., GOCAD, SKUA, Petrel), behavior prediction models using FEM and IFDM (e.g., TOUGH Family, ECLIPSE Suite, CMG Suite), performance evaluation models (e.g., CO_2-STOR, CO_2-LEAK), and pre- and post-processing programs (e.g., Tecplot, Visual FEA, Visual COFAT3D). Grid Converter also includes the GOCAD2TOUGH module. Grid Converter has updated to converse grid, material property, and physico-chemical condition information data accurately and precisely from three-dimensional geologic modeling program GOCAD to probabilistic evaluation model CO_2-STOR.

CO_2-STOR (Kihm et al., 2017) is a probabilistic evaluation model for theoretical and effective gas-, liquid-, supercritical-phase (i.e., fluid-phase) CO_2 storage capacities of saline formations and consists of the following three major compartments. First, this model is developed based on the static volumetrics-based formulations for estimating the theoretical and effective gas-, liquid-, supercritical-, and fluid-phase CO_2 storage capacities (Bachu et al., 2007; CSLF, 2007, 2008; NETL, 2007, 2008; IEA GHG, 2009; NETL, 2010, 2012, 2015; Kim, 2011, 2012a, 2012b). Second, the H_2O-NaCl-CO_2 mixture equation of state (EOS) model ECO2N (Pruess, 2005) is implemented into CO_2-STOR for calculating the CO_2 and/or H_2O densities and solubilities dependent on the pressure (P), temperature (T), and salt mass fraction or concentration (groundwater salinity) (X_S) and thus for identifying the corresponding CO_2 fluid phase type among gas, liquid, and supercritical phases. ECO2N is a fluid property module for the TOUGH2 simulator (Pruess et al., 2012). It provides an accurate description of the thermophysical properties of mixtures of water, salt, and CO_2 under conditions typically encountered in geologic formations (e.g., saline formations) of interest for geologic storage of CO_2 (i.e., $P \leq 60$ MPa, $10°C \leq T \leq 110°C$, salinity up to full halite saturation). As independent input variables, the pressure, temperature, and salt mass fraction or concentration (groundwater salinity) at grid block centers can be imported into CO_2-STOR by various means as follows: simple assumptions (e.g., hydrostatic pressure and uniform groundwater salinity), laboratory experiments (e.g., intrinsic permeability and thermal conductivity), field measurements (e.g., geothermal gradient and heat flow), numerical simulations (e.g., fluid flow and heat transport modeling), and any combinations. Third, the Latin Hypercube sampling (LHS) technique (Mckay et al., 1979) is incorporated into CO_2-STOR for performing grid-based Monte Carlo simulation. Latin Hypercube sampling (LHS) is a statistical method of generating random samples of parameter values from a multidimensional distribution. It is widely used in Monte Carlo simulation. When performing random sampling, considerable number of runs are necessary to perform in order to achieve a reasonably accurate result. Also, even if random sampling is performed for a considerable number of times, it cannot be guaranteed that the result of random sampling achieves a reasonably accurate result. However, when performing Latin Hypercube sampling (LHS), it can drastically reduce the number of runs necessary to achieve a reasonably accurate result. Because Latin Hypercube sampling (LHS) is based on the Latin square design, which has a single sample in each row and column. Thus, proper number of runs are sufficient to perform in order to achieve a reasonably accurate result. Previous version of CO_2-STOR only estimates fluid-phase CO_2 storage capacity and have to apply two arbitrary screening criteria (i.e., 800-m-depth and supercritical-phase cutoffs). CO_2-STOR has updated to allow selection of arbitrary screening criteria and estimate individual gas-, liquid-, and supercritical-phase CO_2 storage capacities. In addition, previous version of CO_2-STOR only presents the results with simple outputs such as CO_2 storage density, theoretical and effective CO_2 storage capacities. Thus, CO_2-STOR is updated to present the results with sufficient outputs such as grid-based CO_2 density, fluid-phase CO_2 storage efficiency parameters and factor, and theoretical and effective individual gas-, liquid-, supercritical-, and whole fluid-phase CO_2 storage capacities.

In terms of physical trapping of injected CO_2, the time-independent theoretical and effective individual gas-, liquid-, supercritical-, and whole fluid-phase CO_2 storage capacities of a saline formation acting as an open system can be expressed using the static volumetrics-based approach (Bachu et al., 2007; CSLF, 2007, 2008; NETL, 2007, 2008; IEA GHG, 2009; NETL, 2010, 2012, 2015) after its improvement for fluid-phase CO_2 (Kim, 2011, 2012a, 2012b) as follows:

$$\begin{aligned} M_{t\,CO_2\,jp} &= \int_{V_{jp}} n_t\,\rho_{CO_2\,jp}\,dV_{jp} = \int_{V_{jp}} I_{t\,CO_2\,jp}\,dV_{jp} \\ &= \sum_{i_{jp}=1}^{N_{jp}} V_{jp}^{i_{jp}}\,n_t^{i_{jp}}\,\rho_{CO_2\,jp}^{i_{jp}} = \sum_{i_{jp}=1}^{N_{jp}} V_{p\,jp}^{i_{jp}}\,\rho_{CO_2\,jp}^{i_{jp}} \end{aligned}$$

$$= \sum_{i_{jp}=1}^{N_{jp}} V_{jp}^{i_{jp}} \rho_{t\,CO_2\,jp}^{i_{jp}} = \sum_{i_{jp}=1}^{N_{jp}} M_{t\,CO_2\,jp}^{i_{jp}}$$

(2.1)

$$M_{e\,CO_2\,jp} = \int_{V_{jp}} n_t\, \rho_{CO_2\,jp}\, E_{CO_2\,jp}\, dV_{jp} = \int_{V_{jp}} I_{e\,CO_2\,jp}\, dV_{jp}$$
$$= \sum_{i_{jp}=1}^{N_{jp}} V_{jp}^{i_{jp}}\, n_t^{i_{jp}}\, \rho_{CO_2\,jp}^{i_{jp}}\, E_{CO_2\,jp} = \sum_{i_{jp}=1}^{N_{jp}} V_{p\,jp}^{i_{jp}}\, \rho_{CO_2\,jp}^{i_{jp}}\, E_{CO_2\,jp}$$
$$= \sum_{i_{jp}=1}^{N_{jp}} V_{jp}^{i_{jp}}\, I_{e\,CO_2\,jp}^{i_{jp}} = \sum_{i_{jp}=1}^{N_{jp}} M_{e\,CO_2\,jp}^{i_{jp}}$$
$$= \sum_{i_{jp}=1}^{N_{jp}} M_{t\,CO_2\,jp}^{i_{jp}}\, E_{CO_2\,jp} = M_{t\,CO_2\,jp}\, E_{CO_2\,jp}$$

(2.2)

where $M_{t\,CO_2\,jp}$ is the theoretical j-phase CO2 storage capacity $[M]$ of the saline formation ($M_{t\,CO_2\,fp} = M_{t\,CO_2\,gp} + M_{t\,CO_2\,lp} + M_{t\,CO_2\,sp}$), $M_{e\,CO_2\,jp} = M_{t\,CO_2\,jp} E_{CO_2\,jp}$ is the effective j-phase CO2 storage capacity (US DOE j-phase CO2 storage resource) $[M]$ of the saline formation ($M_{e\,CO_2\,fp} = M_{e\,CO_2\,gp} + M_{e\,CO_2\,lp} + M_{e\,CO_2\,sp}$), V_{jp} is the volume $[L^3]$ of the saline formation (i.e., the domain of interest) occupied by the j-phase CO2 ($V_{fp} = V_{gp} + V_{lp} + V_{sp} = V_t$), $dV_{jp} = dxdydz_{jp}$ is the differential volume $[L^3]$ of the saline formation occupied by the j-phase CO2, $n_t(x,y,z)$ is the (total) porosity $[L^3/L^3]$ of the saline formation, $\rho_{CO_2\,jp}(P,T,X_s)$ is the j-phase CO2 density $[M/L^3]$ at its equilibrium physico-chemical conditions (P,T,X_s), $V_{p\,jp} = V_{jp}\,n_t$ is the pore volume $[L^3]$ of the saline formation occupied by the j-phase CO2 ($V_{p\,fp} = V_{p\,gp} + V_{p\,lp} + V_{p\,sp} = V_{p\,t}$), $I_{t\,CO_2\,jp} = n_t\,\rho_{CO_2\,jp} = M_{t\,CO_2\,jp}/V_{jp}$ is the theoretical j-phase CO2 storage density (intensity) $[M/L^3]$ of the saline formation, $E_{CO_2\,jp} = M_{e\,CO_2\,jp}/M_{t\,CO_2\,jp}$ is the formation-level j-phase CO2 storage efficiency factor $[L^3/L^3]$ of the saline formation ($E_{CO_2\,gp} = E_{CO_2\,lp} = E_{CO_2\,sp} = E_{CO_2\,fp}$), $I_{e\,CO_2\,jp} = n_t\,\rho_{CO_2\,jp}\,E_{CO_2\,jp} = M_{e\,CO_2\,jp}/V_{jp}$ is the effective j-phase CO2 storage density (intensity) $[M/L^3]$ of the saline formation ($I_{e\,CO_2\,jp} = I_{t\,CO_2\,jp}\,E_{CO_2\,jp}$), N_{jp} is the number of grid blocks (elements) used in spatial discretization of the saline formation occupied by the j-phase CO2 ($N_{fp} = N_{gp} + N_{lp} + N_{sp} = N_t$), the subscript jp denotes the j-phase of CO2 (jp = gas-phase (gp), liquid-phase (lp), supercritical-phase (sp), and fluid-phase (fp)), and the superscript i_{jp} denotes the value of the corresponding parameter in the i_{jp}-th grid block used in spatial discretization of the saline formation occupied by the j-phase CO2 or at its center ($i_{gp} \neq i_{lp} \neq i_{sp} \neq i_{fp}$). Here x, y, and z are the coordinate axes $[L]$, P is the pressure $[ML/T^2L^2]$, T is the temperature $[\theta]$, X_s is the groundwater salinity (salt mass fraction or concentration) $[M/M]$, V_t is the total (gross) volume $[L^3]$ of the saline formation, $V_{p\,t}$ is the total pore volume $[L^3]$ of the saline formation, and N_t is the total number of grid blocks (elements) used in spatial discretization of the saline formation. In addition, the terms in the brackets indicate the dimensions of the corresponding parameters, $[M]$ is the mass, $[L]$ is the length, $[T]$ is the time, and $[\theta]$ is the temperature. Here the (total) porosity $(n_t(x, y, z))$ of the saline formation is used as a formation-level parameter due to the lack of a sufficient number of (total) porosity data. If a sufficient number of (total) porosity data is collected, the (total) porosity of the saline formation can be used as a grid-based (wise) parameter using the results of three-dimensional geologic property modeling. The pressure (P), temperature (T), and salt mass fraction or concentration (groundwater salinity) (X_s) of the saline formation is used as a grid-based (wise). Thus, the j-phase CO_2 density $(\rho_{CO_2\,jp})$ of the saline formation is calculated at each grid and used as a grid-based (wise) parameter.

The time-independent fluid-phase CO_2 storage efficiency factor $E_{CO_2\,fp}$ in Eq. (2.2) reflects the fraction of the total (accessible) pore volume of the saline formation that will be occupied by lighter injected fluid-phase CO_2 (plume), which displaces (replaces) denser in situ (initial, resident) groundwater (body) and moves (accumulates) upward by density and mobility differences between injected fluid-phase CO_2 and in situ groundwater to the overlying top boundary of the saline formation (i.e., $0 \leq E_{CO_2\,fp} \leq 1$). In other words, it is not only dependent upon the net geologic pore volume (amount) for CO_2 storage but is also influenced by the injected fluid-phase CO_2 volume (shape), which is biggest at the end of CO_2 injection. Thus, it can be expressed as a multiplicative combination of seven geologic and displacement volumetric storage efficiency parameters (terms), which are also all between 0 and 1, as follows (NETL, 2007, 2008; IEA GHG, 2009; NETL, 2010, 2012, 2015):

$$\begin{aligned} E_{CO_2\,fp} &= E_{geol}\, E_{disp\,fp} = \left(E_{A_n/A_t}\, E_{h_n/h_g}\, E_{n_e/n_t}\right)\left(E_A\, E_L\, E_g\, E_d\right) \\ &= \left(E_{A_n/A_t}\, E_{A_n/A_t}\, E_{A_n/A_t}\right)\left(E_V\, E_d\right) \end{aligned} \tag{2.3}$$

where $E_{geol} = E_{A_n/A_t}\, E_{h_n/h_g}\, E_{n_e/n_t}$ is the intrinsic geologic storage efficiency parameter to define the percentage of the pore volume that is amenable to geologic CO_2 storage, and $E_{disp\,fp} = E_A\, E_L\, E_g\, E_d = E_V\, E_d$ is the fluid-phase CO_2 displacement storage efficiency parameter to define the percentage of the pore volume occupied by the fluid-phase CO_2 plume immediately (instantly) surrounding a single CO_2 injection well at the end of

CO_2 injection, when the fluid-phase CO_2 plume is biggest by definition (Figure 2.2). The end of CO_2 injection is the most favorable timing for the possible (probable) maximum size (volume) of the injected fluid-phase CO_2 plume minimizing (saturated) dissolution of CO_2 into groundwater. Here E_{A_n/A_t} is the net-to-total area ratio which is the fraction of total basin or region area with a suitable formation, E_{h_n/h_g} the net-to-gross thickness ratio which is the fraction of total geologic unit that meets minimum porosity and permeability requirements for injection, and E_{n_e/n_t} is the effective-to-total porosity ratio which is fraction of total porosity that is effective, while E_A is the areal (lateral) displacement efficiency, $E_L = E_I$ is the vertical (geologic layering) displacement efficiency, E_g is the gravity (buoyancy) displacement efficiency, $E_d = 1 - S_{wirr}$ is the microscopic (pore-scale) displacement efficiency in the CO_2 plume which is the fraction of pore space unavailable due to immobile in situ fluid, $E_V = E_A\ E_L\ E_g$ is the volumetric displacement efficiency which is the combined fraction of immediate volume surrounding an injection well that can be contacted by CO_2 and fraction of net thickness that is contacted by CO_2 as a consequence of the density difference between CO_2 and in situ water, and S_{wirr} is the irreducible (residual, immobile) water saturation. The shape of the injected fluid-phase CO_2 plume and the four displacement efficiency terms E_A, E_L, E_g, and E_d

are shown schematically in Figure 2.2 (NETL, 2010). Further details on the definitions, formulations, and determinations of the fluid-phase CO_2 storage efficiency parameters and factor in Eq. (2.3) are given by the works of NETL (2007, 2008), IEA GHG (2009), and NETL (2010, 2012, 2015). On the other hand, $C_{c\,CO_2\,fp} = E_{CO_2\,fp}/(1 - S_{wirr}) = E_{CO_2\,fp}/E_d = E_{geol}\,E_V = \left(E_{A_n/A_t}\,E_{h_n/h_g}\,E_{n_e/n_t}\right)(E_V)$ is the fluid-phase CO_2 storage capacity coefficient in the CSLF methodology (Bachu et al, 2007; CSLF, 2007, 2008; IEA GHG, 2009).

A series of Monte Carlo and numerical simulations has been performed using the commercial statistical programs such as GSLIB and GoldSim to estimate and compile highly reliable and broadly applicable probability ranges (databases) of the fluid-phase CO_2 storage efficiency parameters and factors for various saline formations in USA and Canada (NETL, 2007, 2008) as well as for more than 20,000 clastic (e.g., sandstone, mudstone, and conglomerate) and carbonate (limestone and dolomite) hydrocarbon (oil and gas) reservoirs as proxies for saline formations in USA, Canada, and other countries (i.e., Average Global Database (AGD)) (IEA GHG, 2009; NETL, 2010, 2012, 2015). When undocumented ranges of the storage efficiency parameters of the various saline formations in USA and Canada (NETL, 2007, 2008) were applied using uniform, normal, and mixed distributions, the P_{15},

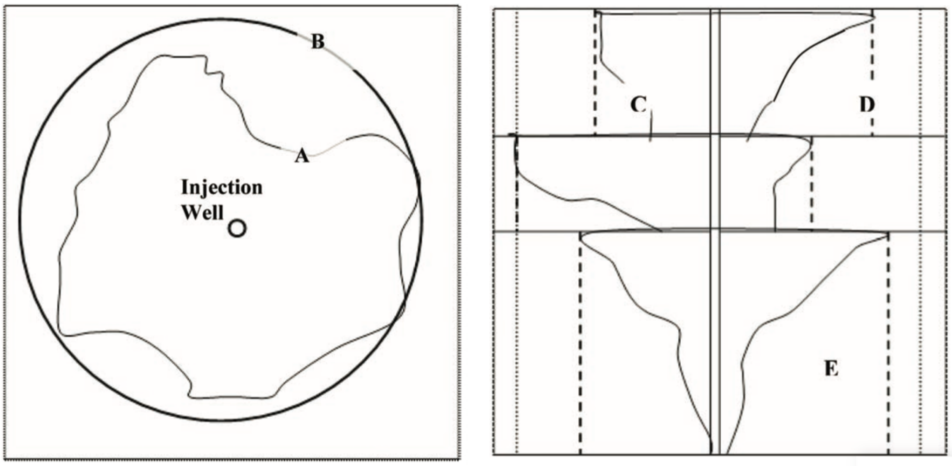

Figure 2.2. Schematic diagram of the fluid-phase CO_2 displacement storage efficiency parameter. Top- and side-views of injection CO_2 well and plume area (NETL, 2010).

P_{50}, and P_{85} percent probability ranges of the fluid-phase CO_2 storage efficiency factor were 1.0%, 2.0% (1.8% to 2.2%), and 4.0%, respectively (NETL, 2007, 2008). When the same undocumented ranges of the storage efficiency parameters of the various saline formations in USA and Canada (NETL, 2007, 2008) were applied using log-odds normal distributions, the P_{10}, P_{50}, and P_{90} percent probability ranges of the fluid-phase CO_2 storage efficiency factor were 0.51%, 2.0%, and 5.5%, respectively (NETL, 2010, 2012, 2015). On the other hand, when documented ranges of the storage efficiency parameters of the more than 20,000 clastic and carbonate hydrocarbon reservoirs in USA, Canada, and other countries (i.e., Average Global Database (AGD)) (IEA GHG, 2009) were applied using log-odds normal distributions and numerical simulations, the overall fluid-phase CO_2 storage efficiency factor ranges from 0.40% to 5.5% over the P_{10} and P_{90} percent probability range (IEA GHG, 2009; NETL, 2010, 2012, 2015). In particular, the P_{10}, P_{50}, and P_{90} percent probability ranges for the documented clastic hydrocarbon reservoirs were 0.51%, 2.0%, and 5.4%, respectively, and they are very similar to the above-mentioned P_{10}, P_{50}, and P_{90} percent probability ranges for the undocumented saline formations (i.e., 0.51%, 2.0%, and 5.5%, respectively) in USA and Canada (NETL, 2010, 2012, 2015). These probability ranges (databases) of the fluid-phase CO_2 storage efficiency parameters and factors of the saline formations in USA and Canada from the works of IEA GHG (2009), NETL (2010, 2012, 2015), and Goodman et al. (2011) have also been applied to the clastic saline formations in the other countries (e.g., Su et al., 2013; Sopher et al., 2014; Li et al., 2015).

If a saline formation has a simple geometry as a horizontal layer with a uniform thickness and homogeneous material properties (porosity and CO_2 density) and physico-chemical conditions (pressure and temperature), its theoretical and effective fluid-phase CO_2 storage capacities $M_{t\,CO_2\,jp}$ $[M]$ and $M_{e\,CO_2\,jp}$ $[M]$ in Eqs. (2.1) and (2.2) can be further approximated, respectively, as follows (Bachu et al., 2007; CSLF, 2007, 2008; NETL, 2007, 2008; IEA GHG, 2009; NETL, 2010, 2012, 2015):

$$M_{t\,CO_2\,jp} \approx V_t\, n_t\, \rho_{CO_2\,jp} = A_t\, h_g\, n_t\, \rho_{CO_2\,jp} \tag{2.4}$$

$$M_{e\,CO_2\,jp} \approx V_t\, n_t\, \rho_{CO_2\,jp}\, E_{CO_2\,jp} = A_t\, h_g\, n_t\, \rho_{CO_2\,jp}\, E_{CO_2\,jp} \tag{2.5}$$

where V_t is the total volume $[L^3]$ of the saline formation, n_t is the (total) porosity $[L^3/L^3]$ of the saline formation, $\rho_{CO_2\,jp}(P,T,X_s)$ is the j-phase CO_2 density $[M/L^3]$ at its equilibrium physico-chemical conditions (P,T,X_s), A_t is the total area $[L^2]$ of the saline formation, h_g is the gross thickness $[L]$ of the saline formation, and $E_{CO_2\ jp}$ is the formation-level j-phase CO_2 storage efficiency factor $[L^3/L^3]$ of the saline formation. The j-phase CO_2 density $\rho_{CO_2\ jp}$ is evaluated at pressure and temperature that represents storage conditions anticipated for the saline formation and averaged over V_t or h_g and A_t.

In order to clarify the concept of fluid-phase CO_2 storage capacity estimation, performed in this study, the procedure of grid-based Monte Carlo simulation is defined as a workflow chart (Figure 2.3). First, raw data such as pressure including atmosphere pressure and hydrostatic pressure (Figure 2.3a), temperature including onshore ground surface and offshore seafloor surface temperature and geothermal gradient (Figure 2.3b), TDS (Figure 2.3c), porosity (Figure 2.3d), volumes of geologic formations (Figure 2.3e), and storage efficiency (Figure 2.3f) is analyzed and computerized to use as basic computational input data for CO_2 storage capacity estimation. Individual gas-, liquid-, supercritical-, and whole fluid-phase CO_2 density (Figure 2.3g) at each grid is computed probabilistically using corresponding deterministic pressure and probabilistic temperature. Here the pressures at onshore region grids are computed using atmospheric pressure and hydrostatic pressure with depth from the ground surface, whereas the pressures at offshore region grids are computed using atmospheric pressure and hydrostatic pressure with depth from the sea level. The temperatures at onshore region grids are computed using onshore ground surface temperature and probabilistic geothermal gradient with depth from the ground surface, whereas the temperatures at the offshore region grids are computed using offshore seafloor surface temperature and probabilistic geothermal gradient with depth from the offshore seafloor surface. Individual gas-, liquid-, supercritical-, and whole fluid-phase CO_2 storage density (Figure 2.3h) is computed probabilistically using individual gas-, liquid-, supercritical-, and whole fluid-phase CO_2 density (Figure 2.3g) and porosity (Figure 2.3d). Theoretical individual gas-, liquid-, supercritical-, and whole fluid-phase CO_2 storage capacity estimation with grid-based Monte Carlo simulation (Figure 2.3i) is performed using individual gas-, liquid-, supercritical-, and whole fluid-phase CO_2 storage density (Figure 2.3h) and volumes of geologic formations (Figure 2.3e). And effective individual gas-, liquid-, supercritical-, and whole fluid-phase CO_2 storage capacity estimation with grid-based Monte Carlo simulation (Figure 2.3j) is performed using theoretical individual gas-, liquid-, supercritical-, and whole fluid-phase CO_2 storage capacity estimation with grid-based Monte Carlo simulation (Figure 2.3i) and CO_2 storage efficiency (Figure 2.3f).

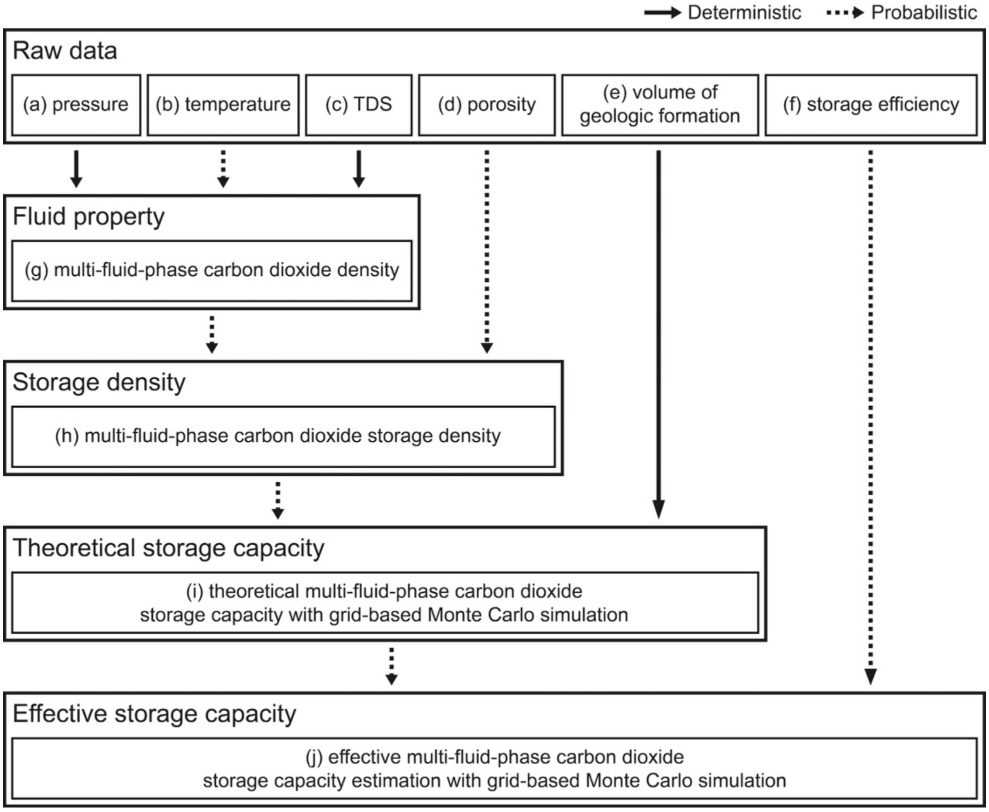

Figure 2.3. Workflow chart of fluid-phase carbon dioxide storage capacity estimation with grid-based Monte Carlo simulation of the Pohang Basin.

3. Study area

3.1. Location and geological settings

The study area includes the Pohang City, Gyeongju City, Yeongil Bay, Homi Cape, and surrounding onshore and offshore regions. It is located in the southeastern part of Korea and east longitude of 129°07’55”E to 129°41’18”E and in the north latitude of 35°52’10”N to 36°20’29”N (Figure 3.1). Most of the study area is geologically occupied by the so-called Tertiary Pohang Basin. The Pohang Basin has been identified as one of the most suitable sedimentary basins in Korea for commercial-scale geologic CO_2 storage.

In overall from the west to the east, the study area is composed of the Jurassic plutonic igneous rocks (Daebo Intrusives), Cretaceous clastic sedimentary rocks (Sindong Group and Hayang Group), volcanic igneous rocks (Yucheon Group), and plutonic igneous rocks (Bulguksa Intrusives), Tertiary (Paleogene) plutonic and volcanic igneous rocks, Tertiary (Neogene) clastic sedimentary rocks (Janggi Group and Yeonil Group), and Quaternary alluvium and marine sediments in ascending order (Um et al., 1964; Sohn et al., 2001; Sohn and Son, 2004) (Figure 3.1). The Tertiary Janggi Group and Yeonil Group constitute the so-called Pohang Basin, whereas the Cretaceous Sindong Group, Hayang Group, Yucheon Group, and Bulguksa Intrusives

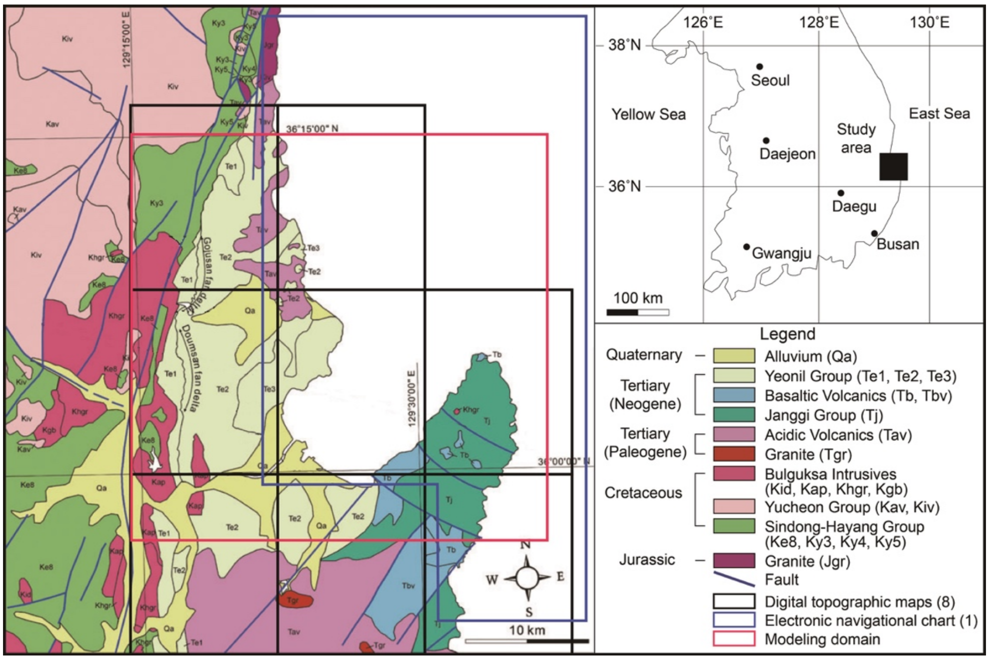

Figure 3.1. Location and surface (onshore) geologic maps of the Pohang Basin with modeling domain. The surface geologic map is modified from Um et al., (1964), Sohn et al., (2001), and Sohn and Son (2004).

constitute the so-called Gyeongsang Basin. In terms of areal distribution, the Tertiary Pohang Basin is major and distributed both onshore and offshore, whereas the Cretaceous Gyeongsang Basin is minor and distributed onshore only in the study area.

In more detail, based on various geophysical exploration (seismic and geomagnetic survey) and deep borehole logging databases (i.e., undocumented numeric data and imaginary files), the study area is subdivided into the six geologic formations such as the Cretaceous Basement and Tertiary (Paleogene) Volcanics (CBTV), Tertiary (Neogene) Primary and Resedimented Volcanics (PRSV), Fluvial Conglomerate and Sandstone (FCSS), Shallow Marine Sandstone (SMSS), Interlayered Sandstone and Mudstone (ISMS), and Marine Mudstone (MRMS) in ascending order (Yoon, 2013) (Figure 3.2). Tertiary (Neogene) Primary and Resedimented Volcanics (PRSV) belongs to the Janggi Group, while Fluvial Conglomerate and Sandstone (FCSS), Shallow Marine Sandstone (SMSS), Interlayered Sandstone and Mudstone (ISMS), and Marine Mudstone (MRMS) belong to the Yeonil Group.

The Pohang Basin becomes deeper and thicker northeastward, and its northeastern boundary has not yet been well identified. Thus, it has been considered as an open system (Figure 3.1). The geologic formations in the

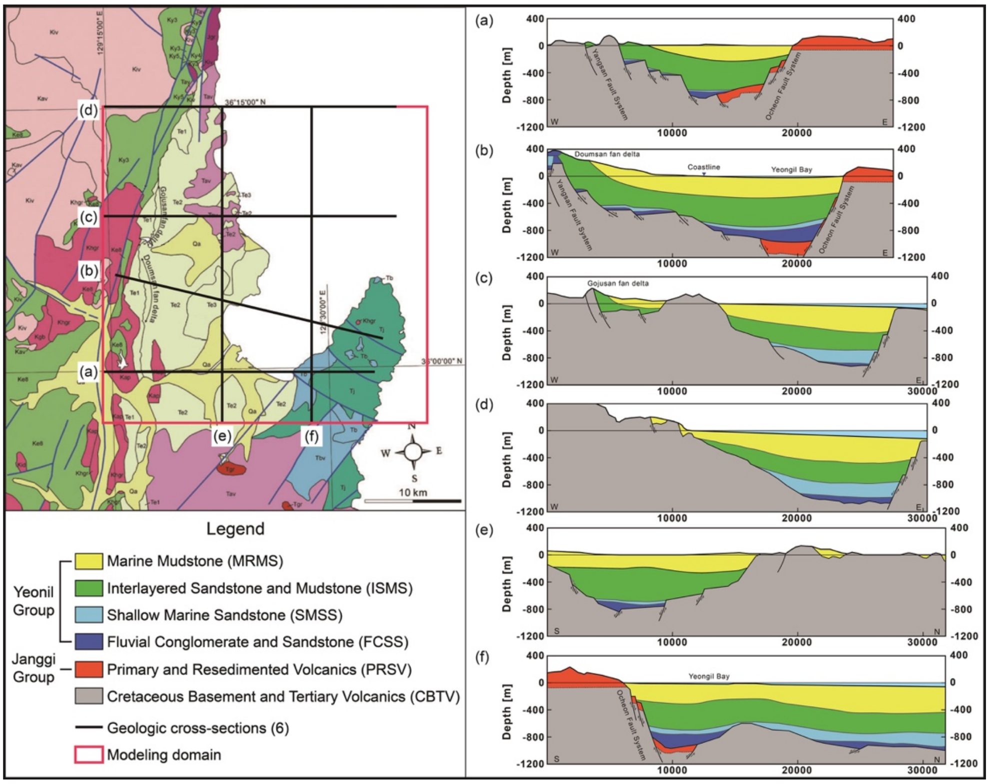

Figure 3.2. Geologic cross-sections of the Pohang Basin with geologic structures (major faults) and formations along (a) Line 1, (b) Line 2, (c) Line 3, (d) Line 4, (e) Line 5, and (f) Line 6 and their locations (Yoon, 2013).

study area are distributed very complicatedly both onshore and offshore with irregular depths and thicknesses (Figure 3.2). On the other hand, the geologic formations are partly dissected and offset by the Yangsan Fault System (Lee et al., 1999) and Ocheon Fault System (Cheon et al., 2012) (Figures 3.1 and 3.2).

3.2. Assignment of geologic formations for geologic carbon dioxide storage

On the basis of lithological and compositional characteristics, the six geologic formations (i.e., MRMS, ISMS, SMSS, FCSS, PRSV, and CBTV) in geologic CO_2 storage in the Pohang Basin are assigned the role for geologic CO_2 storage and summarized in Table 3.1. The overlying relatively thick MRMS (Marine Mudstone) and ISMS (Interlayered Sandstone and Mudstone) are mudstone (MS)-dominant and thus can serve as potential cap (seal) rocks for geologic CO_2 storage. The MRMS (Marine Mudstone) and ISMS (Interlayered Sandstone and Mudstone) are mostly have proper thickness for preventing leakage risk of CO_2 (i.e., stable geologic CO_2 storage) and favorable hydrogeological properties (i.e., low porosity and permeability). In the meantime, the underlying SMSS (Shallow Marine Sandstone) and FCSS (Fluvial Conglomerate and Sandstone) are sandstone (SS)-dominant and thus can act as potential reservoir (storage) rocks (clastic saline formations) for geologic CO_2 storage. The SMSS (Shallow Marine Sandstone) and FCSS (Fluvial Conglomerate and Sandstone) mostly have proper onshore and offshore depths for supercritical- and liquid-phase CO_2 conditions (i.e., more than about 800 m depth from the ground surface or sea level) and favorable hydrogeological properties (i.e., high porosity and permeability) for large amounts of CO_2 storage (Kim, J.C. et al., 2012, 2013). On the other hand, the lowermost PRSV (Tertiary (Neogene) Primary and Resedimented Volcanics) and CBTV (Cretaceous Basement and Tertiary (Paleogene) Volcanics) act as bedrocks.

Table 3.1. Geologic modeling output values of numbers of grid blocks, volumes, and volume fractions of the geologic formations in the Pohang Basin.

Geologic formation	Role in geologic CO_2 storage	Number of grid blocks[a]	Volume (km^3)	Volume fraction (%)
Marine Mudstone (MRMS)	Upper cap rock	60,000 (60,000)	148.49	9.32
Interlayered Sandstone and Mudstone (ISMS)	Lower cap rock	60,000 (33,852)	151.64	9.52
Shallow Marine Sandstone (SMSS)	Upper reservoir rock (clastic saline formation)	40,000 (14,840)	27.13	1.70
Fluvial Conglomerate and Sandstone (FCSS)	Lower reservoir rock (clastic saline formation)	40,000 (8,820)	17.00	1.07
Primary and Resedimented Volcanics (PRSV)	Upper bedrock	20,000 (4,740)	18.68	1.17
Cretaceous Basement and Tertiary Volcanics (CBTV)	Lower bedrock	40,000 (40,000)	1,229.88	77.22
Sum		260,000 (162,252)	1,592.82	100.00

[a] The numbers in the parentheses are the numbers of non-zero-volume grid blocks.

4. Three-dimensional geologic modeling

4.1. Three-dimensional geologic modeling setups

The following information data for the Pohang Basin are used as spatially distributed input data in three-dimensional geologic modeling using the geostatistical geologic modeling program GOCAD (Paradigm, 2014). The eight onshore (ground) digital topographic maps (Cheongha, Chilpo, Pohang, Hwanho, Daebo, Yeonil, Yongdeok, and Guryongpo) (NGII, 2013) and one offshore (seafloor) electronic navigational chart (Pohang Harbor Vicinity sheet) (KHOA, 2011) supply the information data of the spatial digital elevation model (DEM). The one surface (onshore) geologic map (Um et al., 1964; Sohn et al., 2001; Sohn and Son, 2004) (Figure 3.1) and six geologic cross-sections (four cross-sections in the east-west (EW) direction and two cross-sections in the north-south (NS) direction) (Yoon, 2013) (Figure 3.2) provide the information data of the spatial geologic structures and formations (Figure 4.1). Here the six geologic cross-sections was made by integration of previous works (Choi et al., 1993; Choi, 2006; Huntec Ltd., 1967; Yoon, 1994; Yoon and Chough, 1993; Yoon and Chough, 1995) including offshore region data such as seismic and ocean topography exploration data and onshore region data such as borehole data of the Pohang Basin.

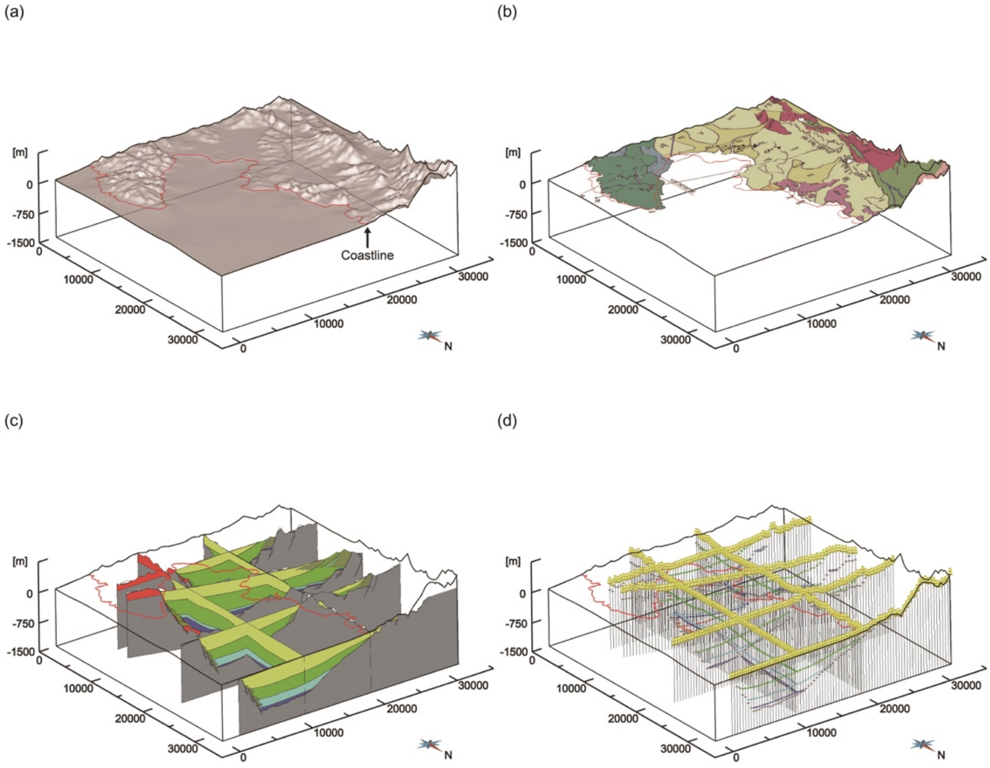

Figure 4.1. Three-dimensional spatial distributions of (a) geologic modeling domain with digital elevation model, (b) surface geologic map, (c) 6 offshore geologic cross-sections with geologic structures (faults) and formations, and (d) 464 virtual boreholes with geologic structures (faults) and formations in the Pohang Basin.

Considering the above-mentioned spatially distributed input data, the region of 32,600 m in the east-west (EW) direction, 31,800 m in the north-south (NS) direction, and up to the topographic high and down to 1,500 m from the sea level in the vertical direction is selected as the modeling domain to encompass mainly the Pohang Basin for its highly reliable three-dimensional geologic modeling (Figures 3.1 and 3.2). The modeling domain is located in the east longitude of 129°15’15”E to 129°37’47”E and in the north latitude of 35°56’47”N to 36°15’09”N (Figures 3.1 and 3.2).

4.2. Three-dimensional geologic models

4.2.1. Three-dimensional geologic structure model

The three-dimensional geologic structure model of the Pohang Basin is illustrated in Figure 4.2. As shown in the figure, the geologic structure model is composed of the eight major faults, which are obtained by means of the above-mentioned discrete smooth interpolation (DSI) technique. They belong to the Yangsan Fault System and Ocheon Fault System. The eight major faults are generally positioned in the north-south (NS) direction and partly dissect and offset the six geologic formations (i.e., CBTV, PRSV, FCSS, SMSS, ISMS, and MRMS) as shown in Figure 3.2. They are also implemented in the following three-dimensional geologic stratigraphy, grid, and formation

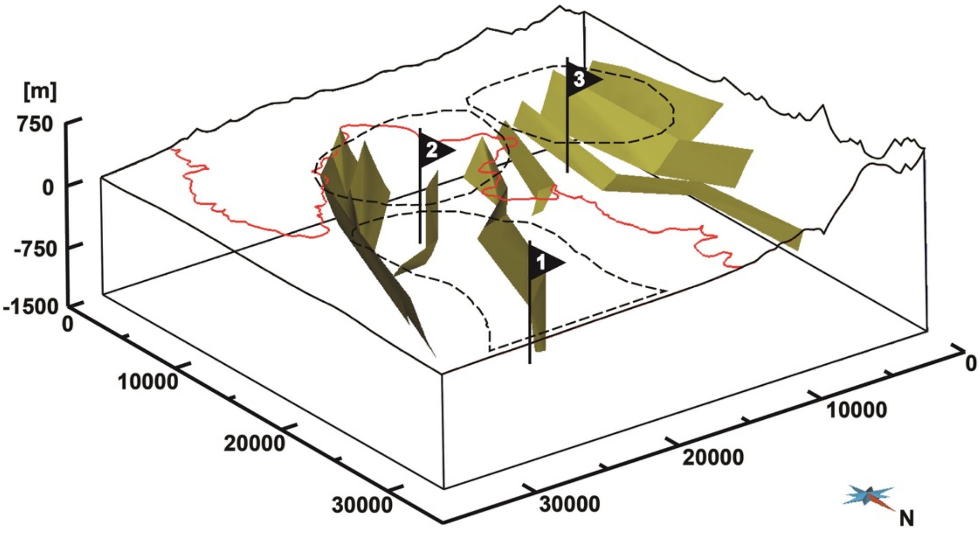

Figure 4.2. Three-dimensional geologic structure model of the Pohang Basin with the eight major faults (yellow surfaces).

models (Figures 4.3, 4.4, and 4.5, respectively). The three prospective areas for geologic CO_2 storage such as Areas 1, 2, and 3 marked in Figure 4.2 are explained in Sections 4.2.2 and 4.2.4. As shown in Figure 4.2, Area 1 is slightly dissected by the three major faults, whereas Areas 2 and 3 are highly dissected by the four and five major faults, respectively.

4.2.2. Three-dimensional geologic stratigraphy model

The three-dimensional geologic stratigraphy model of the Pohang Basin is illustrated in Figure 4.3. As shown in the figure, the geologic stratigraphy model is composed of the six geologic formation boundaries (more precisely the upper surfaces), which are obtained by means of the above-mentioned discrete smooth interpolation (DSI) technique. The six geologic formation boundaries are deep at the three prospective areas such as Area 1 (northeastern offshore area), Area 2 (southern offshore area near the Yeongil Bay), and Area 3 (western onshore area near the Pohang City) in the modeling domain. In particular, at Area 1, where the six geologic formation boundaries are deepest, the depths to the upper surfaces of the six geologic formations CBTV, PRSV, FCSS, SMSS, ISMS, and MRMS from the sea level are about 1,175 m, 1,025 m, 959 m, 771 m, 451 m, and 69 m, respectively. As shown in Figure 4.3, Area 1 is slightly dissected by the three major faults, whereas

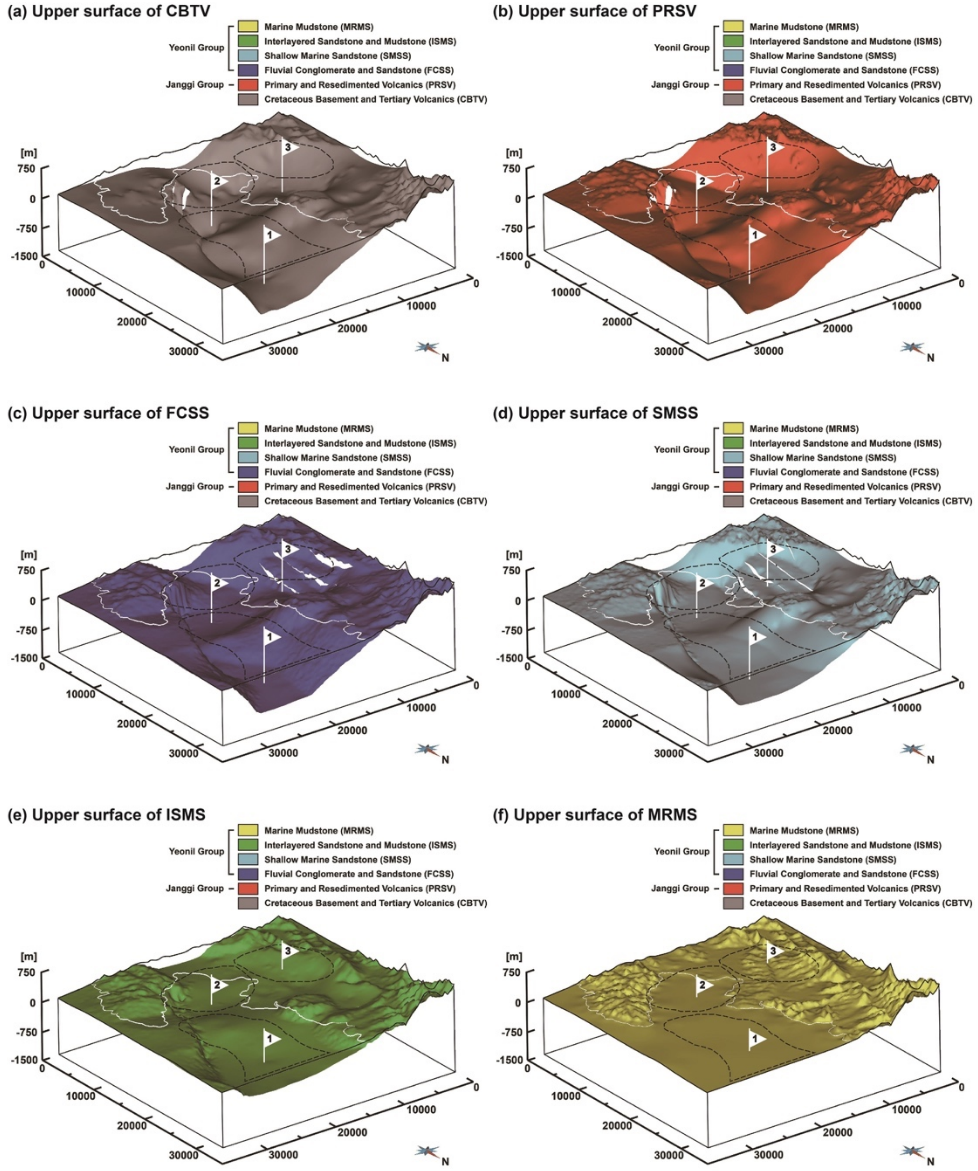

Figure 4.3. Three-dimensional geologic stratigraphy model of the Pohang Basin with upper surfaces of the six geologic formations (a) CBTV, (b) PRSV, (c) FCSS, (d) SMSS, (e) ISMS, and (f) MRMS.

Areas 2 and 3 are highly dissected by the four and five major faults, respectively.

4.2.3. Three-dimensional geologic grid model

The three-dimensional geologic grid model of the Pohang Basin is illustrated in Figure 4.4. As shown in the figure, the geologic grid model is composed of 260,000 hexahedral grid blocks (elements) (i.e., 100 × 100 × 26 in east-west, north-south, and vertical directions, respectively, including zero-volume (thickness) grid blocks), which are used to discretize the spaces between the eight major faults (Figure 4.2) and six geologic formation boundaries (Figure 4.3). The numbers of grid blocks of the six geologic formations are summarized in Table 3.1. As listed in the table, the CBTV (Lower bedrock), PRSV (Upper bedrock), FCSS (lower reservoir rock), SMSS (upper reservoir rock), ISMS (lower cap rock), and MRMS (upper cap rock) consist of 40,000, 4,740, 8,820, 14,840, 33,852, and 60,000 non-zero-volume hexahedral grid blocks (elements), respectively. The three prospective areas such as Areas 1, 2, and 3 marked in Figure 4.4 are explained in Sections 4.2.2 and 4.2.4.

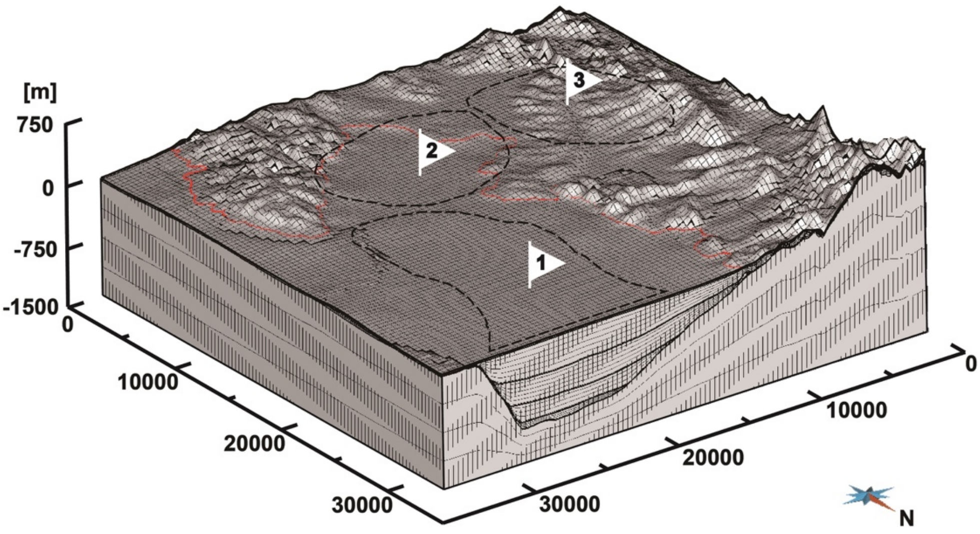

Figure 4.4. Three-dimensional geologic grid model of the Pohang Basin with 260,000 grid blocks and boundaries of the six geologic formations CBTV, PRSV, FCSS, SMSS, ISMS, and MRMS.

4.2.4. Three-dimensional geologic formation model

The three-dimensional geologic formation model of the Pohang Basin is illustrated in Figure 4.5. As shown in the figure, the geologic formation model is composed of the six geologic formations, which are obtained by means of polymerization of the preceding three-dimensional geologic structure, stratigraphy, and grid models (Figures 4.1, 4.2, and 4.3, respectively). The six geologic formations are distributed very complicatedly both onshore and offshore with irregular depths and thicknesses, and they are partly dissected and offset by the eight major faults (Figures 4.1 and 4.2) as mentioned in Figure 3.2. The five geologic formations except the lowermost bedrock CBTV are deep and thick at the three prospective areas such as Areas 1, 2, and 3 in the modeling domain. In particular, at Area 1, where the five geologic formations are deepest and thickest, the thicknesses of the five geologic formations PRSV, FCSS, SMSS, ISMS, and MRMS are about 150 m, 66 m, 188 m, 320 m, and 382 m, respectively. The volumes and volume fractions of the six geologic formations are summarized in Table 3.1. As listed in the table, the volumes (volume fractions) of the FCSS (lower reservoir rock), SMSS (upper reservoir rock), ISMS (lower cap rock), and MRMS (upper cap rock) are 17.00 km^3 (1.07%), 27.13 km^3 (1.70%), 151.64 km^3 (9.52%), and 148.49 km^3 (9.32%), respectively.

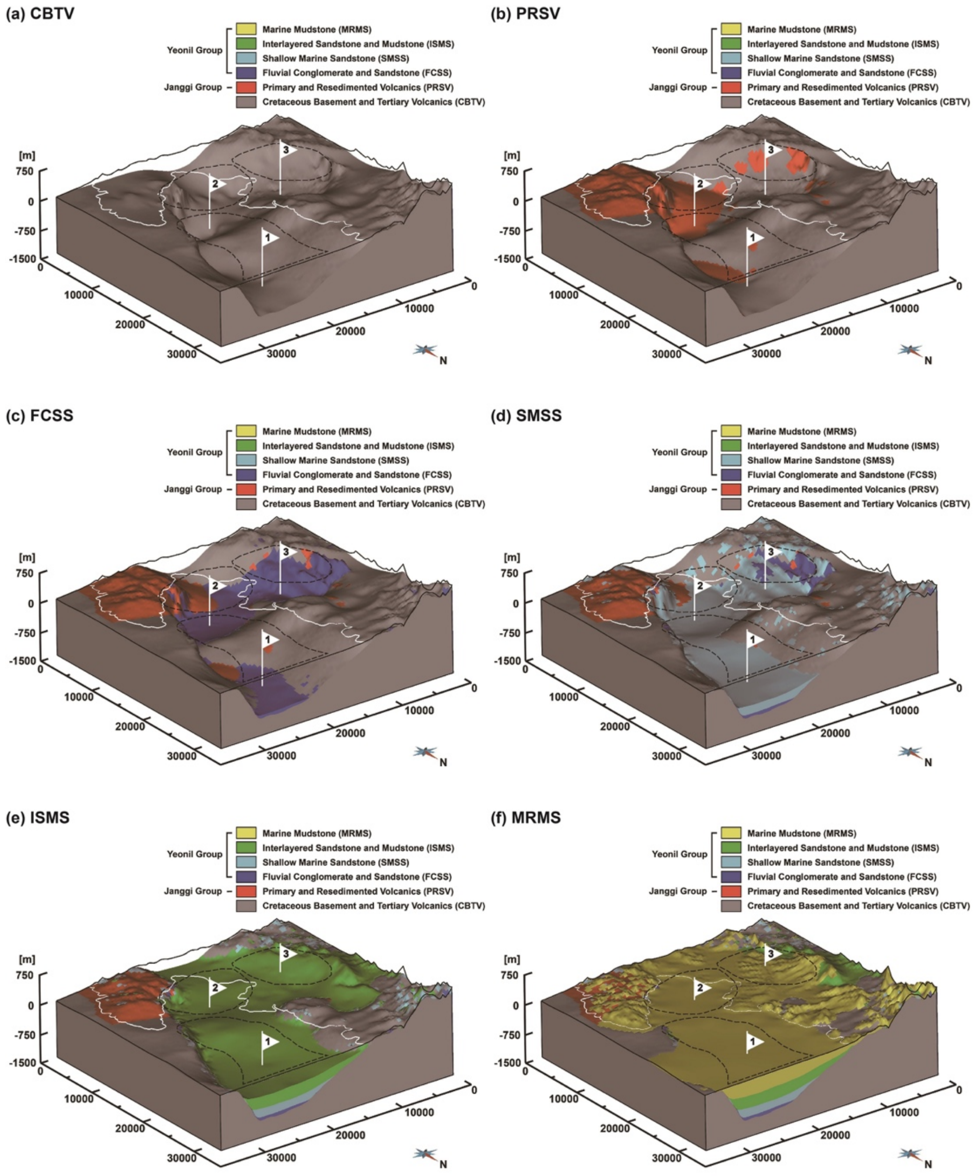

Figure 4.5. Three-dimensional geologic formation model of the Pohang Basin with the six geologic formations (a) CBTV, (b) PRSV, (c) FCSS, (d) SMSS, (e) ISMS, and (f) MRMS.

5. Fluid-phase carbon dioxide storage capacity estimation

5.1. Grid-based Monte Carlo simulation setups

The grid information data (i.e., geometry, location, and volume) of the two clastic saline formations (i.e., SMSS and FCSS) in the Pohang Basin are adopted from the preceding three-dimensional geologic models (Figures 4.1, 4.2, 4.3, and 4.4 and Table 3.1) through the grid information data conversion model Grid Converter (Kim, C.S. et al., 2013). They are then used as formation-specific input data for Eqs. (2.1) and (2.2) (Section 2.2) in grid-based Monte Carlo simulation using the probabilistic theoretical and effective fluid-phase CO_2 storage capacity evaluation model CO_2-STOR (Kihm et al., 2017).

The (total) porosities of the two clastic saline formations (i.e., SMSS and FCSS) in the Pohang Basin are adopted from the works of Huh et al. (1992), Kim, J.C. et al. (2012, 2013), Park et al. (2013), and Park and Park (2016) (Table 5.1) and used as formation-specific input data for Eqs. (2.1) and (2.2) (Section 2.2) in grid-based Monte Carlo simulation. Here the probabilistic distributions of the (total) porosities are assumed to have truncated normal distributions, which can represent normal distributions and do not allow the

Table 5.1. Monte Carlo simulation input values of total porosities of the clastic saline formations and geothermal gradient in the Pohang Basin.

Parameter	Total porosity		Geothermal gradient (°C/km)
	SMSS[a]	FCSS[b]	Pohang Basin[c]
Number of data	6	5	8
Minimum	0.0818	0.0628	23.37
Maximum	0.2797	0.3150	27.99
Mean	0.2254	0.2339	26.07
Standard deviation	0.0723	0.0901	1.31

[a] The three data are from Huh et al. (1992), and the three data are from Park et al. (2013).

[b] The two data are from Kim, J.C. et al. (2012, 2013), and the three data are from Park and Park (2016).

[c] The eight data are from Kim and Lee (2007).

(total) porosities to exceed the range of raw data.

The linear vertical hydrostatic pressure gradient ($\Delta P/\Delta z$), linear vertical geothermal gradient ($\Delta T/\Delta z$), and uniform salt mass fraction or concentration (groundwater salinity) (X_s) are adopted to obtain spatially distributed pressure and temperature in the two clastic saline formations (i.e., SMSS and FCSS). They are then used as independent input data (variables) for calculating the fluid-phase CO_2 density and identifying the corresponding CO_2 fluid phase type in grid blocks or at grid block centers for Eqs. (2.1) and (2.2) (Section 2.2) in grid-based Monte Carlo simulation. Here the atmospheric pressure, onshore ground surface temperature, offshore seafloor surface temperature, groundwater salinity, and gravitational acceleration are set equal to 1.0 atm (101,325 Pa), 15.0°C (KMA, 2011), 11.0°C (Na et al., 1991), 35,000 ppm (normal seawater salinity equivalent to seawater density of 1,025 kg/m^3), and 9.81 m/sec^2, respectively. The geothermal gradient is adopted from the work of Kim and Lee (2007) (Table 5.1) and used as basin-specific input data. Here it is assumed that the geothermal gradient is represented by a truncated normal distribution.

On the other hand, the five fluid-phase CO_2 storage efficiency parameters (terms) (i.e., E_{A_n/A_t}, E_{h_n/h_g}, E_{n_e/n_t}, E_V, and E_d) of the two clastic saline formations are adopted from the works of NETL (2007, 2008) and IEA GHG

(2009) (Table 5.2) and used as general input data for calculating the intrinsic geologic storage efficiency parameter E_{geol}, fluid-phase CO_2 displacement storage efficiency parameter $E_{disp\ fp}$, and fluid-phase CO_2 storage efficiency factor $E_{CO_2\ fp}$ for Eqs. (2.2) and (2.3) (Section 2.2) in grid-based Monte Carlo simulation. Here it is assumed that the five fluid-phase CO_2 storage efficiency parameters are represented using log-odds normal (logistic-normal) distributions (Aitchison and Shen, 1980) as in the works of NETL (2010, 2012, 2015). The grid-based Monte Carlo simulation is performed 1,000 times.

5.2. Probability density distributions of input data

The probability density distributions of the (total) porosities of the two clastic saline formations SMSS and FCSS in the Pohang Basin are plotted in Figures 5.1a and 5.1b, respectively, and summarized in Table 5.3. As shown in the figures and table, they all show truncated normal distributions and meet very well their original (input) statistical values listed in Table 5.1. In addition, they are very similar to each other.

The probability density distribution of the geothermal gradient in the Pohang Basin is plotted in Figure 5.1c and summarized in Table 5.3. As shown in the figure and table, it also shows a truncated normal distribution

Table 5.2. Monte Carlo simulation input values of fluid-phase CO_2 storage efficiency parameters of the clastic saline formations in the Pohang Basin.

Parameter	P_{10} value	P_{90} value
Intrinsic geologic storage efficiency parameter		
Net-to-total area ratio E_{A_n/A_t}[a]	0.20	0.80
Net-to-gross thickness ratio E_{h_n/h_g}[b]	0.21	0.76
Effective-to-total porosity ratio E_{n_e/n_t}[b]	0.64	0.77
Fluid-phase CO_2 displacement storage efficiency parameter		
Volumetric displacement efficiency E_V[c]	0.16	0.39
Microscopic displacement efficiency E_d[c]	0.35	0.76

[a] The data are from NETL (2007, 2008).

[b] The data are from the Average Global Database (AGD) in IEA GHG (2009).

[c] The data are from the numerical simulations in IEA GHG (2009).

(a) Total porosity of SMSS

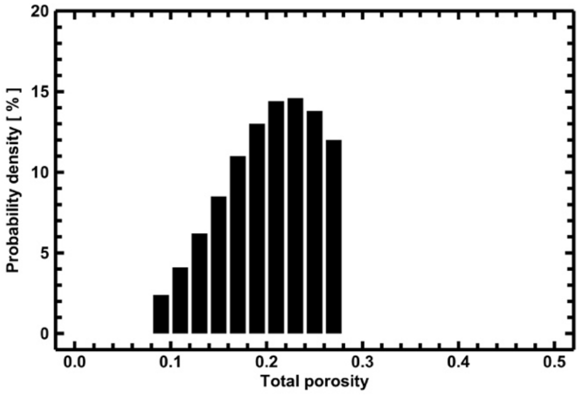

(b) Total porosity of FCSS

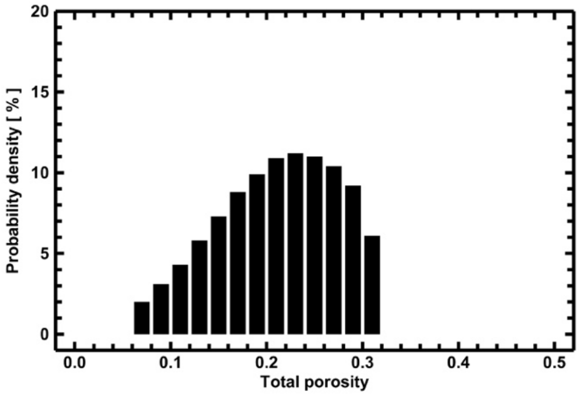

(c) Geothermal gradient of Pohang Basin

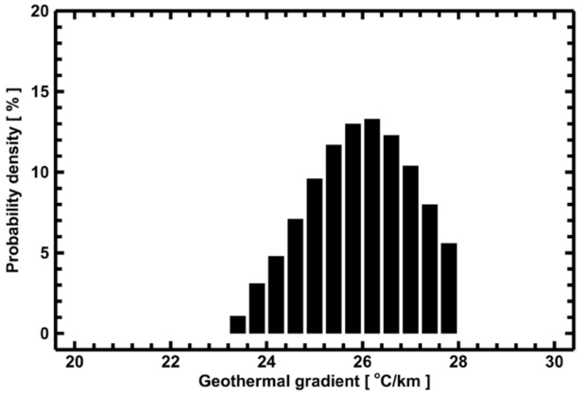

Figure 5.1. Probability density distributions of total porosities of the clastic saline formations (a) SMSS and (b) FCSS and (c) geothermal gradient in the Pohang Basin.

Table 5.3. Monte Carlo simulation output values of total porosities of the clastic saline formations and geothermal gradient in the Pohang Basin.

Parameter	Total porosity		Geothermal gradient (°C/km)
	SMSS	FCSS	Pohang Basin
Number of data[a]	1,000	1,000	1,000
Minimum ($P_{0.1}$)	0.0826	0.0629	23.39
P_{10} value	0.1321	0.1219	24.46
First quartile (P_{25})	0.1673	0.1658	25.17
Median (P_{50})	0.2067	0.2163	25.98
Third quartile (P_{75})	0.2411	0.2612	26.76
P_{90} value	0.2629	0.2911	27.36
Maximum (P_{100})	0.2796	0.3148	27.98
Mean	0.2017	0.2110	25.94
Standard deviation	0.0482	0.0620	1.07

[a] The number of data is equal to the number of Monte Carlo simulations.

and meets very well its original (input) statistical values listed in Table 5.1.

The pressure and temperature at the grid block centers in the two clastic saline formations SMSS and FCSS in the Pohang Basin under the probabilistically various geothermal gradients (i.e., minimum, first quartile, median, third quartile, and maximum) are plotted in Figures 5.2a and 5.2b, respectively, with the fluid-phase CO_2 density contours and phase boundaries. As shown in the figures, the pressure and temperature are distributed as narrow wedge-shaped bands from the shallowest grid block centers (near the onshore ground surface and offshore seafloor surface) down to the deepest grid block centers (near the lowermost bottom surfaces of the saline formations). Such wedge-shaped distributions arise because the single deterministic hydrostatic pressure gradient and various probabilistic linear geothermal gradients are adopted in this study as mentioned in Section 5.1. The figures also show that, in both saline formations, CO_2 exists as gas, liquid, and supercritical phases with the corresponding distinctive density ranges depending on the pressure and temperature with depth.

As a particular case from Figure 5.2, the probability density distributions of the gas-, liquid-, and supercritical-phase CO_2 densities in the two clastic saline formations SMSS and FCSS in the Pohang Basin under the median geothermal gradient are plotted in the left and right columns of Figure 5.3,

(a) SMSS

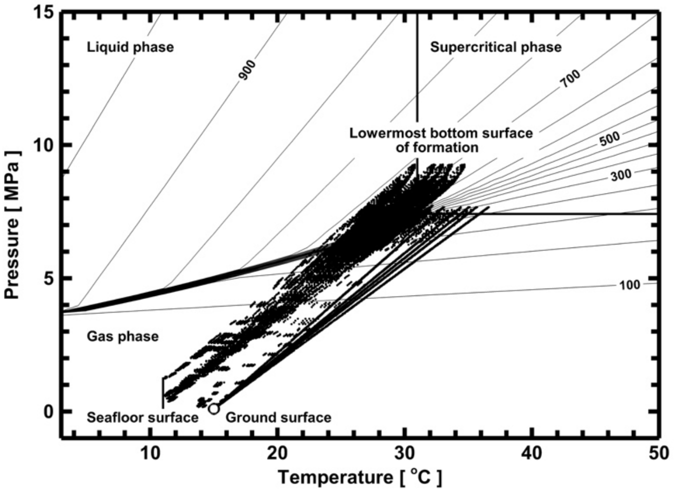

(b) FCSS

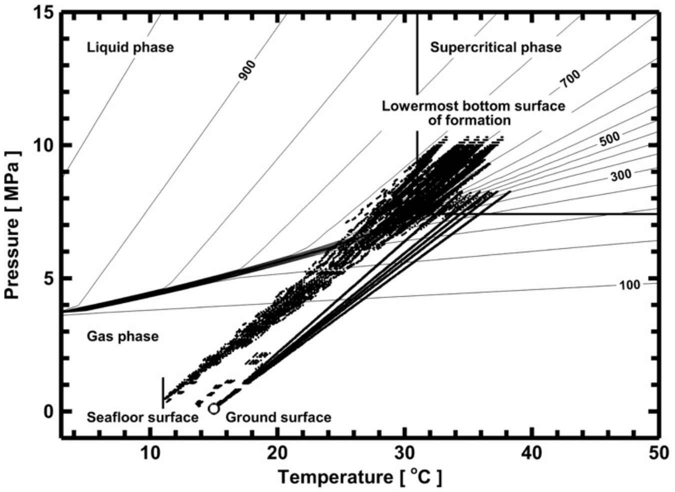

Figure 5.2. Pressure and temperature distributions at the grid block centers in the clastic saline formations (a) SMSS and (b) FCSS in the Pohang Basin under the minimum (most left), first quartile, median, third quartile, and maximum (most right) geothermal gradients. The phase boundaries are adopted from Pruess (2005).

respectively, and summarized in Table 5.4. As shown in the figure and table, in the shallower grid blocks (closer to the onshore ground surface and offshore seafloor surface) within both saline formations, CO_2 exists as a gas phase (Figures 5.3a and 5.3b and the first and fourth columns of Table 5.4) with the lower and wider density ranges. However, in the deeper grid blocks (closer to the lowermost bottom surfaces of the saline formations) within both saline formations, CO_2 exists as liquid phase (Figures 5.3c and 5.3d and the second and fifth columns of Table 5.4) and supercritical phase (Figures 5.3e and 5.3f and the third and sixth columns of Table 5.4) with the higher and narrower density ranges. The supercritical-phase CO_2 even shows bimodal density ranges within both saline formations. In addition, in the deeper grid blocks within the overlying saline formation SMSS, the liquid-phase CO_2 is more dominant than the supercritical-phase CO_2. However, in the deeper grid blocks within the underlying saline formation FCSS, the supercritical-phase CO_2 is more dominant than the liquid-phase CO_2.

The probability density distributions of the intrinsic geologic storage efficiency parameter E_{geol}, fluid-phase CO_2 displacement storage efficiency parameter $E_{disp\,fp}$, and fluid-phase CO_2 storage efficiency factor $E_{CO_2\,fp}$, which are calculated using Eq. (2.3) (Section 2.2), of the two clastic saline formations SMSS and FCSS in the Pohang Basin are plotted in Figures 5.4a,

Table 5.4. Monte Carlo simulation output values of gas-, liquid-, and supercritical-phase CO_2 densities in the clastic saline formations in the Pohang Basin under the median geothermal gradient.

Parameter	SMSS (kg/m^3)			FCSS (kg/m^3)		
	Gas phase	Liquid phase	Supercritical phase	Gas phase	Liquid phase	Supercritical phase
Number of grid blocks[a]	9,726	4,036	1,078	4,112	1,031	3,677
Volume of grid blocks (km^3)[b]	10.72	12.11	4.30	8.66	1.75	6.59
Volume fraction of grid blocks (%)[c]	39.51	44.64	15.85	50.94	10.29	38.77
Minimum ($P_{<0.10}$)	2.32	485.46	270.37	2.78	560.78	270.81
P_{10} value	7.19	613.80	287.77	38.94	604.78	373.20
First quartile (P_{25})	50.07	640.71	687.89	87.30	622.02	668.76
Median (P_{50})	157.69	672.99	694.08	155.95	652.90	694.68
Third quartile (P_{75})	217.17	687.02	701.22	211.10	662.42	699.50
P_{90} value	257.93	696.88	707.36	246.91	679.73	706.70
Maximum (P_{100})	435.40	713.37	714.92	436.73	712.91	716.30
Mean	142.45	663.04	622.63	149.35	644.90	643.59
Standard deviation	93.36	31.85	157.58	77.23	28.83	122.01

[a] The total number of grid blocks for each saline formation is equal to the corresponding number of non-zero-volume grid blocks listed in Table 3.1.

[b] The total volume of grid blocks for each saline formation is equal to the corresponding volume listed in Table 3.1.

[c] The total volume fraction of grid blocks for each saline formation is equal to 100%.

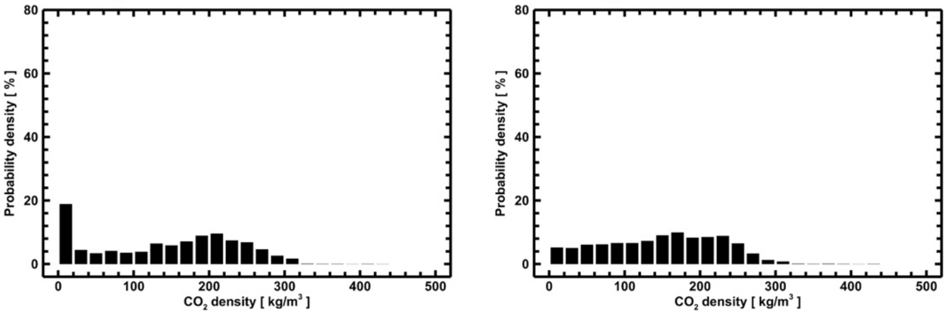

(a) Gas-phase CO$_2$ density in SMSS

(b) Gas-phase CO$_2$ density in FCSS

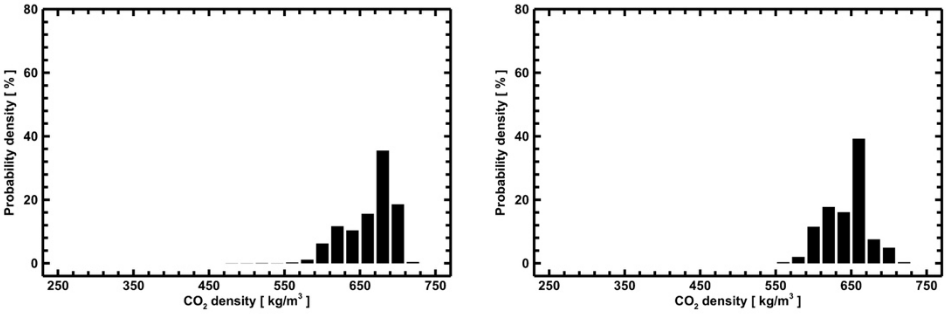

(c) Liquid-phase CO$_2$ density in SMSS

(d) Liquid-phase CO$_2$ density in FCSS

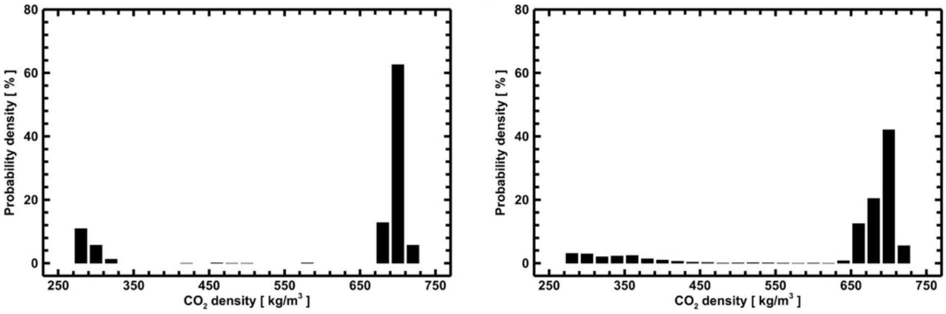

(e) Supercritical-phase CO$_2$ density in SMSS

(f) Supercritical-phase CO$_2$ density in FCSS

Figure 5.3. Probability density distributions of (a and b) gas-phase, (c and d) liquid-phase, and (e and f) supercritical-phase CO$_2$ densities in the clastic saline formations (left) SMSS and (right) FCSS in the Pohang Basin under the median geothermal gradient.

5.4b, and 5.4c, respectively, and summarized in Table 5.5. As shown in the figures and table, they all show log-normal distributions because they are expressed as multiplicative combinations of the five fluid-phase CO_2 storage efficiency parameters (terms) E_{A_n/A_t}, E_{h_n/h_g}, E_{n_e/n_t}, E_V, and E_d, which all show log-odds normal (logistic-normal) distributions as mentioned in Section 5.1. In addition, as shown in Table 5.5, the five fluid-phase CO_2 storage efficiency parameters meet very well the original (input) statistical values, which are listed in Table 5.2. In particular, as shown in Table 5.5, the P_{10}, P_{50}, and P_{90} values of the fluid-phase CO_2 storage efficiency factor are 0.58%, 2.00%, and 5.06%, respectively. They are very similar to those of the undocumented saline formations (i.e., 0.51%, 2.0%, and 5.5%, respectively) and the documented clastic saline formations (i.e., 0.51%, 2.0%, and 5.4%, respectively), which were estimated by Monte Carlo simulation using the commercial statistical program GoldSim, in the works of NETL (2010, 2012, 2015) (Section 2.2).

5.3. Probability density distributions of fluid-phase carbon dioxide storage capacities

The probability density distributions of the theoretical individual gas-, liquid-, supercritical-, and whole fluid-phase CO_2 storage capacities, which

(a) Intrinsic geologic storage efficiency parameter

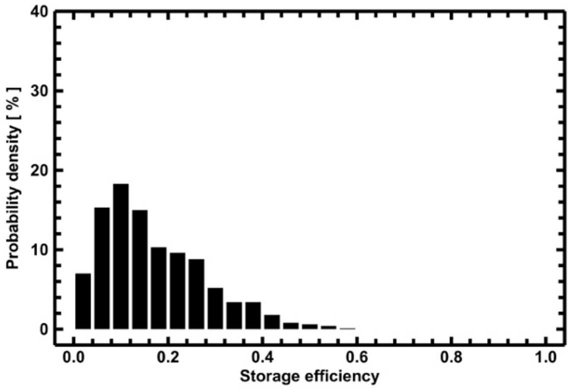

(b) Fluid-phase CO_2 displacement storage efficiency parameter

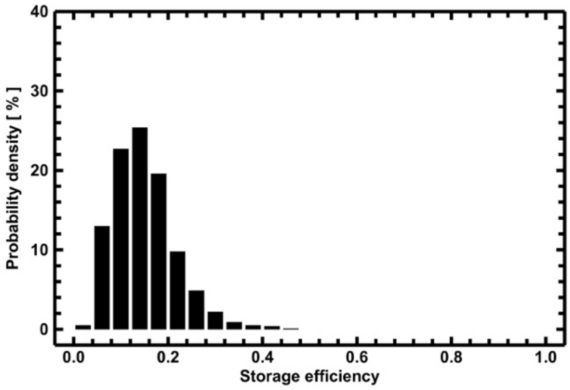

(c) Fluid-phase CO_2 storage efficiency factor

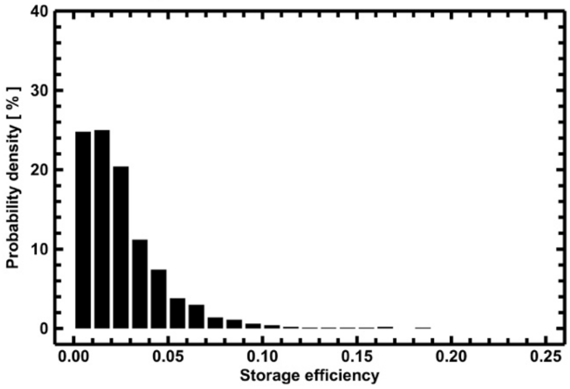

Figure 5.4. Probability density distributions of (a) intrinsic geologic storage efficiency parameter, (b) fluid-phase CO_2 displacement storage efficiency parameter, and (c) fluid-phase CO_2 storage efficiency factor of the clastic saline formations SMSS and FCSS in the Pohang Basin.

Table 5.5. Monte Carlo simulation output values of fluid-phase CO_2 storage efficiency parameters and factor of the clastic saline formations in the Pohang Basin.

Parameter	E_{A_n/A_t}[a]	E_{h_n/h_g}[b]	E_{n_e/n_t}[c]	E_V[d]	E_d[e]	E_{geol}[f]	$E_{disp\ fp}$[g]	$E_{CO_2\ fp}$[h]
Number of data[i]	1,000	1,000	1,000	1,000	1,000	1,000	1,000	1,000
Minimum ($P_{0.1}$)	0.0297	0.0172	0.4909	0.0690	0.1287	0.0056	0.0253	0.0004
P_{10} value	0.1991	0.2091	0.6397	0.1596	0.3496	0.0469	0.0737	0.0058
First quartile (P_{25})	0.3244	0.3229	0.6736	0.2022	0.4500	0.0861	0.1019	0.0102
Median (P_{50})	0.4999	0.4781	0.7092	0.2587	0.5662	0.1434	0.1407	0.0200
Third quartile (P_{75})	0.6748	0.6376	0.7424	0.3242	0.6754	0.2363	0.1837	0.0335
P_{90} value	0.7994	0.7597	0.7699	0.3897	0.7596	0.3239	0.2337	0.0506
Maximum (P_{100})	0.9793	0.9676	0.8461	0.6346	0.9199	0.5803	0.4430	0.1878
Mean	0.5000	0.4820	0.7067	0.2683	0.5599	0.1694	0.1495	0.0256
Standard deviation	0.2205	0.2033	0.0508	0.0900	0.1546	0.1088	0.0657	0.0223

[a] Net-to-total area ratio

[b] Net-to-gross thickness ratio

[c] Effective-to-total porosity ratio

[d] Volumetric displacement efficiency

[e] Microscopic displacement efficiency

[f] Intrinsic geologic storage efficiency parameter

[g] Fluid-phase CO_2 displacement storage efficiency parameter

[h] Fluid-phase CO_2 storage efficiency factor

[i] The number of data is equal to the number of Monte Carlo simulations.

are calculated using Eq. (2.1) (Section 2.2), of the two clastic saline formations SMSS and FCSS in the Pohang Basin are plotted in Figures 5.5 and 5.6, respectively, and summarized in Tables 5.6 and 5.7, respectively. In overall, they all show asymmetric normal distributions with the right (positive) (i.e., mean $>$ median) or left (negative) (i.e., mean $<$ median) skewness in different degrees. This arises because the fluid-phase CO_2 density and the corresponding CO_2 fluid phase type change across the phase boundaries as the geothermal gradient varies from the minimum to maximum as shown in Figures 5.2 and 5.3 and Table 5.4. In particular (as mentioned in Section 5.2), in the deeper grid blocks within the overlying saline formation SMSS, the liquid-phase CO_2 is more dominant than the supercritical-phase CO_2. However, in the deeper grid blocks within the underlying saline formation FCSS, the supercritical-phase CO_2 is more dominant than the liquid-phase CO_2.

As shown in Figures 5.5a, 5.5b, and 5.5c and the first, second, and third columns of Table 5.6, in the overlying saline formation SMSS, the theoretical liquid-phase (Figure 5.5b), supercritical-phase (Figure 5.5c), and gas-phase (Figure 5.5a) CO_2 storage capacities are probabilistically higher, intermediate, and lower with the mean values of 1,566.65 Mton, 546.43 Mton, and 398.52 Mton, respectively. This arises because, in the overlying saline formation

SMSS, the volumes occupied by the liquid- and gas-phase CO_2, respectively, are very similar to each other and greater than the volume occupied by the supercritical-phase CO_2, while the liquid- and supercritical-phase CO_2 densities are very close to each other and much greater than the gas-phase CO_2 density in the SMSS as mentioned in Table 5.4.

However, as shown in Figures 5.6a, 5.6b, and 5.6c and the first, second, and third columns of Table 5.7, in the underlying saline formation FCSS, the theoretical supercritical-phase (Figure 5.6c), gas-phase (Figure 5.6a), and liquid-phase (Figure 5.6b) CO_2 storage capacities are probabilistically higher, intermediate, and lower with the mean values of 846.21 Mton, 270.83 Mton, and 253.87 Mton, respectively. This arises because, in the underlying saline formation FCSS, the volumes occupied by the gas- and supercritical-phase CO_2, respectively, are somewhat similar to each other and greater than the volume occupied by the liquid-phase CO_2, while the liquid- and supercritical-phase CO_2 densities are very close to each other and much greater than the gas-phase CO_2 density in the FCSS as mentioned in Table 5.4.

As a whole, as shown in Figures 5.5d and 5.6d and the fourth column of Tables 5.6 and 5.7, respectively, the theoretical fluid-phase CO_2 storage capacity is probabilistically higher in the overlying saline formation SMSS (Figure 5.5d) compared with the underlying saline formation FCSS (Figure

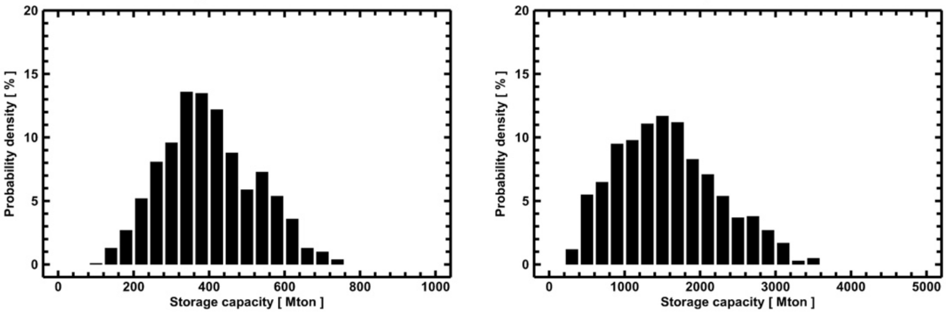

(a) Theoretical gas-phase CO_2 storage capacity

(b) Theoretical liquid-phase CO_2 storage capacity

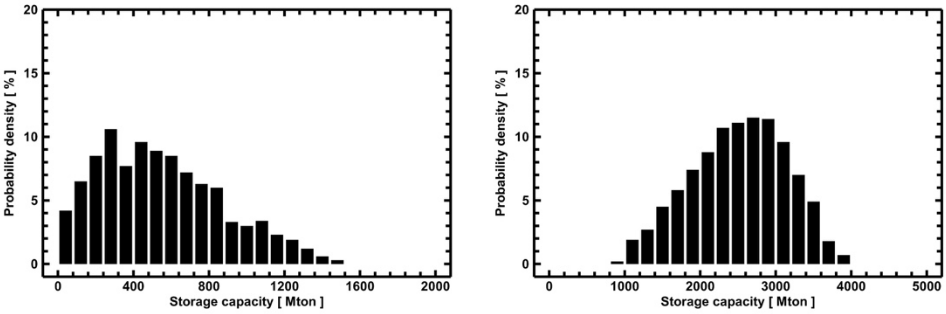

(c) Theoretical supercritical-phase CO_2 storage capacity

(d) Theoretical fluid-phase CO_2 storage capacity

Figure 5.5. Probability density distributions of theoretical (a) gas-phase, (b) liquid-phase, (c) supercritical-phase, and (d) fluid-phase CO_2 storage capacities of the clastic saline formation SMSS in the Pohang Basin.

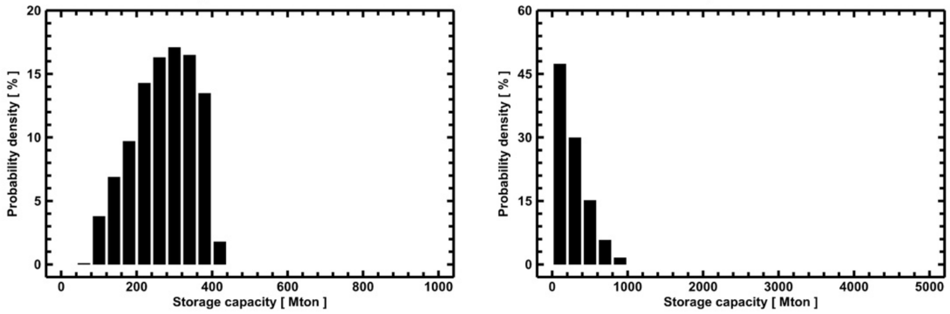

(a) Theoretical gas-phase CO_2 storage capacity

(b) Theoretical liquid-phase CO_2 storage capacity

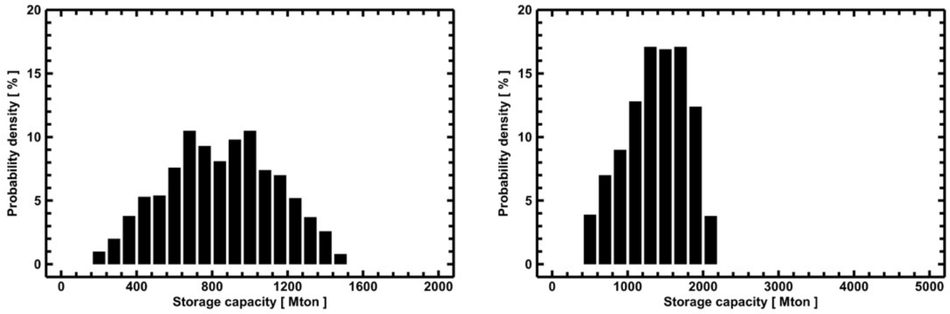

(c) Theoretical supercritical-phase CO_2 storage capacity

(d) Theoretical fluid-phase CO_2 storage capacity

Figure 5.6. Probability density distributions of theoretical (a) gas-phase, (b) liquid-phase, (c) supercritical-phase, and (d) fluid-phase CO_2 storage capacities of the clastic saline formation FCSS in the Pohang Basin.

Table 5.6. Monte Carlo simulation output values of theoretical gas-, liquid-, supercritical-, and fluid-phase CO_2 storage capacities of the clastic saline formation SMSS in the Pohang Basin.

Parameter	SMSS (Mton)			
	Gas phase	Liquid phase	Supercritical phase	Fluid phase
Number of data[a]	1,000	1,000	1,000	1,000
Minimum ($P_{0.1}$)	119.98	234.95	9.91	938.18
P_{10} value	242.56	712.69	150.94	1,620.82
First quartile (P_{25})	309.72	1,067.90	279.12	2,046.48
Median (P_{50})	387.13	1,510.15	508.08	2,545.89
Third quartile (P_{75})	479.72	2,011.56	761.21	2,982.80
P_{90} value	567.00	2,536.25	1,032.18	3,319.64
Maximum (P_{100})	743.46	3,554.05	1,472.51	3,952.83
Mean	398.52	1,566.65	546.43	2,511.60
Standard deviation	122.38	676.54	326.13	629.51

[a] The number of data is equal to the number of Monte Carlo simulations.

Table 5.7. Monte Carlo simulation output values of theoretical gas-, liquid-, supercritical-, and fluid-phase CO_2 storage capacities of the clastic saline formation FCSS in the Pohang Basin.

Parameter	FCSS (Mton)			
	Gas phase	Liquid phase	Supercritical phase	Fluid phase
Number of data[a]	1,000	1,000	1,000	1,000
Minimum ($P_{0.1}$)	79.99	1.61	171.59	410.41
P_{10} value	157.10	24.29	445.66	784.88
First quartile (P_{25})	212.28	81.68	639.48	1,081.46
Median (P_{50})	278.41	215.31	854.08	1,400.99
Third quartile (P_{75})	335.15	376.33	1,055.06	1,697.70
P_{90} value	373.75	549.83	1,232.63	1,892.55
Maximum (P_{100})	420.45	976.97	1,471.73	2,143.49
Mean	270.83	253.87	846.21	1,370.91
Standard deviation	79.82	206.84	287.87	404.70

[a] The number of data is equal to the number of Monte Carlo simulations.

5.6d) because the SMSS has a larger total pore volume (i.e., gross formation volume x (total) porosity) as mentioned in Tables 3.1 and 5.1. The mean theoretical fluid-phase CO_2 storage capacities of the SMSS and FCSS are equal to 2,511.60 Mton and 1,370.91 Mton, respectively.

The probability density distributions of the effective individual gas-, liquid-, supercritical-, and whole fluid-phase CO_2 storage capacities, which are calculated using Eq. (2.2) (Section 2.2), of the two clastic saline formations SMSS and FCSS in the Pohang Basin are plotted in Figures 5.7 and 5.8, respectively, and summarized in Tables 5.8 and 5.9, respectively. They are then compared with those of the theoretical individual gas-, liquid-, supercritical-, and whole fluid-phase CO_2 storage capacities (Figures 5.5 and 5.6 and Tables 5.6 and 5.7). In overall, they all show log-normal distributions, and their values are much lower than the values of the theoretical individual gas-, liquid-, supercritical-, and whole fluid-phase CO_2 storage capacities. This arises because the fluid-phase CO_2 storage efficiency factor shows a log-normal distribution and is much less than unity as shown in Figure 5.4c and Table 5.5.

As shown in Figures 5.7a, 5.7b, and 5.7c and the first, second, and third columns of Table 5.8, in the overlying saline formation SMSS, the effective liquid-phase (Figure 5.7b), supercritical-phase (Figure 5.7c), and gas-phase

(Figure 5.7a) CO_2 storage capacities are probabilistically higher, intermediate, and lower with the mean values of 39.34 Mton, 14.50 Mton, and 10.35 Mton, respectively. This also arises because of the above-mentioned same reasons, in the overlying saline formation SMSS, that the volumes occupied by the liquid- and gas-phase CO_2, respectively, are very similar to each other and greater than the volume occupied by the supercritical-phase CO_2, while the liquid- and supercritical-phase CO_2 densities are very close to each other and much greater than the gas-phase CO_2 density in the SMSS as mentioned in Table 5.4.

However, as shown in Figures 5.8a, 5.8b, and 5.8c and the first, second, and third columns of Table 5.9, in the underlying saline formation FCSS, the effective supercritical-phase (Figure 5.8c), gas-phase (Figure 5.8a), and liquid-phase (Figure 5.8b) CO_2 storage capacities are probabilistically higher, intermediate, and lower with the mean values of 21.93 Mton, 7.00 Mton, and 6.39 Mton, respectively. This also arises because of the above-mentioned same reasons, in the underlying saline formation FCSS, that the volumes occupied by the gas- and supercritical-phase CO_2, respectively, are somewhat similar to each other and greater than the volume occupied by the liquid-phase CO_2, while the liquid- and supercritical-phase CO_2 densities are very close to each other and much greater than the gas-phase CO_2 density in the FCSS as

(a) Effective gas-phase CO_2 storage capacity

(b) Effective liquid-phase CO_2 storage capacity

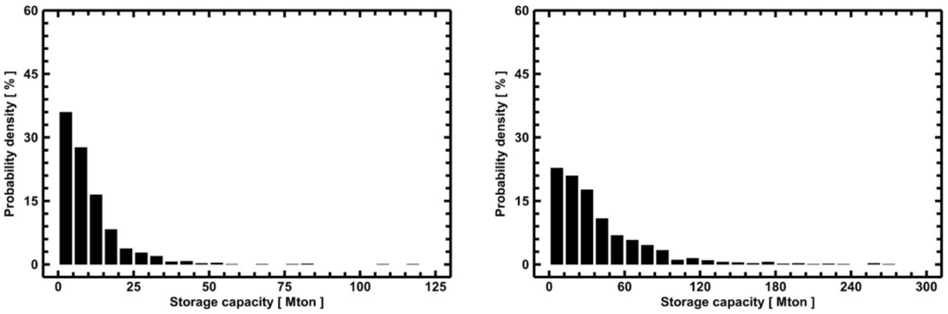

(c) Effective supercritical-phase CO_2 storage capacity

(d) Effective fluid-phase CO_2 storage capacity

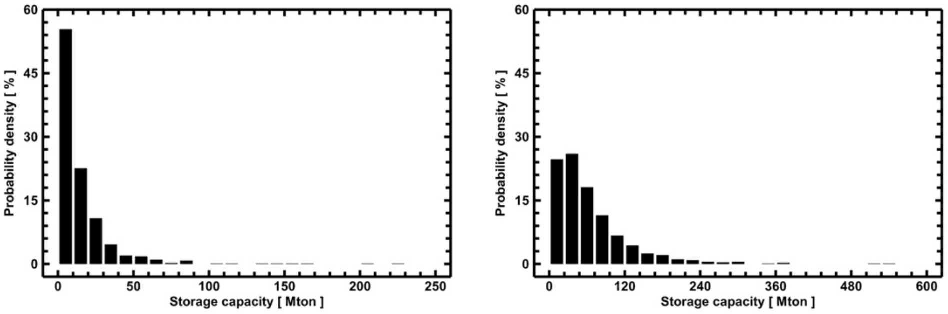

Figure 5.7. Probability density distributions of effective (a) gas-phase, (b) liquid-phase, (c) supercritical-phase, and (d) fluid-phase CO_2 storage capacities of the clastic saline formation SMSS in the Pohang Basin.

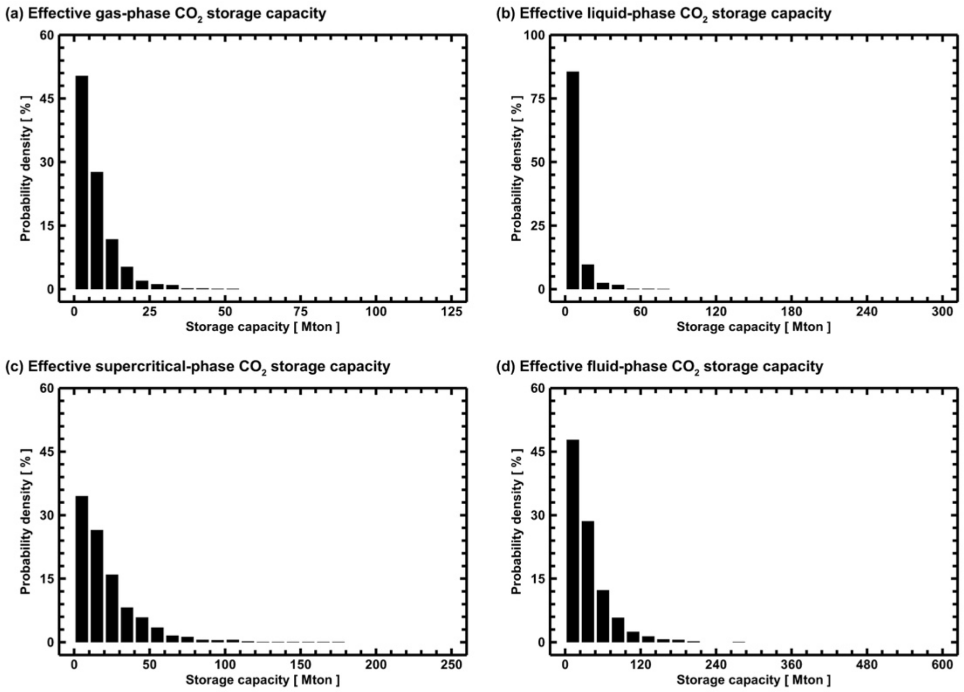

Figure 5.8. Probability density distributions of effective (a) gas-phase, (b) liquid-phase, (c) supercritical-phase, and (d) fluid-phase CO_2 storage capacities of the clastic saline formation FCSS in the Pohang Basin.

Table 5.8. Monte Carlo simulation output values of effective gas-, liquid-, supercritical-, and fluid-phase CO_2 storage capacities of the clastic saline formation SMSS in the Pohang Basin.

Parameter	SMSS (Mton)			
	Gas phase	Liquid phase	Supercritical phase	Fluid phase
Number of data[a]	1,000	1,000	1,000	1,000
Minimum ($P_{0.1}$)	0.18	0.52	0.04	1.18
P_{10} value	2.05	6.77	1.70	13.83
First quartile (P_{25})	3.75	12.91	3.87	24.08
Median (P_{50})	7.21	28.17	8.47	47.07
Third quartile (P_{75})	13.14	53.02	17.65	84.65
P_{90} value	21.51	84.61	31.62	131.26
Maximum (P_{100})	116.39	266.54	225.91	528.18
Mean	10.35	39.34	14.50	64.19
Standard deviation	10.87	38.67	19.59	60.05

[a] The number of data is equal to the number of Monte Carlo simulations.

Table 5.9. Monte Carlo simulation output values of effective gas-, liquid-, supercritical-, and fluid-phase CO_2 storage capacities of the clastic saline formation FCSS in the Pohang Basin.

Parameter	FCSS (Mton)			
	Gas phase	Liquid phase	Supercritical phase	Fluid phase
Number of data[a]	1,000	1,000	1,000	1,000
Minimum ($P_{0.1}$)	0.09	0.01	0.25	0.48
P_{10} value	1.35	0.36	4.01	6.85
First quartile (P_{25})	2.49	1.09	7.55	12.51
Median (P_{50})	4.91	3.27	15.17	25.25
Third quartile (P_{75})	9.16	8.16	28.42	46.22
P_{90} value	15.04	15.41	47.25	74.61
Maximum (P_{100})	54.74	80.13	178.58	281.24
Mean	7.00	6.39	21.93	35.32
Standard deviation	6.67	8.77	21.72	33.30

[a] The number of data is equal to the number of Monte Carlo simulations.

mentioned in Table 5.4.

As a whole, as shown in Figures 5.7d and 5.8d and the fourth column of Tables 5.8 and 5.9, the effective fluid-phase CO_2 storage capacity is probabilistically higher in the overlying saline formation SMSS (Figure 5.7d) compared with the underlying saline formation FCSS (Figure 5.8d) because the SMSS has a larger total pore volume (i.e., gross formation volume x (total) porosity) as mentioned in Tables 3.1 and 5.1. The mean effective fluid-phase CO_2 storage capacities of the SMSS and FCSS are equal to 64.19 Mton and 35.32 Mton, respectively.

5.4. Comparison with the results of the US DOE methodology

As shown in Table 1.1, in this study, three-dimensional geologic modeling as the linked methodology, probabilistic total porosity and geothermal gradient, and the resultant grid-based CO_2 density are adopted to estimate theoretical and effective individual gas-, liquid-, supercritical-, and whole fluid-phase CO_2 storage capacities. However, in the US DOE methodology, which is more well-established methodology compared with the other methodologies, the single bulk volume of geologic formation is used at simple multiplicative combination for the total pore volume which cannot reflect three-dimensionally irregular or complex shape of saline formation or sedimentary basin. Deterministic total porosity and geothermal gradient are applied and resultant deterministic CO_2 density are adopted to estimate fluid-phase CO_2 storage capacity. In order to identify and present the improvements and developments of fluid-phase CO_2 storage capacity estimation using the linked methodology than the US DOE methodology, theoretical and effective fluid-phase CO_2 storage capacity estimation of two saline formations SMSS and FCSS in the Pohang Basin using the linked methodology and the US DOE methodology is compared.

In order to estimate theoretical and effective fluid-phase CO_2 storage capacity estimation of two saline formations SMSS and FCSS in the Pohang Basin using the US DOE methodology, simple multiplicative combination is performed using the single bulk volumes (Table 3.1) and minimum, median, and maximum total porosities (Table 5.3), geothermal gradient (Table 5.3), resultant fluid-phase CO_2 densities, and fluid-phase CO_2 storage efficiency factor (Table 5.5) of two saline formations SMSS and FCSS. The total pore volumes of two saline formations SMSS and FCSS are obtained by the single bulk volumes and minimum, median, and maximum total porosities of two saline formations SMSS and FCSS. The CO_2 densities of two saline formations SMSS and FCSS are calculated using the minimum, median, and maximum geothermal gradient of two saline formations SMSS and FCSS.

Theoretical fluid-phase CO_2 storage capacities of two saline formations SMSS and FCSS are then estimated using the minimum, median, and maximum total pore volumes and fluid-phase CO_2 densities of two saline formations SMSS and FCSS. Finally, effective fluid-phase CO_2 storage capacities of two saline formations SMSS and FCSS are estimated using the minimum, median, and maximum theoretical fluid-phase CO_2 storage capacities of two saline formations SMSS and FCSS and fluid-phase CO_2 storage efficiency factor.

The minimum, median, and maximum theoretical fluid-phase CO_2 storage capacities of the two clastic saline formations SMSS and FCSS in the Pohang Basin using the linked methodology and US DOE methodology are summarized in Table 5.10.

As shown in the first and third column of Table 5.10, in the overlying saline formation SMSS, the minimum, median, and maximum values of theoretical fluid-phase CO_2 storage capacities using the linked methodology are 938.18 Mton, 2,545.89 Mton, and 3,952.83 Mton, respectively, while the minimum, median, and maximum values of theoretical fluid-phase CO_2 storage capacities using the US DOE methodology are 885.05 Mton, 2,575.54 Mton, and 4,004.72 Mton, respectively. The median theoretical fluid-phase CO_2 storage capacities using the linked methodology and US DOE

Table 5.10. Comparison of theoretical fluid-phase CO_2 storage capacities of the clastic saline formations SMSS and FCSS in the Pohang Basin.

Parameter	Linked methodology (Mton)		US DOE methodology (Mton)	
	SMSS	FCSS	SMSS	FCSS
Minimum ($P_{0.1}$)	938.18	410.41	885.02	373.57
Median (P_{50})	2,545.89	1,400.99	2,575.54	1,409.60
Maximum (P_{100})	3,952.83	2,143.49	4,004.72	2,215.46

methodology are very similar. On the other hand, the minimum and maximum theoretical fluid-phase CO_2 storage capacities using the US DOE methodology are lower and higher than the minimum and maximum theoretical fluid-phase CO_2 storage capacities using the linked methodology.

As shown in the second and fourth column of Table 5.10, in the underlying saline formation FCSS, the minimum, median, and maximum values of theoretical fluid-phase CO_2 storage capacities using the linked methodology are 410.41 Mton, 1,400.99 Mton, and 2,143.49 Mton, respectively, while the minimum, median, and maximum values of theoretical fluid-phase CO_2 storage capacities using the US DOE methodology are 373.57 Mton, 1,409.60 Mton, and 2,215.46 Mton, respectively. The median theoretical fluid-phase CO_2 storage capacities using the linked methodology and US DOE methodology are very similar. On the other hand, the minimum and maximum theoretical fluid-phase CO_2 storage capacities using the US DOE methodology are lower and higher than the minimum and maximum theoretical fluid-phase CO_2 storage capacities using the linked methodology.

As a whole, the linked methodology evaluate the theoretical fluid-phase CO_2 storage capacity in a narrower range than the US DOE methodology. The theoretical fluid-phase CO_2 storage capacities of two saline formations SMSS and FCSS in the Pohang Basin using the US DOE methodology are underestimated up to 5.7% and 9.0%, respectively, and overestimated up to 1.3% and 3.2%, respectively, compared with theoretical fluid-phase CO_2 storage capacities of two saline formations SMSS and FCSS in the Pohang Basin using the linked methodology. The underestimate and overestimate rates of the US DOE methodology are higher at the underlying saline formation FCSS. This arises because, the probabilistic total porosity in the underlying saline formation FCSS has higher variation or dispersion than the probabilistic total porosity in the overlying saline formation SMSS.

The minimum, median, and maximum effective fluid-phase CO_2 storage capacities of the two clastic saline formations SMSS and FCSS in the Pohang Basin using the linked methodology and US DOE methodology are summarized in Table 5.11.

As shown in the first and third column of Table 5.11, in the overlying saline formation SMSS, the minimum, median, and maximum values of effective fluid-phase CO_2 storage capacities using the linked methodology are 1.18 Mton, 47.07 Mton, and 528.18 Mton, respectively, while the minimum, median, and maximum values of effective fluid-phase CO_2 storage capacities using the US DOE methodology are 0.35 Mton, 51.51 Mton, and 752.09 Mton, respectively. The median effective fluid-phase CO_2 storage capacities using the linked methodology and US DOE methodology are very similar. On the

Table 5.11. Comparison of effective fluid-phase CO_2 storage capacities of the clastic saline formations SMSS and FCSS in the Pohang Basin.

Parameter	Linked methodology (Mton)		US DOE methodology (Mton)	
	SMSS	FCSS	SMSS	FCSS
Minimum ($P_{0.1}$)	1.18	0.48	0.35	0.15
Median (P_{50})	47.07	25.25	51.51	28.19
Maximum (P_{100})	528.18	281.24	752.09	416.06

other hand, the minimum and maximum effective fluid-phase CO_2 storage capacities using the US DOE methodology are lower and higher than the minimum and maximum effective fluid-phase CO_2 storage capacities using the linked methodology.

As shown in the second and fourth column of Table 5.11, in the underlying saline formation FCSS, the minimum, median, and maximum values of effective fluid-phase CO_2 storage capacities using the linked methodology are 0.48 Mton, 25.25 Mton, and 178.58 Mton, respectively, while the minimum, median, and maximum values of effective fluid-phase CO_2 storage capacities using the US DOE methodology are 0.15 Mton, 28.19 Mton, and 416.06 Mton, respectively. The median effective fluid-phase CO_2 storage capacities using the linked methodology and US DOE methodology are very similar. On the other hand, the minimum and maximum effective fluid-phase CO_2 storage capacities using the US DOE methodology are lower and higher than the minimum and maximum effective fluid-phase CO_2 storage capacities using the linked methodology.

As a whole, the linked methodology evaluate the effective fluid-phase CO_2 storage capacity in a narrower range than the US DOE methodology. The effective fluid-phase CO_2 storage capacities of two saline formations SMSS and FCSS in the Pohang Basin using the US DOE methodology are underestimated up to 70.3% and 68.7%, respectively, and overestimated up to 29.8% and 32.4%, respectively, compared with effective fluid-phase CO_2 storage capacities of two saline formations SMSS and FCSS in the Pohang Basin using the linked methodology. The underestimate and overestimate rates of the US DOE methodology are similar or higher at the underlying saline formation FCSS. This arises because, the probabilistic total porosity in the underlying saline formation FCSS has higher variation or dispersion than the probabilistic total porosity in the overlying saline formation SMSS. In addition, the underestimate and overestimate rates of the effective fluid-phase CO_2 storage capacity are higher than the theoretical fluid-phase CO_2 storage capacity. This arises because, the fluid-phase CO_2 storage efficiency factor, which has especially high variation or dispersion, is applied to evaluate the effective fluid-phase CO_2 storage capacity.

6. Three-dimensional carbon dioxide storage capacities

6.1. Spatial distributions of fluid-phase carbon dioxide storage capacities

The three-dimensional grid-wise (elemental) spatial distributions of the theoretical fluid-phase CO_2 storage capacities from the minimum to maximum of the overlying saline formation SMSS in the Pohang Basin are illustrated in Figure 6.1. And the three-dimensional grid-wise (elemental) spatial distributions of the CO_2 fluid phase types corresponding with theoretical fluid-phase CO_2 storage capacities from the minimum to maximum of the overlying saline formation SMSS in the Pohang Basin are illustrated in Figure 6.2.

As shown in Figure 6.1, in the overlying saline formation SMSS, the grid-wise theoretical fluid-phase CO_2 storage capacities are probabilistically higher at Area 1 (northeastern offshore area), intermediate at Area 2 (southern offshore area near the Yeongil Bay), and lower at Area 3 (western onshore area near the Pohang City). At the three areas, the SMSS is deep and thick as shown in Figures 4.3 and 4.5. In addition, as shown in Figure 6.2, in the overlying saline formation SMSS, CO_2 mainly exists as supercritical and

(a) Minimum theoretical fluid-phase CO_2 storage capacity

(b) First quartile theoretical fluid-phase CO_2 storage capacity

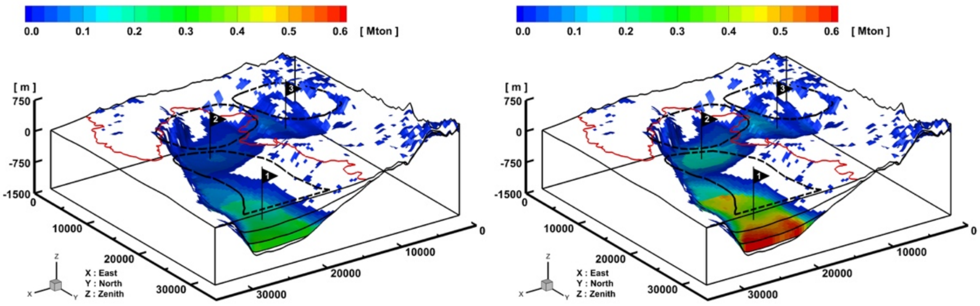

(c) Median theoretical fluid-phase CO_2 storage capacity

(d) Third quartile theoretical fluid-phase CO_2 storage capacity

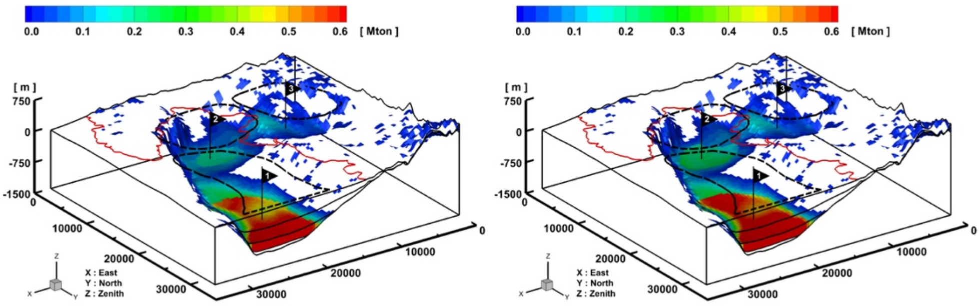

(e) Maximum theoretical fluid-phase CO_2 storage capacity

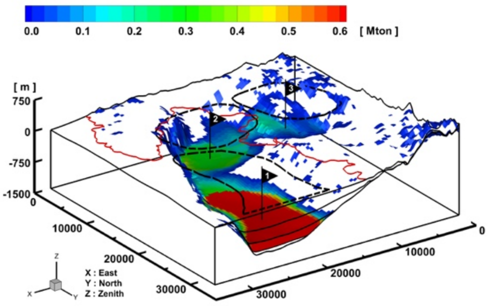

Figure 6.1. Three-dimensional grid-wise spatial distributions of (a) minimum, (b) first quartile, (c) median, (d) third quartile, and (e) maximum theoretical fluid-phase CO_2 storage capacities of the clastic saline formation SMSS in the Pohang Basin.

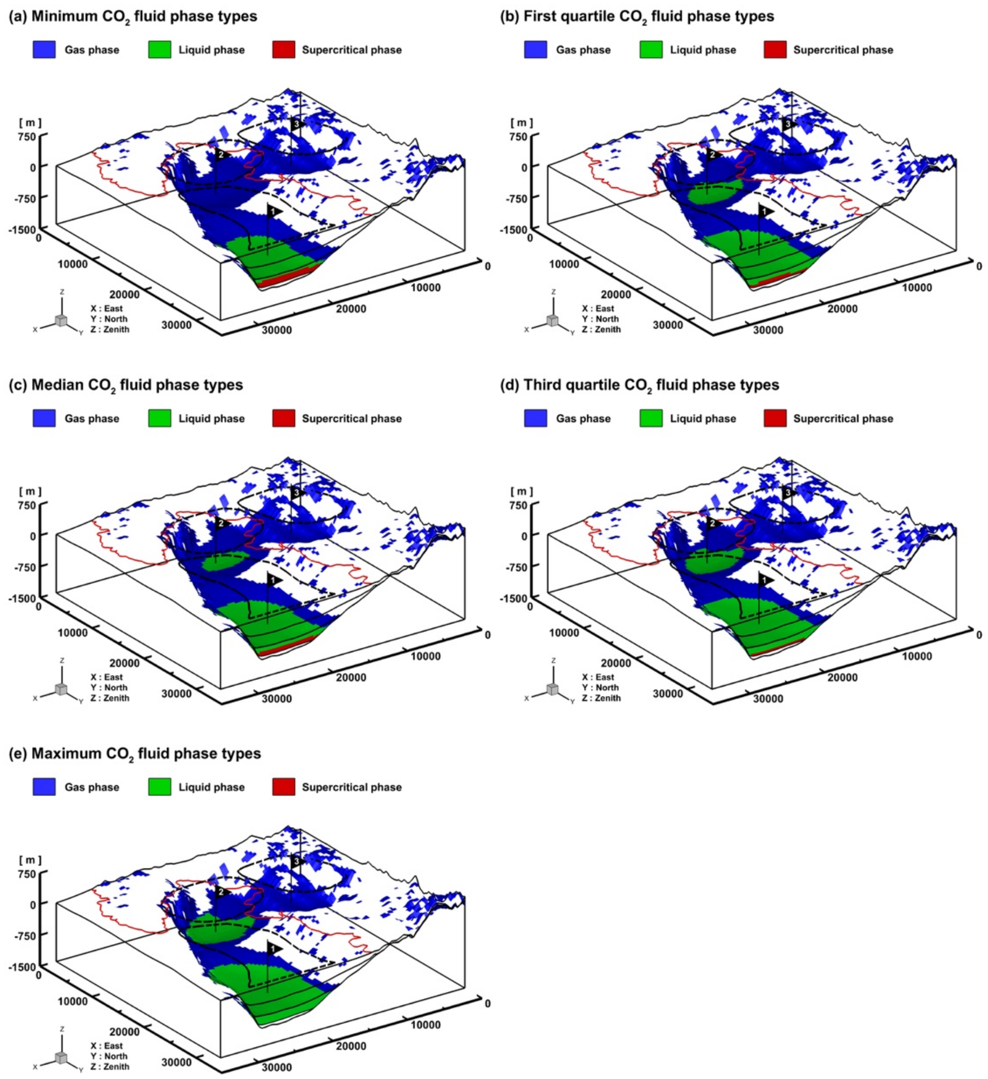

Figure 6.2. Three-dimensional grid-wise spatial distributions of CO_2 fluid phase types corresponding with (a) minimum, (b) first quartile, (c) median, (d) third quartile, and (e) maximum theoretical fluid-phase CO_2 storage capacities of the clastic saline formation SMSS in the Pohang Basin.

liquid phases at Area 1, liquid and gas phases at Area 2, and gas phase at Area 3. However, the area of liquid-phase CO_2 at the CO_2 fluid phase types corresponding with first-quartile theoretical fluid-phase CO_2 storage capacities (Figure 6.2b) are more distributed than those with median theoretical fluid-phase CO_2 storage capacities (Figure 6.2c). This arises because the total pore volume is more dominant factor than the fluid-phase CO_2 density (i.e., CO_2 fluid phase type) for fluid-phase CO_2 storage capacities.

The three-dimensional grid-wise (elemental) spatial distributions of the theoretical fluid-phase CO_2 storage capacities from the minimum to maximum of the underlying saline formation FCSS in the Pohang Basin are illustrated in Figure 6.3. And the three-dimensional grid-wise (elemental) spatial distributions of the CO_2 fluid phase types corresponding with theoretical fluid-phase CO_2 storage capacities from the minimum to maximum of the underlying saline formation FCSS in the Pohang Basin are illustrated in Figure 6.4.

As shown in Figure 6.3, in the underlying saline formation FCSS, the grid-wise theoretical fluid-phase CO_2 storage capacities are probabilistically higher at Area 2 (southern offshore area near the Yeongil Bay), intermediate at Area 1 (northeastern offshore area), and lower at Area 3 (western onshore area near the Pohang City). At the three areas, the FCSS is also deep and

(a) Minimum theoretical fluid-phase CO_2 storage capacity

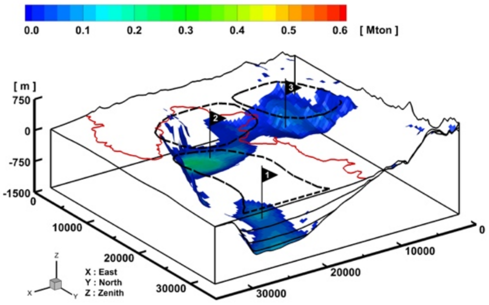

(b) First quartile theoretical fluid-phase CO_2 storage capacity

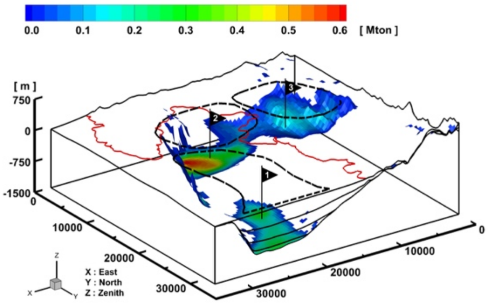

(c) Median theoretical fluid-phase CO_2 storage capacity

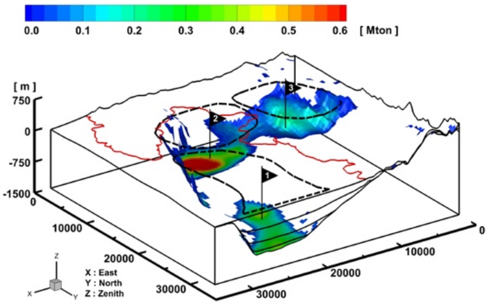

(d) Third quartile theoretical fluid-phase CO_2 storage capacity

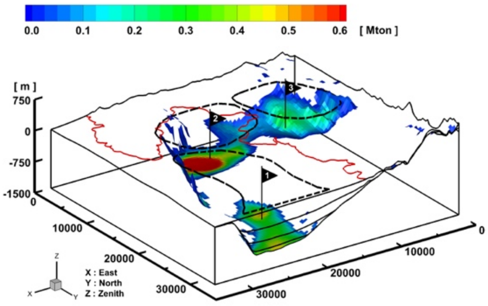

(e) Maximum theoretical fluid-phase CO_2 storage capacity

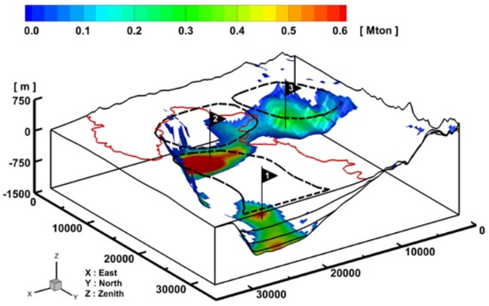

Figure 6.3. Three-dimensional grid-wise spatial distributions of (a) minimum, (b) first quartile, (c) median, (d) third quartile, and (e) maximum theoretical fluid-phase CO_2 storage capacities of the clastic saline formation FCSS in the Pohang Basin.

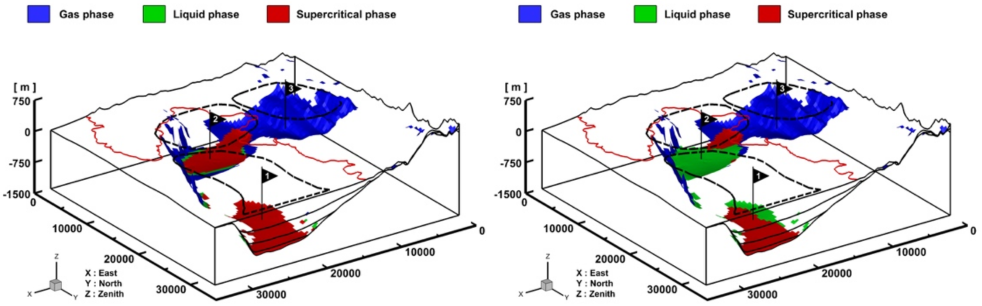

(a) Minimum CO_2 fluid phase types

(b) First quartile CO_2 fluid phase types

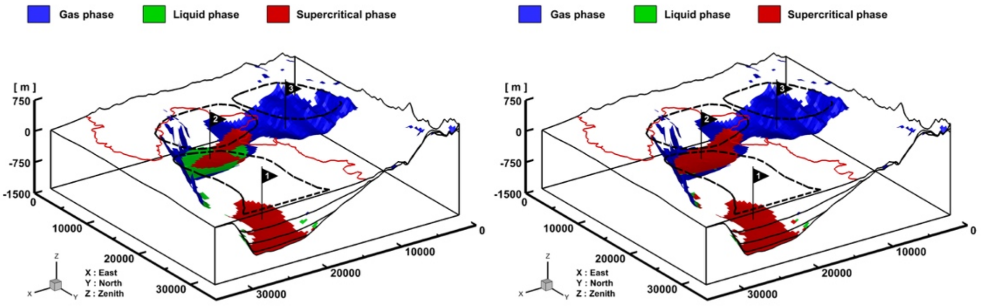

(c) Median CO_2 fluid phase types

(d) Third quartile CO_2 fluid phase types

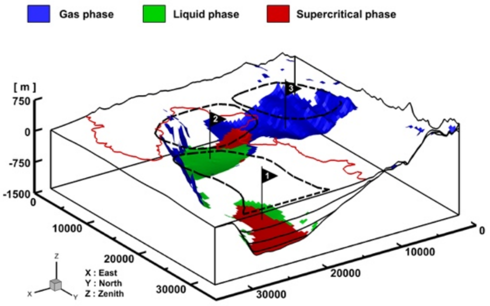

(e) Maximum CO_2 fluid phase types

Figure 6.4. Three-dimensional grid-wise spatial distributions of CO_2 fluid phase types corresponding with (a) minimum, (b) first quartile, (c) median, (d) third quartile, and (e) maximum theoretical fluid-phase CO_2 storage capacities of the clastic saline formation FCSS in the Pohang Basin.

thick as shown in Figures 4.3 and 4.5. In addition, as shown in Figure 6.4, in the underlying saline formation FCSS, CO_2 mainly exists as supercritical phase at Area 1, supercritical and liquid phases at Area 2, and gas phase at Area 3. However, the area of supercritical-phase CO_2 at the CO_2 fluid phase types corresponding with minimum theoretical fluid-phase CO_2 storage capacities (Figure 6.4a) are more distributed than those with maximum theoretical fluid-phase CO_2 storage capacities (Figure 6.4e). This arises because the total pore volume is more dominant factor than the fluid-phase CO_2 density (i.e., CO_2 fluid phase type) for fluid-phase CO_2 storage capacities.

As a whole, as shown in Figures 6.1 and 6.3, the grid-wise theoretical fluid-phase CO_2 storage capacities are probabilistically higher in the overlying saline formation SMSS (Figure 6.1) compared with the underlying saline formation FCSS (Figure 6.3). In addition (as mentioned in Sections 5.2 and 5.3), as shown in Figures 6.2 and 6.4, at Areas 1 and 2, the liquid-phase CO_2 is more dominant than the supercritical-phase CO_2 in the overlying saline formation SMSS (Figure 6.2), whereas the supercritical-phase CO_2 is more dominant than the liquid-phase CO_2 in the underlying saline formation FCSS (Figure 6.4).

The three-dimensional grid-wise (elemental) spatial distributions of the effective fluid-phase CO_2 storage capacities from the minimum to maximum of the overlying saline formation SMSS in the Pohang Basin are illustrated in Figure 6.5. They are then compared with those of the theoretical fluid-phase CO_2 storage capacities (Figure 6.1). And the three-dimensional grid-wise (elemental) spatial distributions of the CO_2 fluid phase types corresponding with theoretical fluid-phase CO_2 storage capacities from the minimum to maximum of the overlying saline formation SMSS in the Pohang Basin are illustrated in Figure 6.6.

As shown in Figure 6.5, in the overlying saline formation SMSS, the grid-wise effective fluid-phase CO_2 storage capacities are probabilistically higher at Area 1 (northeastern offshore area), intermediate at Area 2 (southern offshore area near the Yeongil Bay), and lower at Area 3 (western onshore area near the Pohang City). At the three areas, the SMSS is deep and thick as shown in Figures 4.3 and 4.5. In addition, as shown in Figure 6.6, in the overlying saline formation SMSS, CO_2 mainly exists as supercritical and liquid phases at Area 1, liquid and gas phases at Area 2, and gas phase at Area 3. However, the area of liquid-phase CO_2 at the CO_2 fluid phase types corresponding with minimum effective fluid-phase CO_2 storage capacities (Figure 6.6a) are more distributed than those with maximum effective fluid-phase CO_2 storage capacities (Figure 6.6e). This arises because the total pore volume is more dominant factor than the fluid-phase CO_2 density (i.e., CO_2

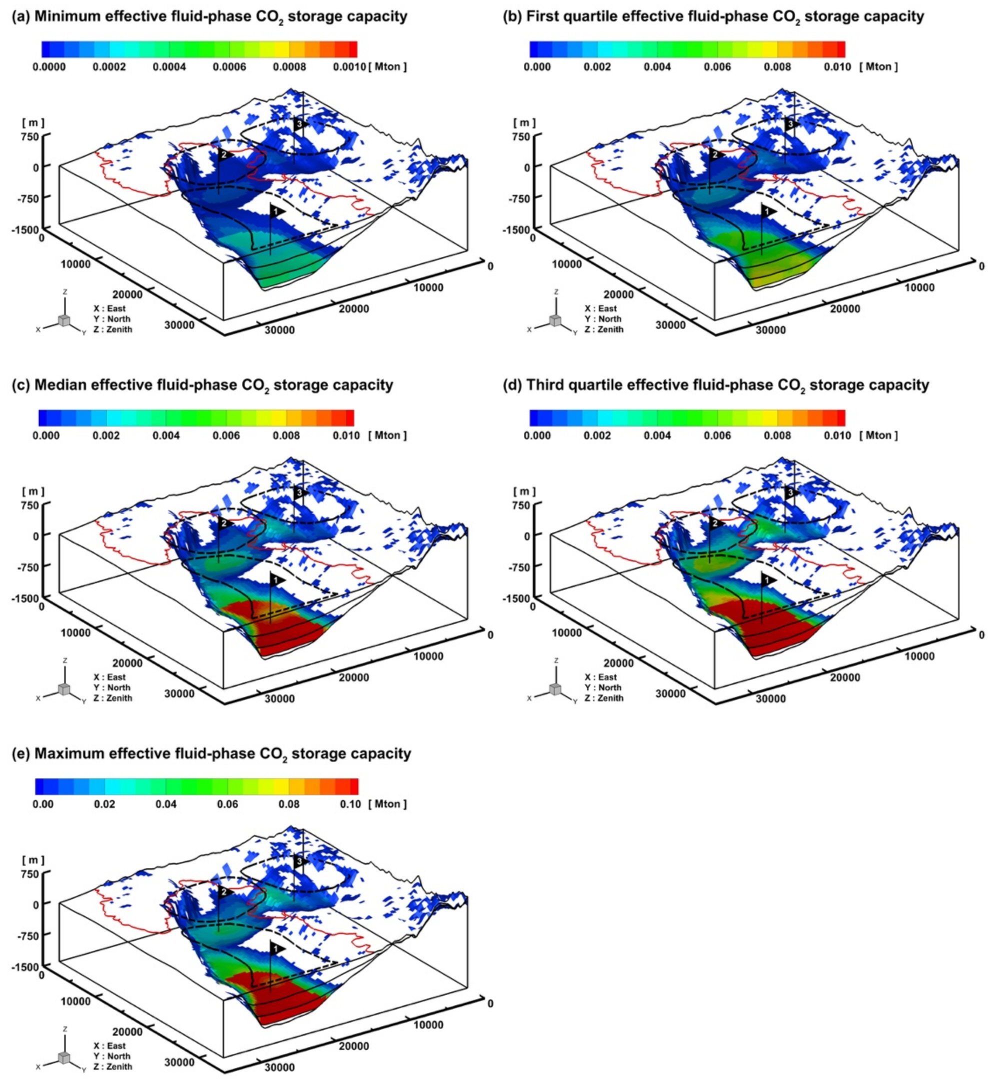

Figure 6.5. Three-dimensional grid-wise spatial distributions of (a) minimum, (b) first quartile, (c) median, (d) third quartile, and (e) maximum effective fluid-phase CO_2 storage capacities of the clastic saline formation SMSS in the Pohang Basin.

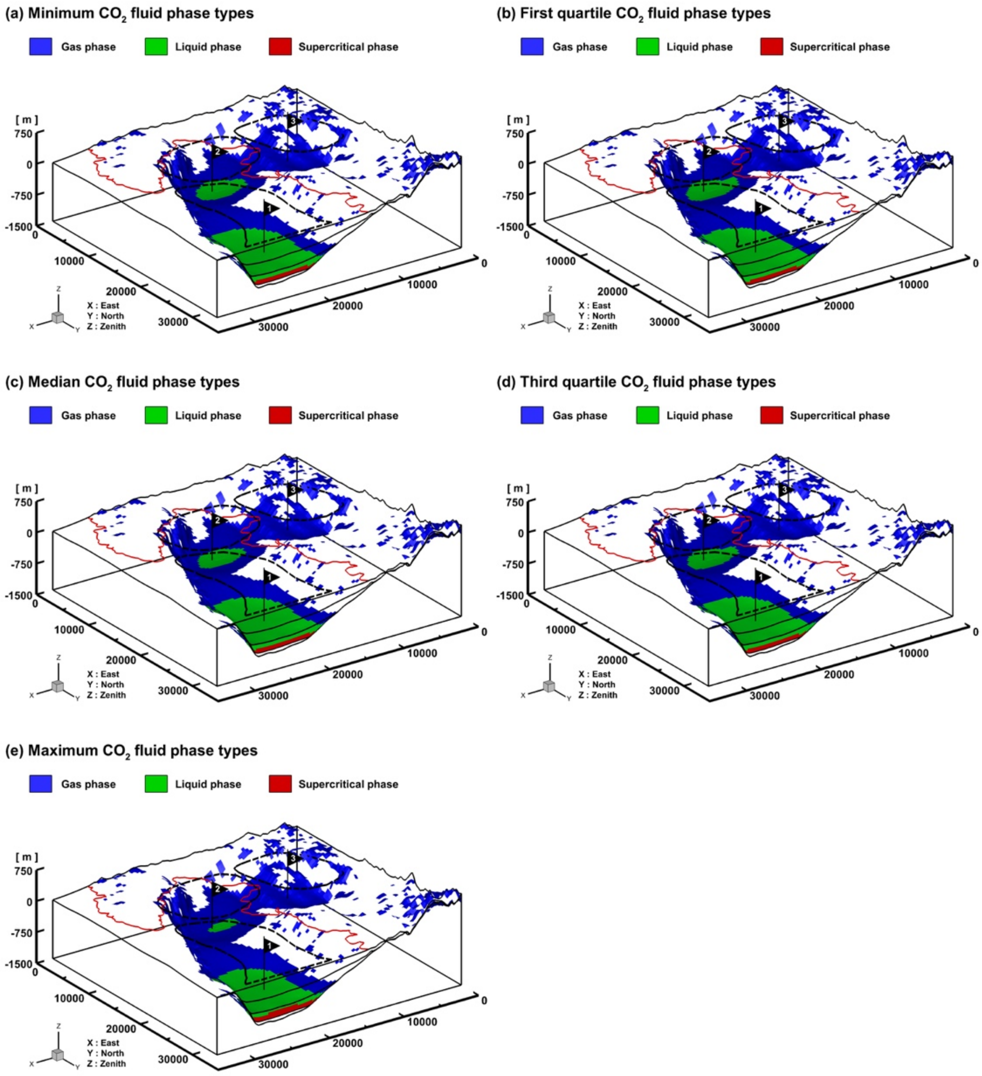

Figure 6.6. Three-dimensional grid-wise spatial distributions of CO_2 fluid phase types corresponding with (a) minimum, (b) first quartile, (c) median, (d) third quartile, and (e) maximum effective fluid-phase CO_2 storage capacities of the clastic saline formation SMSS in the Pohang Basin.

fluid phase type) for fluid-phase CO_2 storage capacities.

The three-dimensional grid-wise (elemental) spatial distributions of the effective fluid-phase CO_2 storage capacities from the minimum to maximum of the underlying saline formation FCSS in the Pohang Basin are illustrated in Figure 6.7. They are then compared with those of the theoretical fluid-phase CO_2 storage capacities (Figure 6.3). And the three-dimensional grid-wise (elemental) spatial distributions of the CO_2 fluid phase types corresponding with theoretical fluid-phase CO_2 storage capacities from the minimum to maximum of the underlying saline formation FCSS in the Pohang Basin are illustrated in Figure 6.8.

As shown in Figure 6.7, in the underlying saline formation FCSS, the grid-wise effective fluid-phase CO_2 storage capacities are probabilistically higher at Area 2 (southern offshore area near the Yeongil Bay), intermediate at Area 1 (northeastern offshore area), and lower at Area 3 (western onshore area near the Pohang City). At the three areas, the FCSS is also deep and thick as shown in Figures 4.3 and 4.5. In addition, as shown in Figure 6.8, in the underlying saline formation FCSS, CO_2 mainly exists as supercritical phase at Area 1, supercritical and liquid phases at Area 2, and gas phase at Area 3. However, the area of supercritical-phase CO_2 at the CO_2 fluid phase types corresponding with first quartile effective fluid-phase CO_2 storage capacities

(Figure 6.8b) are more distributed than those with maximum effective fluid-phase CO_2 storage capacities (Figure 6.8e). This arises because the total pore volume is more dominant factor than the fluid-phase CO_2 density (i.e., CO_2 fluid phase type) for fluid-phase CO_2 storage capacities.

As a whole, as shown in Figures 6.5 and 6.7, the grid-wise theoretical fluid-phase CO_2 storage capacities are probabilistically higher in the overlying saline formation SMSS (Figure 6.5) compared with the underlying saline formation FCSS (Figure 6.7). In addition (as mentioned in Sections 5.2 and 5.3), as shown in Figures 6.6 and 6.8, at Areas 1 and 2, the liquid-phase CO_2 is more dominant than the supercritical-phase CO_2 in the overlying saline formation SMSS (Figure 6.6), whereas the supercritical-phase CO_2 is more dominant than the liquid-phase CO_2 in the underlying saline formation FCSS (Figure 6.8).

In both saline formations, the grid-wise effective fluid-phase CO_2 storage capacities also show the almost identical spatial distributions to those of the above-mentioned grid-wise theoretical fluid-phase CO_2 storage capacities. However, their values are much lower than the values of the grid-wise median theoretical fluid-phase CO_2 storage capacities. This arises because the fluid-phase CO_2 storage efficiency factor is much less than unity as shown in Figure 5.4c and Table 5.5.

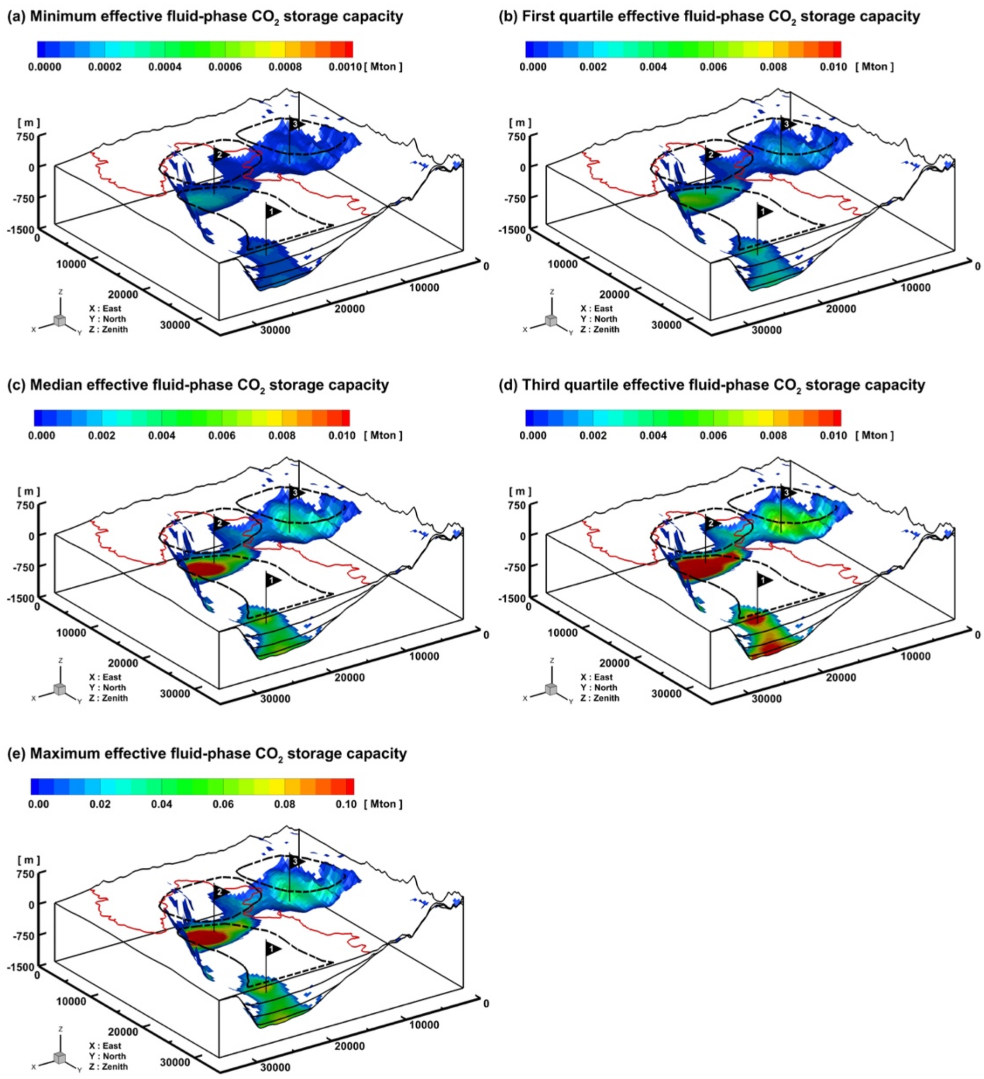

Figure 6.7. Three-dimensional grid-wise spatial distributions of (a) minimum, (b) first quartile, (c) median, (d) third quartile, and (e) maximum effective fluid-phase CO_2 storage capacities of the clastic saline formation FCSS in the Pohang Basin.

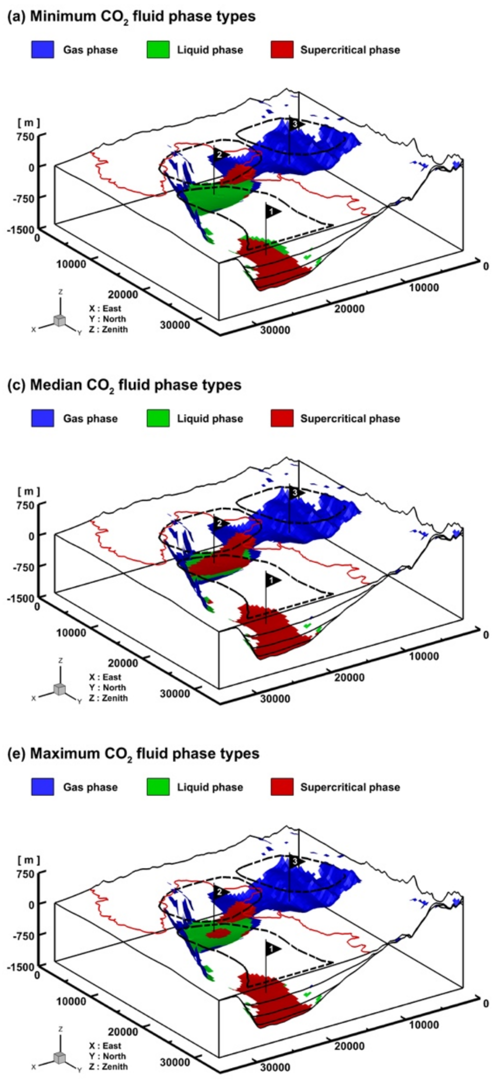

Figure 6.8. Three-dimensional grid-wise spatial distributions of CO_2 fluid phase types corresponding with (a) minimum, (b) first quartile, (c) median, (d) third quartile, and (e) maximum effective fluid-phase CO_2 storage capacities of the clastic saline formation FCSS in the Pohang Basin.

6.2. Optimal locations of carbon dioxide storage

Among the above-mentioned three prospective areas (i.e., Areas 1, 2, and 3) in the Pohang Basin, the optimal areas or locations of CO_2 injection and storage can be recommended as follows.

Four key criteria (parameters) for selecting or ranking the optimal CO_2 storage locations are decided first by summarizing and analyzing the results of the three-dimensional geologic modeling (Section 4) and grid-based Monte Carlo simulation (Section 5). They are the (1) formation volumes, (2) effective individual gas-, liquid-, supercritical-, and whole fluid-phase CO_2 storage capacities, and (3) effective individual gas-, liquid-, supercritical-, and whole fluid-phase CO_2 storage densities (intensities) of the clastic saline formations (i.e., SMSS and FCSS) in terms of CO_2 fluid masses and phases as well as the (4) existence (influence) of the major faults at the three prospective areas. The first three criteria are considered as positive factors because their higher values are more favorable for large-size commercial-scale CO_2 storage. On the other hand, in general, a fault can act hydrogeologically as a barrier or leakage pathway. However, the eight major faults in the Pohang Basin have not yet been well identified and characterized. Thus, the last criterion is considered as a negative factor in order to avoid or minimize the risk of possible CO_2 leakage through faults and thus to maximize integrity and safety of CO_2 storage. The grid-wise effective individual gas-, liquid-, supercritical-, and whole fluid-phase CO_2 storage capacities and storage densities (intensities) of the clastic saline formations (i.e., SMSS and FCSS) are only selected for key criteria (parameters) instead of both theoretical and effective individual gas-, liquid-, supercritical-, and whole fluid-phase CO_2 storage capacities and storage densities (intensities) of the clastic saline formations (i.e., SMSS and FCSS). This is because, in both saline formations, the grid-wise theoretical individual gas-, liquid-, supercritical-, and whole fluid-phase CO_2 storage capacities show the almost identical spatial distributions to those of the grid-wise effective individual gas-, liquid-, supercritical-, and whole fluid-phase CO_2 storage capacities as mentioned in Section 6.1 and as follows.

The values of the four key criteria (parameters) at the three prospective areas such as Areas 1, 2, and 3 of the overlying saline formation SMSS are then summarized in Table 6.1. The top views of the three-dimensional grid-wise spatial distributions of the theoretical and effective fluid-phase CO_2 storage capacities (i.e., second key parameter) of the overlying saline formation SMSS with the eight major faults (i.e., fourth key parameter) are also illustrated in Figures 6.9 and 6.11, respectively. And the top views of the three-dimensional grid-wise spatial distributions of the CO_2 fluid phase types corresponding with theoretical and effective individual gas-, liquid-, supercritical-, and whole fluid-phase CO_2 storage capacities (i.e., second key parameter) of the overlying saline formation SMSS with the eight major faults (i.e., fourth key parameter) are also illustrated in Figures 6.10 and 6.12, respectively.

On the basis of the formation volumes (i.e., first key parameter) and theoretical and effective individual gas-, liquid-, supercritical-, and whole fluid-phase CO_2 storage capacities (i.e., second key parameter), the optimal locations of CO_2 storage in the overlying saline formation SMSS are better in the order of Areas 1, 2, and 3 (Figures 6.9 and 6.11). Although the CO_2 fluid phase type is not a specific key parameter, in terms of the CO_2 fluid phase types, the optimal locations of CO_2 storage in the overlying saline formation SMSS are also generally better in the order of Areas 1, 2, and 3 (Figures 6.10 and 6.12). On the contrary, there are exceptional cases that the area of liquid-phase CO_2 at the CO_2 fluid phase types corresponding with first quartile theoretical fluid-phase CO_2 storage capacities (Figure 6.10b) are more distributed than those with median theoretical fluid-phase CO_2 storage capacities (Figure 6.10c) and the area of liquid-phase CO_2 at the CO_2 fluid phase types corresponding with minimum effective fluid-phase CO_2 storage capacities (Figure 6.12a) are more distributed than those with maximum

Table 6.1. Summary values of the four key criteria (parameters) at the three prospective areas of the clastic saline formation SMSS in the Pohang Basin.

Parameter	Area 1	Area 2	Area 3
Shallow Marine Sandstone (SMSS)			
Formation volume (km^3)[a] occupied by CO_2			
Gas phase	3.12	3.33	3.52
Liquid phase	9.27	1.78	0.00
Supercritical phase	4.15	0.21	0.05
Fluid phase	16.54	5.32	3.57
Effective CO_2 storage capacity (Mton)[a]			
Gas phase	2.63	2.87	2.00
Liquid phase	24.03	4.18	0.00
Supercritical phase	11.02	0.24	0.05
Fluid phase	37.68	7.29	2.05
Effective CO_2 storage density (Mton/km^3)[b]			
Gas phase	0.84	0.86	0.57
Liquid phase	2.59	2.35	-
Supercritical phase	2.66	1.14	1.00
Fluid phase	2.28	1.37	0.57
Existence of major faults			
Number of major faults	3	4	5
Degree of dissection	slight	high	high
Overall suitability rank for geologic CO_2 storage	first	second	third

[a] The values are equal to the median (P_{50}) values for each phase.

[b] The effective CO_2 storage density is equal to the effective CO_2 storage capacity per formation volume for each phase (Section 2.2).

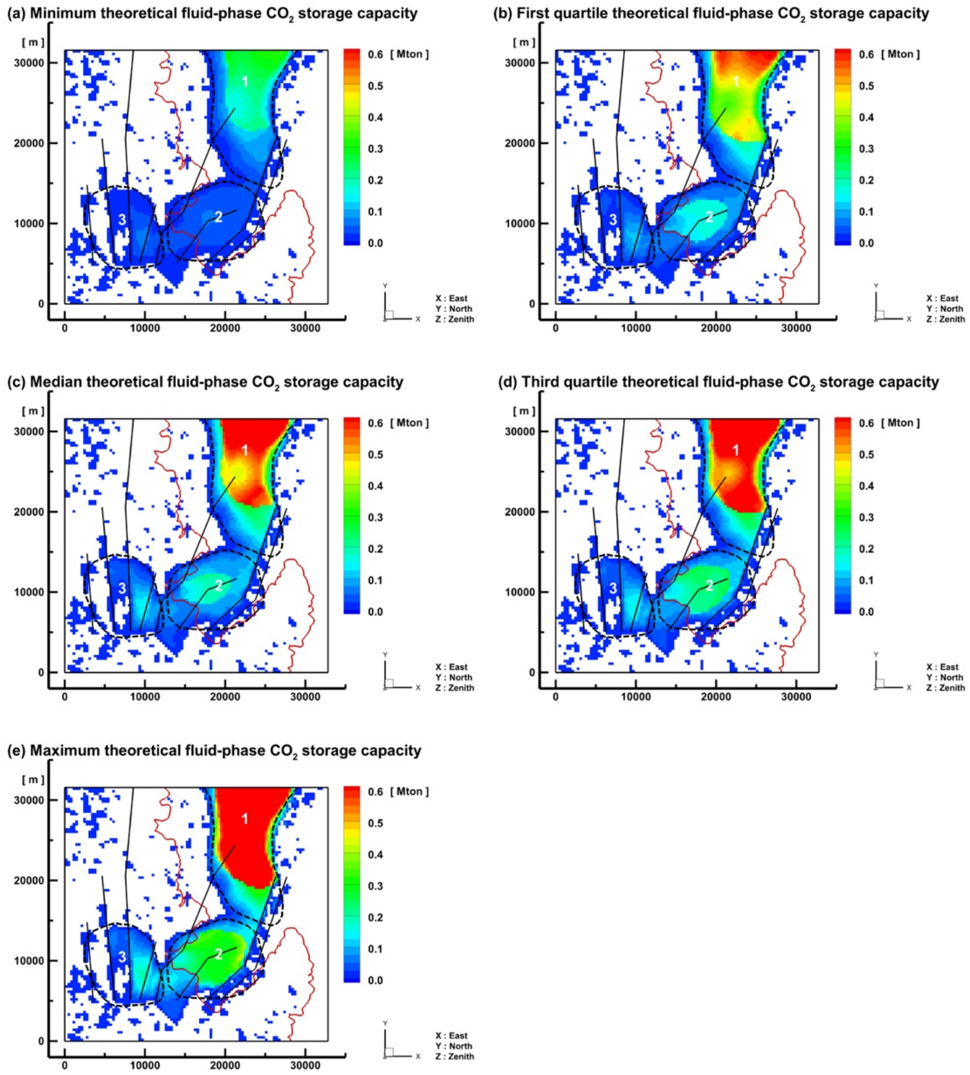

(a) Minimum theoretical fluid-phase CO$_2$ storage capacity

(b) First quartile theoretical fluid-phase CO$_2$ storage capacity

(c) Median theoretical fluid-phase CO$_2$ storage capacity

(d) Third quartile theoretical fluid-phase CO$_2$ storage capacity

(e) Maximum theoretical fluid-phase CO$_2$ storage capacity

Figure 6.9. Top views of three-dimensional grid-wise spatial distributions of (a) minimum, (b) first quartile, (c) median, (d) third quartile, and (e) maximum theoretical fluid-phase CO$_2$ storage capacities of the clastic saline formation SMSS in the Pohang Basin with the eight major faults (black solid lines).

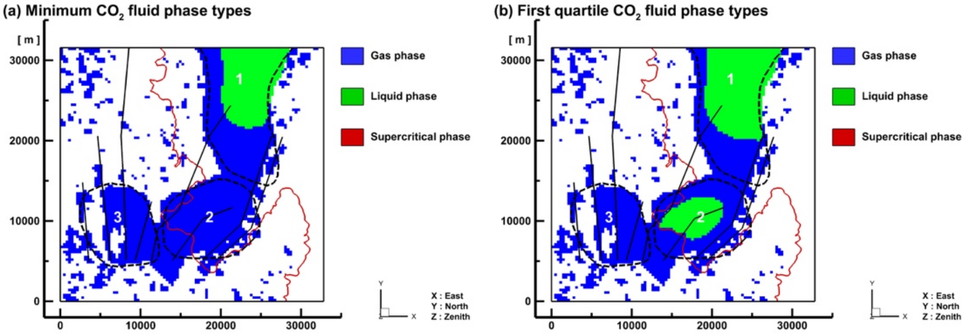

(a) Minimum CO_2 fluid phase types

(b) First quartile CO_2 fluid phase types

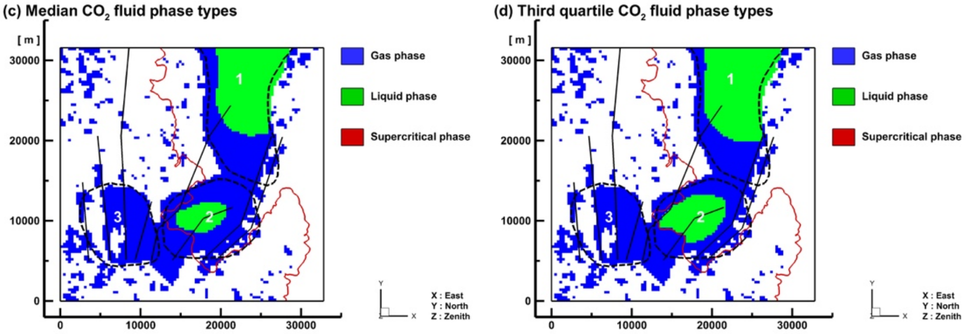

(c) Median CO_2 fluid phase types

(d) Third quartile CO_2 fluid phase types

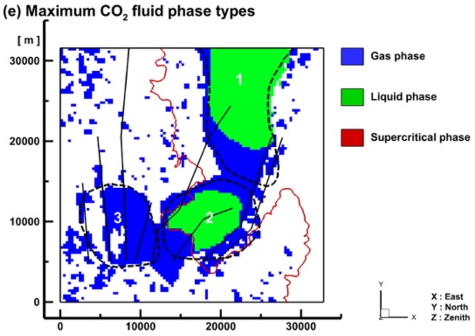

(e) Maximum CO_2 fluid phase types

Figure 6.10. Top views of three-dimensional grid-wise spatial distributions of CO_2 fluid phase types corresponding with (a) minimum, (b) first quartile, (c) median, (d) third quartile, and (e) maximum theoretical fluid-phase CO_2 storage capacities of the clastic saline formation SMSS in the Pohang Basin with the eight major faults (black solid lines).

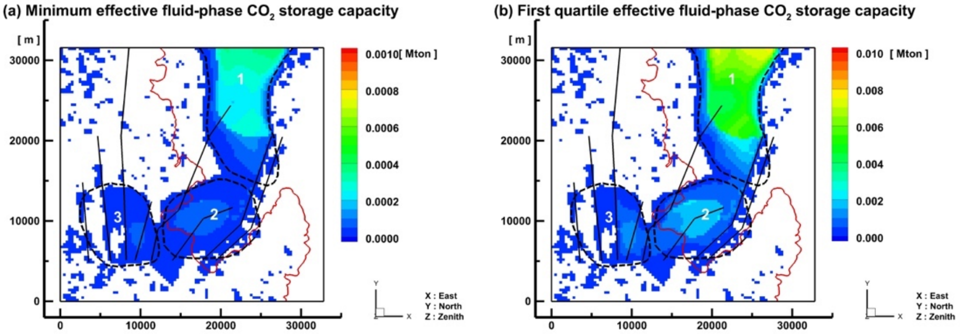
(a) Minimum effective fluid-phase CO_2 storage capacity

(b) First quartile effective fluid-phase CO_2 storage capacity

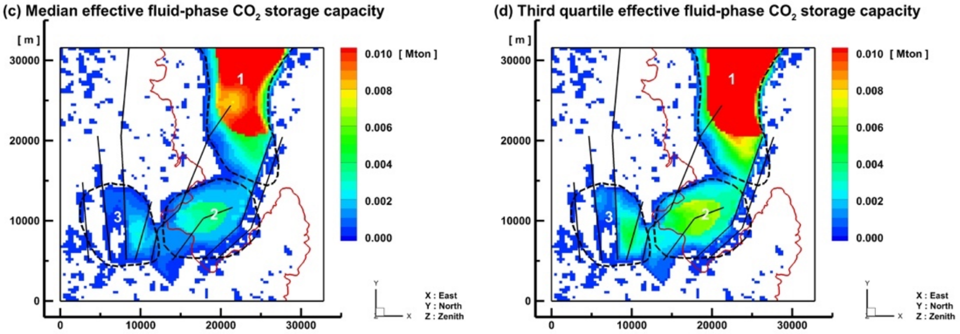
(c) Median effective fluid-phase CO_2 storage capacity

(d) Third quartile effective fluid-phase CO_2 storage capacity

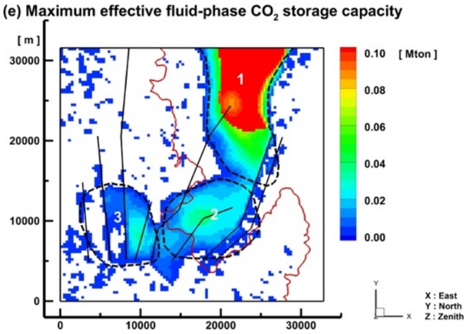
(e) Maximum effective fluid-phase CO_2 storage capacity

Figure 6.11. Top views of three-dimensional grid-wise spatial distributions of (a) minimum, (b) first quartile, (c) median, (d) third quartile, and (e) maximum effective fluid-phase CO_2 storage capacities of the clastic saline formation SMSS in the Pohang Basin with the eight major faults (black solid lines).

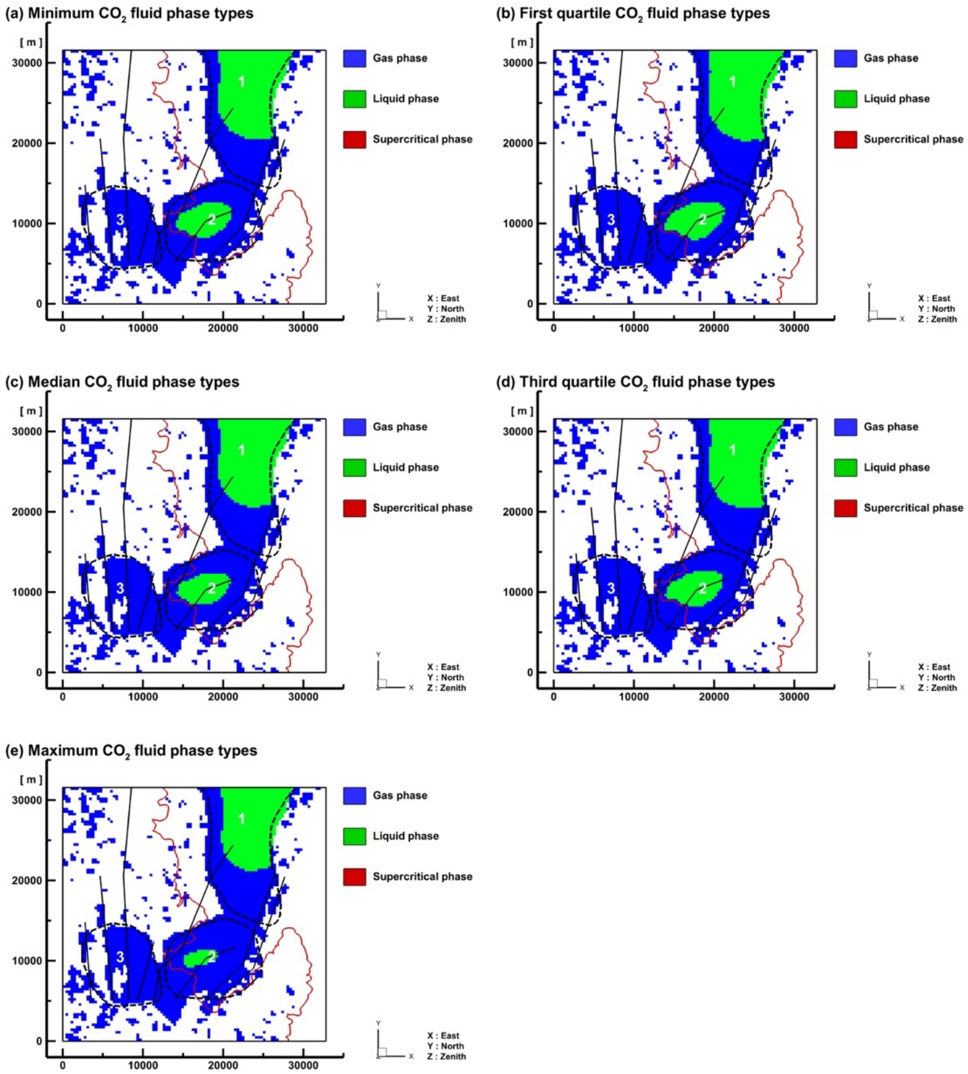

Figure 6.12. Top views of three-dimensional grid-wise spatial distributions of CO_2 fluid phase types corresponding with (a) minimum, (b) first quartile, (c) median, (d) third quartile, and (e) maximum effective fluid-phase CO_2 storage capacities of the clastic saline formation SMSS in the Pohang Basin with the eight major faults (black solid lines).

effective fluid-phase CO_2 storage capacities (Figure 6.12e). This arises because the total pore volume is more dominant factor than the fluid-phase CO_2 density (i.e., CO_2 fluid phase type) for fluid-phase CO_2 storage capacities as mention in Section 6.1. In addition, in terms of the effective individual gas-, liquid-, supercritical-, and whole fluid-phase CO_2 storage densities (i.e., third key parameter), the optimal locations of CO_2 storage in SMSS are consistently better in the order of Areas 1, 2, and 3 (Table 6.1).

The values of the four key criteria (parameters) at the three prospective areas such as Areas 1, 2, and 3 of the underlying saline formation FCSS are then summarized in Table 6.2. The top views of the three-dimensional grid-wise spatial distributions of the theoretical and effective individual gas-, liquid-, supercritical-, and whole fluid-phase CO_2 storage capacities (i.e., second key parameter) of the underlying saline formation FCSS with the eight major faults (i.e., fourth key parameter) are also illustrated in Figures 6.13 and 6.15, respectively. And the top views of the three-dimensional grid-wise spatial distributions of the CO_2 fluid phase types corresponding with theoretical and effective individual gas-, liquid-, supercritical-, and whole fluid-phase CO_2 storage capacities (i.e., second key parameter) of the underlying saline formation FCSS with the eight major faults (i.e., fourth key parameter) are also illustrated in Figures 6.14 and 6.16, respectively.

Table 6.2. Summary values of the four key criteria (parameters) at the three prospective areas of the clastic saline formation FCSS in the Pohang Basin.

Parameter	Area 1	Area 2	Area 3
Fluvial Conglomerate and Sandstone (FCSS)			
Formation volume (km^3)[a] occupied by CO_2			
Gas phase	0.11	3.51	4.95
Liquid phase	0.05	0.53	0.00
Supercritical phase	2.41	4.73	0.31
Fluid phase	2.57	8.77	5.26
Effective CO_2 storage capacity (Mton)[a]			
Gas phase	0.06	1.96	3.17
Liquid phase	0.14	1.21	0.00
Supercritical phase	6.64	11.68	0.37
Fluid phase	6.84	14.85	3.54
Effective CO_2 storage density (Mton/km^3)[b]			
Gas phase	0.55	0.56	0.64
Liquid phase	2.80	2.28	-
Supercritical phase	2.76	2.47	1.19
Fluid phase	2.66	1.69	0.67
Existence of major faults			
Number of major faults	3	4	5
Degree of dissection	slight	high	high
Overall suitability rank for geologic CO_2 storage	first	second	third

[a] The values are equal to the median (P_{50}) values for each phase.

[b] The effective CO_2 storage density is equal to the effective CO_2 storage capacity per formation volume for each phase (Section 2.2).

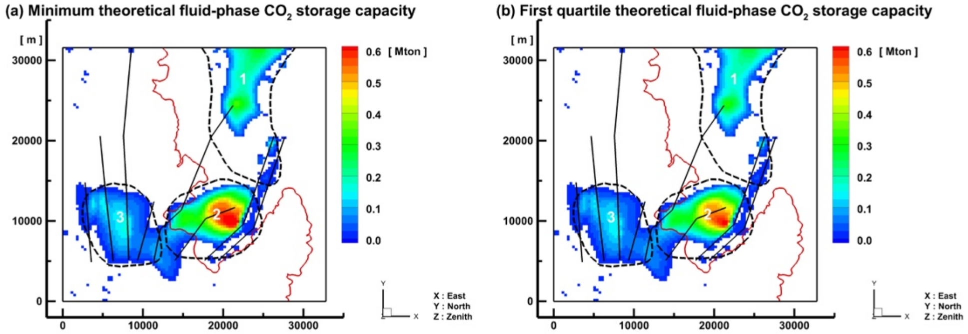

(a) Minimum theoretical fluid-phase CO_2 storage capacity

(b) First quartile theoretical fluid-phase CO_2 storage capacity

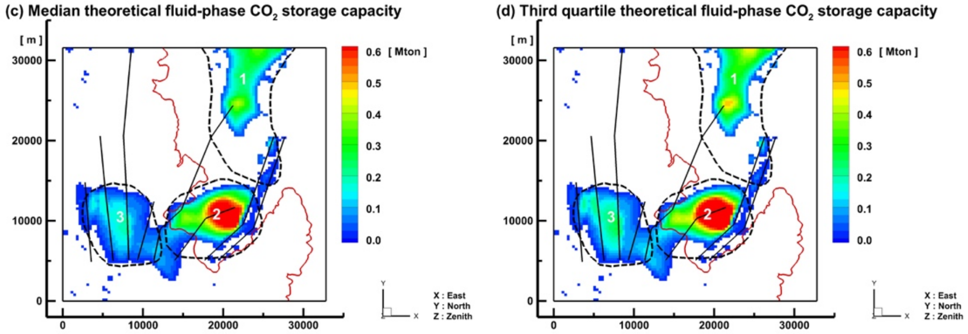

(c) Median theoretical fluid-phase CO_2 storage capacity

(d) Third quartile theoretical fluid-phase CO_2 storage capacity

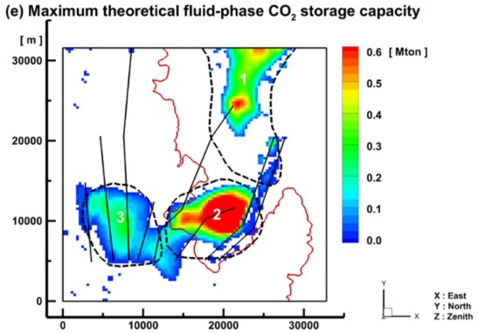

(e) Maximum theoretical fluid-phase CO_2 storage capacity

Figure 6.13. Top views of three-dimensional grid-wise spatial distributions of (a) minimum, (b) first quartile, (c) median, (d) third quartile, and (e) maximum theoretical fluid-phase CO_2 storage capacities of the clastic saline formation FCSS in the Pohang Basin with the eight major faults (black solid lines).

(a) Minimum CO$_2$ fluid phase types

(b) First quartile CO$_2$ fluid phase types

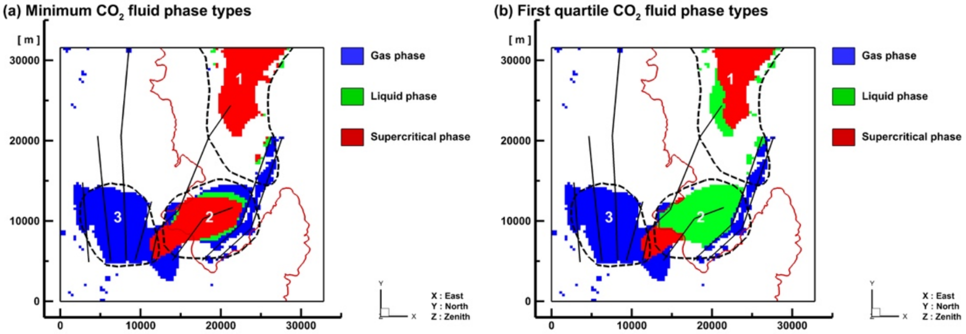

(c) Median CO$_2$ fluid phase types

(d) Third quartile CO$_2$ fluid phase types

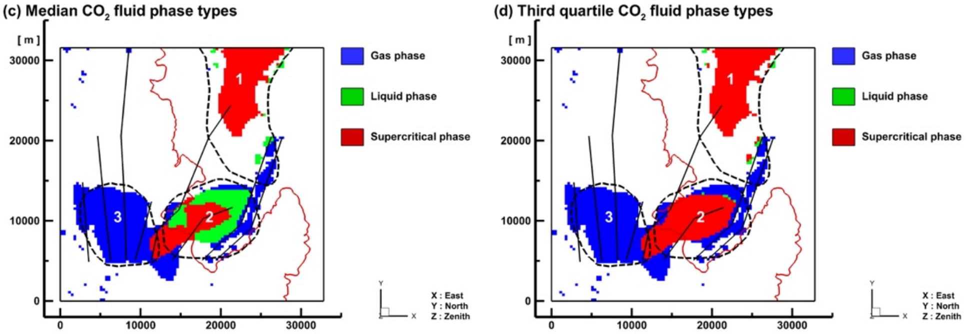

(e) Maximum CO$_2$ fluid phase types

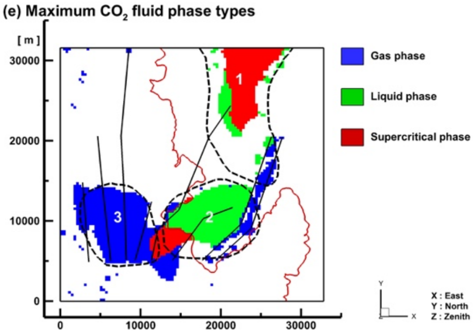

Figure 6.14. Top views of three-dimensional grid-wise spatial distributions of CO$_2$ fluid phase types corresponding with (a) minimum, (b) first quartile, (c) median, (d) third quartile, and (e) maximum theoretical fluid-phase CO$_2$ storage capacities of the clastic saline formation FCSS in the Pohang Basin with the eight major faults (black solid lines).

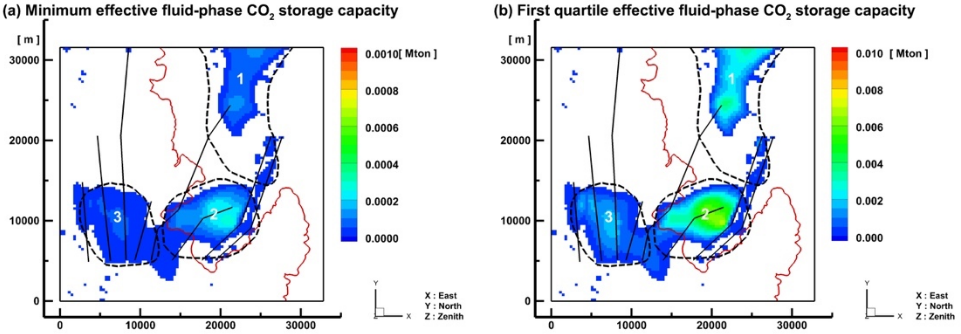

(a) Minimum effective fluid-phase CO_2 storage capacity

(b) First quartile effective fluid-phase CO_2 storage capacity

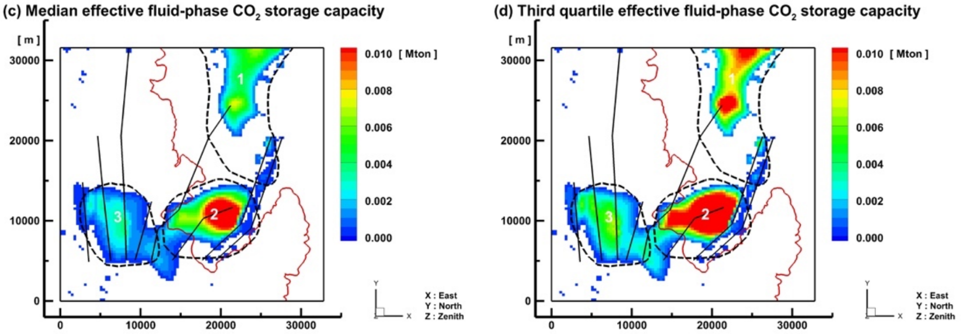

(c) Median effective fluid-phase CO_2 storage capacity

(d) Third quartile effective fluid-phase CO_2 storage capacity

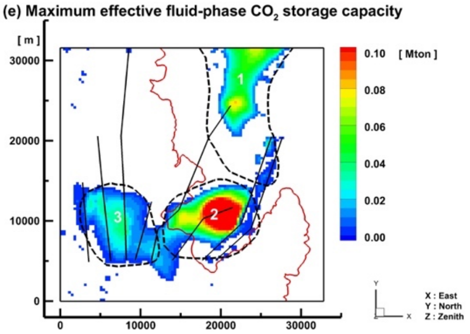

(e) Maximum effective fluid-phase CO_2 storage capacity

Figure 6.15. Top views of three-dimensional grid-wise spatial distributions of (a) minimum, (b) first quartile, (c) median, (d) third quartile, and (e) maximum effective fluid-phase CO_2 storage capacities of the clastic saline formation FCSS in the Pohang Basin with the eight major faults (black solid lines).

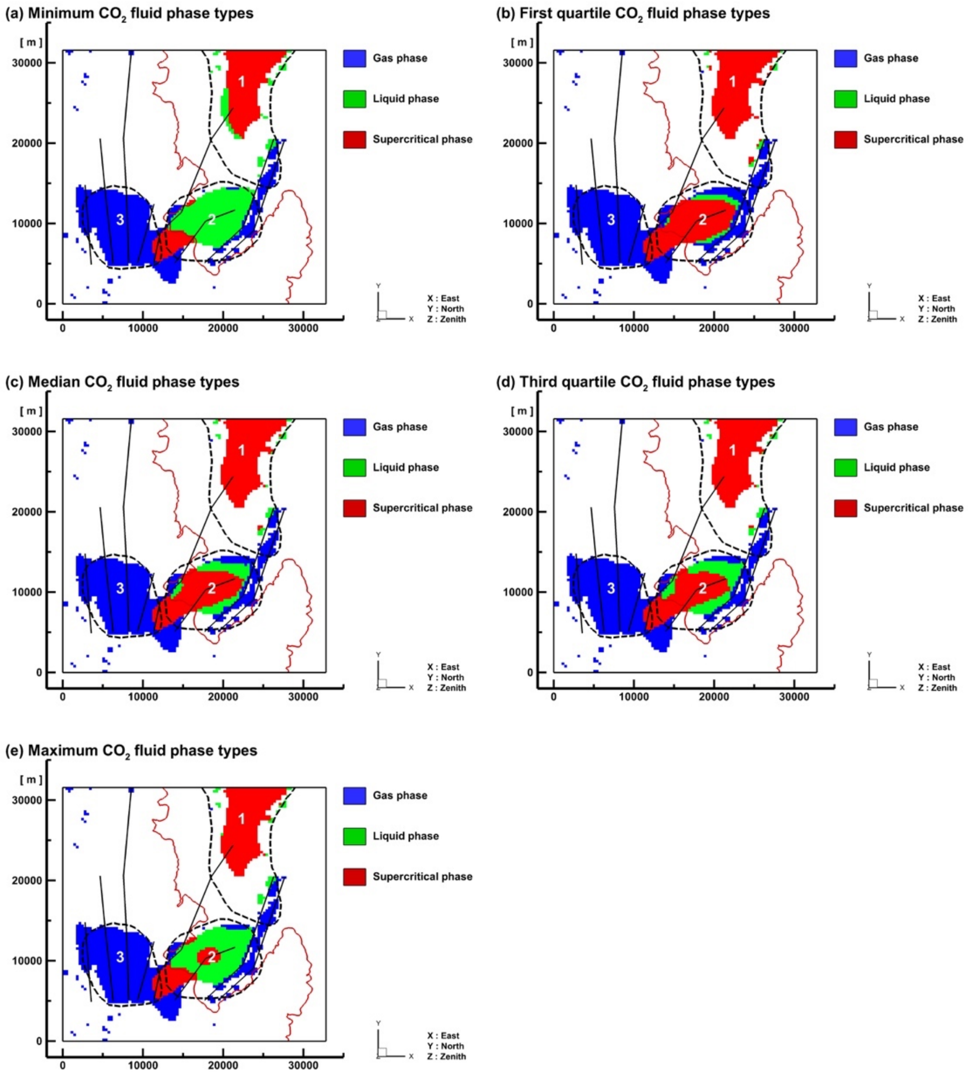

Figure 6.16. Top views of three-dimensional grid-wise spatial distributions of CO_2 fluid phase types corresponding with (a) minimum, (b) first quartile, (c) median, (d) third quartile, and (e) maximum effective fluid-phase CO_2 storage capacities of the clastic saline formation FCSS in the Pohang Basin with the eight major faults (black solid lines).

On the basis of the formation volumes (i.e., first key parameter) and theoretical and effective individual gas-, liquid-, supercritical-, and whole fluid-phase CO_2 storage capacities (i.e., second key parameter), the optimal locations of CO_2 storage in the underlying saline formation FCSS are better in the order of Areas 2, 1, and 3 (Figures 6.13 and 6.15). Although the CO_2 fluid phase type is not a specific key parameter, in terms of the CO_2 fluid phase types, the optimal locations of CO_2 storage in the underlying saline formation FCSS are generally better in the order of Areas 1, 2, and 3 (Figures 6.14 and 6.16). On the contrary, there are exceptional cases that the area of supercritical-phase CO_2 at the CO_2 fluid phase types corresponding with minimum theoretical fluid-phase CO_2 storage capacities (Figure 6.14a) are more distributed than those with maximum theoretical fluid-phase CO_2 storage capacities (Figure 6.14e) and the area of supercritical-phase CO_2 at the CO_2 fluid phase types corresponding with first quartile effective fluid-phase CO_2 storage capacities (Figure 6.16b) are more distributed than those with maximum effective fluid-phase CO_2 storage capacities (Figure 6.14e) This arises because the total pore volume is more dominant factor than the fluid-phase CO_2 density (i.e., CO_2 fluid phase type) for fluid-phase CO_2 storage capacities as mention in Section 6.1. In addition, in terms of the effective individual gas-, liquid-, supercritical-, and whole fluid-phase CO_2

storage densities (i.e., third key parameter), the optimal locations of CO_2 storage in FCSS are consistently better in the order of Areas 1, 2, and 3 (Table 6.2).

As a whole, these first three key parameters suggest that Area 1 is favorable for large-size commercial-scale offshore CO_2 storage, Area 2 is favorable for middle-size demonstration-scale offshore CO_2 storage, and Area 3 is favorable for small-size pilot-scale onshore CO_2 storage. In addition, fortunately, Area 1 is slightly dissected by the three major faults, whereas Areas 2 and 3 are highly dissected by the four and five major faults, respectively. As a result, the optimal locations of CO_2 storage in both SMSS and FCSS are still better in the order of Areas 1, 2, and 3 even though the existence of the major faults (i.e., fourth key parameter) is considered. Thus, the overall suitability ranks of Areas 1, 2, and 3 for geologic CO_2 storage are determined to be the first, second, and third, respectively (Tables 6.1 and 6.2).

7. Discussions

The CSLF methodology (CSLF, 2005; Bachu et al., 2007; Bradshaw et al., 2007; CSLF, 2007, 2008) has discussed that calculating CO_2 density at geologic formation is difficult because it depends on the pressure at geologic formation once it is filled with CO_2. This pressure has to be higher than the initial groundwater pressure in order to achieve CO_2 injection and lower than the maximum bottomhole injection pressure in order to avoid rock fracturing or breaching of the capillary seal. Considering the CO_2 injection pressure and resultant CO_2 density require numerous (site-specific) input parameters and can be changed according to time progress. Thus, the CO_2 injection pressure and resultant CO_2 density, which is difficult to apply at the static volumetrics-based approach, are not considered in this study.

Three-dimensional geologic model is subject to several kinds of uncertainty (Wellmann et al., 2010). Such uncertainties are classified into three different types as data imprecision and quality, interpolation or extrapolation away from known points, and incomplete knowledge of structures in subsurface (Cox, 1982; Mann, 1993; Bárdossy and Fodor, 2001). Among the three different types, data imprecision and quality is the most direct problem to handle and reduce uncertainty. In order to overcome the uncertainty arising from data imprecision and quality, sufficient and reliable geologic data should be collected extensively and applied carefully such as digital topographic map, electronic navigational chart, surface geologic map, offshore geologic cross-sections with geologic structures (faults) and formations. The six offshore geologic cross-sections with geologic structures (faults) and formations used in this study was made by collection and integration of offshore region data such as seismic and ocean topography exploration data and onshore region data such as borehole data of the Pohang Basin and the result of three-dimensional geologic modeling show very good agreement with those above-mentioned analyzed and computerized raw data (i.e., digital topographic map, electronic navigational chart, surface geologic map, offshore geologic cross-sections with geologic structures (faults) and formations). However, if more sufficient and reliable geologic data of the Pohang Basin is collected, it should be compared with the results of three-dimensional geologic modeling and applied carefully to make three-dimensional geologic model more precisely for further studies.

Total porosities and geothermal gradient of the two clastic saline formations in the Pohang Basin used in this study are adopted from the previous works (Huh et al., 1992; Kim, J.C. et al., 2012, 2013; Park et al., 2013; Park and Park, 2016; Kim and Lee, 2007) and assumed to have truncated normal distributions. However, number of total porosities and geothermal gradient data of the two clastic formation in the Pohang Basin may be insufficient to represent the total porosities and geothermal gradient of the two clastic formation in the Pohang Basin. With more sufficient total porosity and geothermal gradient data, more precise CO_2 storage capacity can be evaluated. In addition, the input values of fluid-phase CO_2 storage efficiency parameters and factors are obtained from the more than 20,000 clastic and carbonate hydrocarbon reservoirs in USA, Canada, and other countries (i.e., Average Global Database (AGD)) (IEA GHG, 2009). Thus, fluid-phase CO_2 storage efficiency parameters and factors used in this study are highly reliable and broadly applicable. In other words, fluid-phase CO_2 storage efficiency parameters and factors used in this study are not specific values for the Pohang Basin. If more sufficient and reliable site specific geologic data is collected, the intrinsic geologic storage efficiency parameters such as net-to-total area ratio (E_{A_n/A_t}), the net-to-gross thickness ratio (E_{h_n/h_g}), and the effective-to-total porosity ratio (E_{n_e/n_t}) can be removed using the result of three-dimensional geologic lithofacies modeling. The fluid-phase CO_2 displacement storage efficiency parameters also can be removed using the result of numerical simulation of CO_2 behavior based on the three-dimensional geologic grid model. Thus, if more sufficient and reliable total porosity and geothermal gradient of the two clastic saline formations in the Pohang Basin are collected and the actual and specific values of the intrinsic geologic storage efficiency parameters and the fluid-phase CO_2 displacement storage efficiency parameters of two saline formations SMSS and FCSS of the Pohang Basin are known, they should be applied to evaluate CO_2 storage capacity more precisely and reduce uncertainty of the result of theoretical and effective fluid-phase CO_2 storage capacities for further studies.

8. Conclusions

A series of probabilistic evaluation is performed using a linked methodology to estimate individual gas-, liquid-, supercritical-, and whole fluid-phase carbon dioxide (CO_2) storage capacities of the target clastic saline formations in the Pohang Basin, Korea of the Tertiary (Neogene) age. In order to evaluate probabilistically, three-dimensional geologic modeling and grid-based Monte Carlo simulation are performed sequentially as a linked methodology. The two clastic saline formations, which are the sandstone-dominant Fluvial Conglomerate and Sandstone (FCSS) and Shallow Marine Sandstone (SMSS) in the Pohang Basin, are selected as the target clastic saline formations.

A series of three-dimensional geologic modeling was performed first using a geostatistical geologic modeling program to establish the three-dimensional geologic structure, stratigraphy, grid, and formation models of the Pohang Basin. The results of the three-dimensional geologic modeling show that the six geologic formations are distributed very complicatedly both onshore and offshore with irregular depths and thicknesses, and they are partly dissected and offset by the eight major faults. The two clastic saline formations FCSS and SMSS are deep and thick at the three prospective areas such as Area 1 (northeastern offshore area), Area 2 (southern offshore area near the Yeongil Bay), and Area 3 (western onshore area near the Pohang City) in the modeling domain.

A series of grid-based Monte Carlo simulation was then performed using a grid information data conversion model and a probabilistic theoretical and effective fluid-phase CO_2 storage capacity evaluation model to estimate the theoretical and effective individual gas-, liquid-, supercritical-, and whole fluid-phase CO_2 storage capacities of the two clastic saline formations SMSS and FCSS in the Pohang Basin as an open system. The results of the grid-based Monte Carlo simulation show the following three main contents.

First, in the two clastic saline formations SMSS and FCSS, CO_2 exists as gas, liquid, and supercritical phases with the corresponding distinctive density ranges depending on the pressure and temperature with depth. The fluid-phase CO_2 storage efficiency factor of the SMSS and FCSS shows a log-normal distribution, and the five fluid-phase CO_2 storage efficiency parameters meet very well the original (input) statistical values from the previous works.

Second, the theoretical individual gas-, liquid-, supercritical-, and whole fluid-phase CO_2 storage capacities of the SMSS and FCSS all show asymmetric normal distributions. On the other hand, the effective individual gas-, liquid-, supercritical-, and whole fluid-phase CO_2 storage capacities of the saline formations all show log-normal distributions, and their values are much lower than the values of the theoretical individual gas-, liquid-, supercritical-, and whole fluid-phase CO_2 storage capacities. This arises because the fluid-phase CO_2 storage efficiency factor shows a log-normal distribution and is much less than unity. As a whole, the theoretical and effective fluid-phase CO_2 storage capacities are probabilistically higher in the SMSS compared with the FCSS because the SMSS has a larger total pore volume. The mean theoretical fluid-phase CO_2 storage capacities of the SMSS and FCSS are equal to 2,511.60 Mton and 1,370.91 Mton, respectively. The mean effective fluid-phase CO_2 storage capacities of the SMSS and FCSS are equal to 64.19 Mton and 35.32 Mton, respectively. On the other hand, the effective individual gas-, liquid-, supercritical-, and whole fluid-phase CO_2 storage capacities of the SMSS and FCSS are better to be evaluated again using the linked methodology to refine their uncertainties when the fluid-phase CO_2 storage efficiency factors specific to the saline formations are determined more reasonably and realistically. The results of the linked methodology is compared with the results of the US DOE methodology to identify the improvements and developments.

Third, in the SMSS, the grid-wise (elemental) theoretical and effective fluid-phase CO_2 storage capacities are probabilistically higher at Area 1 (mainly as supercritical and liquid phases), intermediate at Area 2 (mainly as liquid and gas phases), and lower at Area 3 (mainly as a gas phase). However, in the FCSS, the grid-wise theoretical and effective fluid-phase CO_2 storage capacities are probabilistically higher at Area 2 (mainly as supercritical and liquid phases), intermediate at Area 1 (mainly as a supercritical phase), and lower at Area 3 (mainly as a gas phase). As a whole, the grid-wise theoretical and effective fluid-phase CO_2 storage capacities are probabilistically higher in the SMSS compared with the FCSS.

Finally, four key criteria (parameters) for selecting or ranking the optimal CO_2 storage locations were decided by summarizing and analyzing the results of the three-dimensional geologic modeling and grid-based Monte Carlo simulation. They are the (1) formation volumes, (2) effective individual gas-, liquid-, supercritical-, and whole fluid-phase CO_2 storage capacities, and (3) effective individual gas-, liquid-, supercritical-, and whole fluid-phase CO_2 storage densities (intensities) of the clastic saline formations SMSS and FCSS in terms of CO_2 fluid masses and phases as well as the (4) existence of the major faults at the three prospective areas. On the basis of the four key criteria (parameters), the overall suitability ranks of Areas 1, 2, and 3 for geologic CO_2 storage were determined to be the first, second, and third, respectively.

On the other hand, the optimal CO_2 storage locations in the SMSS and FCSS are better to be determined again using dynamic numerical reservoir simulations to refine their uncertainties when the hydrogeological characteristics of the Pohang Basin with the eight major faults are identified more reasonably and realistically.

In conclusion, the results of this study show that a linked methodology of three-dimensional geologic modeling and grid-based Monte Carlo simulation presented in this study significantly overcomes the limitations of the US DOE methodology and increases its applicability and feasibility. Thus, it can be utilized as a practical probabilistic evaluation tool to estimate rigorously the theoretical and effective fluid-phase CO_2 storage capacities of clastic saline formations in terms of CO_2 fluid masses and phases and even to determine quantitatively optimal locations of CO_2 storage or injection. Therefore, it may be concluded that the linked methodology may find some useful applications in many worldwide geologic CO_2 storage projects.

References

Aitchison, J., Shen, S.M., 1980. Logistic-normal distributions: some properties and uses. Biometrika 67 (2), 261-272. https://doi.org/10.2307/2335470.

Bachu, S., Gunter, W.D., Perkins, E.H., 1994. Aquifer disposal of CO_2: hydrodynamic and mineral trapping. Energy Convers. Manage. 35 (4), 269-279. https://doi.org/10.1016/0196-8904(94)90060-4.

Bachu, S., Bonijoly, D., Bradshaw, J., Burruss, R., Holloway, S., Christensen, N.P., Mathiassen, O.M., 2007. CO_2 storage capacity estimation: methodology and gaps. Int. J. Greenh. Gas Control 1 (4), 430-443. https://doi.org/10.1016/S1750-5836(07)00086-2.

Bachu, S., Adams, J.J., 2003. Sequestration of CO_2 in geological media in response to climate change: capacity of deep saline aquifers to sequester CO_2 in solution. Energy Convers. Manage. 44 (20), 3151-3175. https://doi.org/10.1016/S0196-8904(03) 00101-8.

Bárdossy, G., Fodor, J., 2001. Traditional and new ways to handle uncertainty in geology. Nat. Resour. Res. 10 (3), 179-187. https://doi.org/10.1023/A:1012513107364

Birkholzer, J.T., Zhou, Q., 2009. Basin-scale hydrogeologic impacts of CO_2 storage: capacity and regulatory implications. Int. J. Greenh. Gas Control 3 (6), 745-756. https://doi.org/10.1016/j.ijggc.2009.07.002.

Blondes, M.S., Brennan, S.T., Merrill, M.D., Buursink, M.L., Warwick, P.D., Cahan, S.M., Cook, T.A., Corum, M.D., Craddock, W.H., DeVera, C.A, Drake II, R.M., Drew, L.J., Freeman, P.A., Lohr, C.D., Olea, R.A., Roberts-Ashby, T.L., Slucher, E.R., Varela, B.A., 2013. National Assessment of Geologic Carbon Dioxide Storage Resources - Methodology Implementation. Open-File Report 2013-1055. United State Geological Survey (USGS), Reston, Virginia, USA, 26 pp.

Bradshaw, B.E., Spencer, L.K., Lahtinen, A.C., Khider, K., Ryan, D.J., Colwell, J.B., Chirinos, A., Bradshaw, J., 2009. Queensland Carbon Dioxide Geological Storage Atlas. Technical Report. Greenhouse Gas Storage Solutions on behalf of Queensland Department of Employment, Economic Development and Innovation, Brisbane, Queensland, Australia, 82 pp.

Bradshaw, B.E., Spencer, L.K., Lahtinen, A.L., Khider, K., Ryan, D.J., Colwell, J.B., Chirinos, A., Bradshaw, J., Draper, J.J., Hodgkinson, J., McKillop, M., 2011. An assessment of Queensland's CO_2 geological storage prospectivity - the Queensland CO_2 geological storage atlas.

Energy Procedia 4, 4583-4590. https://doi.org/10.1016/j.egypro.2011.02.417.

Bradshaw, J., Bachu, S., Bonijoly, D., Burruss, R., Holloway, S., Christensen, N.P., Mathiassen, O.M., 2007. CO_2 storage capacity estimation: issues and development of standards. Int. J. Greenh. Gas Control 1 (1), 62-68. https://doi.org/10.1016/S1750- 5836(07)00027-8.

Brennan, S.T., Burruss, R.C., Merrill, M.D., Freeman, P.A., Ruppert, L.F., 2010. A Probabilistic Assessment Methodology for the Evaluation of Geologic Carbon Dioxide Storage. Open-File Report 2010-1127. United States Geological Survey (USGS), Reston, Virginia, USA, 31 pp.

Burruss, R.C., Brennan, S.T., Freeman, P.A., Merrill, M.D., Ruppert, L.F., Becker, M.F., Herkelrath, W.N., Kharaka, Y.K., Neuzil, C.E., Swanson, S.M., Cook, T.A., Klett, T.R., Nelson, P.H., Schenk, C.J., 2009. Development of a Probabilistic Assessment Methodology for Evaluation of Carbon Dioxide Storage. Open-File Report 2009-1035. United States Geological Survey (USGS), Reston, Virginia, USA, 81 pp.

Choi, D.L., Kim, S.R., Suk, B.C., Oh, J.K., 1993. Shallow geological structure of the Yongil Bay, southeast coast of Korea. Korean Jour. of Petrol. Geol. 1 (1), 53-62.

Choi, P.Y., 2006. ‘Singwang strike-slip duplex’ around the Pohang Basin, SE Korea: its structural evolution and role in opening and fill of the Miocene basin. Geosci. J. 10 (2), 145-157.

CO2CRC, 2008. Storage Capacity Estimation, Site Selection and Characterisation for CO_2 Storage Projects. Technical Report RPT08-1001. Cooperative Research Centre for Greenhouse Gas Technologies (CO2CRC), Canberra, ACT, Australia, 52 pp.

Cox Jr, L. A., 1982. Artifactual uncertainty in risk analysis. Risk Anal. 2 (3), 121-135. https://doi.org/10.1111/j.1539-6924.1982.tb01375.x

CSLF, 2005. Task Force for Review and Identification of Standards for CO_2 Storage Capacity Measurement. Phase I Final Report CSLF-T-2005-09. Carbon Sequestration Leadership Forum (CSLF), Washington, DC, USA, 22 pp.

CSLF, 2007. Estimation of CO_2 Storage Capacity in Geological Media. Phase II Final Report CSLF-T-2007-04. Carbon Sequestration Leadership Forum (CSLF), Washington, DC, USA, 42 pp.

CSLF, 2008. Comparison between Methodologies Recommended for Estimation of CO_2 Storage Capacity in Geological Media. Phase III Final Report CSLF-T-2008-04. Carbon Sequestration Leadership Forum (CSLF), Washington, DC, USA, 17 pp.

CST, 2009. National Carbon Mapping and Infrastructure Plan - Australia. Full Report. Carbon Storage Taskforce (CST), Resources Division, Department of Resources, Energy and Tourism, Canberra, ACT, Australia, 126 pp.

Cheon, Y., Son, M., Song, C.W., Kim, J.S., Sohn, Y.K., 2012. Geometry and kinematics of the Ocheon Fault System along the boundary between the Miocene Pohang and Janggi basins, SE Korea, and its tectonic implications. Geosci. J. 16 (3), 253-273. https://doi.org/10.1007/s12303 012-0029-0.

Gammer, D., Green, A., Holloway, S., Smith, G., 2011. The Energy Technologies Institute's UK CO_2 Storage Appraisal Project (UKSAP). In: Proceedings of the Society of Petroleum Engineers (SPE) Offshore Europe Oil and Gas Conference and Exhibition, Aberdeen, UK, SPE-148426.

Goodman, A., Hakala, A., Bromhal, G., Deel, D., Rodosta, T., Frailey, S., Small, M., Allen, D., Romanov, V., Fazio, J., Huerta, N., McIntyre, D., Kutchko, B., Guthrie, G., 2011. U.S. DOE methodology for the development of geologic storage potential for carbon dioxide at the national and regional scale. Int. J. Greenh. Gas Control 5 (4), 952-965. https://doi.org/10.1016/j.ijggc.2011.03.010.

Goodman, A., Bromhal, G., Strazisar, B., Rodosta, T., Guthrie, G., 2013. Comparison of Publicly Available Methods for Development of Geologic Storage Estimates for Carbon Dioxide in Saline Formations. Technical Report NETL-TRS-1-2013. National Energy Technology Laboratory (NETL), Morgantown, West Virginia, USA, 182 pp.

Guyonnet-Benaize, C., Lamarche, J., Masse, J.P., Villeneuve, M., Viseur, S., 2010. 3D structural modelling of small-deformations in poly-phase fault pattern. Application to the mid-cretaceous Durance uplift, Provence (SE France). J. Geodyn. 50 (2), 81-93. https://doi.org/10.1016/j.jog.2010.03.003

Gwak, S.H., Lee, D.S., 2001. 3-D Visualization of reservoir characteristics through GOCAD (in Korean with English abstract). J. Korean Soc. Earth Explor. Geophys. 4, 80-83.

Heidug, W., 2013. Methods to Assess Geologic CO_2 Storage Capacity: Status and Best Practice. IEA Workshop Report. International Energy Agency (IEA), Paris, France, 43 pp.

Hitchon, B. (Ed.), 1996. Aquifer Disposal of Carbon Dioxide: Hydrodynamic and Mineral Trapping - Proof of Concept. Geoscience Publishing Limited, Sherwood Park, Alberta, Canada, 165 pp.

Holloway, S., 1997. An overview of the underground disposal of carbon dioxide. Energy Convers. Manage. 38 (Supplement), S193-S198. https://doi.org/10.1016/S0196- 8904(96)00268-3.

Huh, D.G., Kim, H.T., Lee, K.H., 1992. A petrophysical properties of petroleum potential reservoirs (in Korean with English abstract). J. Korean Soc. Miner. Energy Resour. Eng. 29 (4), 178-185.

Huntec Ltd., 1967. Report on the offshore geophysical survey in the Pohang area, Republic of Korea. UN ECAFE/CCOP Technical Bulletin 1, 1-12.

IEA GHG, 2009. Development of Storage Coefficients for CO_2 Storage in Deep Saline Formations. Technical Report 2009/13. International Energy Agency Greenhouse Gas R&D Programme (IEA GHG), Cheltenham, Gloucester, UK, 94 pp.

Jeong, J., Jang, W.I., 2011. Estimation of distribution of the weak soil layer for using geostatistics (in Korean with English abstract). J. Korean Soc. Mar. Eng. 35, 1132-1140.

Kaufmann, O., Martin, T., 2009. Reprint of “3D geological modeling from boreholes, cross-sections and geological maps, application over former natural gas storages in coal mines”. Comput. Geosci. 35 (1), 70-82. https://doi.org/10.1016/S0098-3004(08)00227-6

KHOA, 2011. Electronic Navigational Chart of Pohang Harbor Vicinity Sheet, scale 1:75,000. Sheet 175 (DXF File). Korea Hydrographic and Oceanographic Administration (KHOA), Busan, Korea.

KMA, 2011. Climatological normals of Korea for 1981~2010 (in Korean and English). Technical Report 11-1360000-000077-14, 678 pp., Korea Meteorological Administration (KMA), Seoul, Korea, 678 pp.

Kihm, J.H., Park, J.Y., Kim, J.M., 2017. CO_2-STOR: A Probabilistic Evaluation Model for Theoretical and Effective Multi-Fluid-Phase Carbon Dioxide Storage Capacities of Geologic Formations (Saline Formations), version 1.1. Technical Report GGEL-2017- 5. Geological and Groundwater Engineering Laboratory, School of Earth and Environmental Sciences, Seoul National University, Seoul, Korea, 197 pp.

Kim, C.S., Kihm, J.H., Lee, S., Kim, J.M., 2013. Grid Converter (Including GOCAD2TOUGH Module): A Conversion Model for Grid, Material Property, and Physico-Chemical Condition Information Data between Three-Dimensional Geologic Modeling Programs, Behavior Prediction Models, Performance Evaluation Models, and Pre- and Post-Processing Programs, version 1.0. Technical Report GGEL-2013-5. Geological and Groundwater Engineering Laboratory, School of Earth and Environmental Sciences, Seoul National University, Seoul, Korea, 34 pp.

Kim, D.H., Ryu, D.W., Lee, J.H., Choi, I.G., Kim, J.K., Lee, W.J., 2010. Comparative studies of kriging methods for estimation of geo-layer distribution of Song-Do international city in Incheon (in Korean with English abstract). J. Korean Soc. Rock Mech. 26, 57-64.

Kim, H.C., Lee, Y., 2007. Heat flow in the Republic of Korea. J. Geophys. Res. 112 (B5), B05413. https://doi.org/10.1029/2006JB004266.

Kim, J.C., Lee, Y.I., Son, M., Yoon, S.H., Yi, K., Cheong, D., Ryang, W.H., Kim, Y.S., Kim, S. B., Kim, J.M., Kim, H.S., Keehm, Y., Cho, G.C., Park, E., Kim, T., Won, K.S., Lee, M., 2012. Characterization of Storage Strata and Development of Basis Design Technology for Demonstration of CO_2 Geological Storage (in Korean). First-Year Annual Report GP2012-030-1. Korea Institute of Geoscience and Mineral Resources (KIGAM), Daejeon, Korea, 168 pp.

Kim, J.C., Lee, Y.I., Son, M., Yoon, S.H., Yi, K., Cheong, D., Ryang, W.H., Kim, Y.S., Kang, S.M., Kim, J.M., Kim, H.S., Keehm, Y., Cho, G.C., Park, E., Kim, T., Won, K.S., Lee, M., 2013. Characterization of Storage Strata and Development of Basis Design Technology for Demonstration of CO_2 Geological Storage (in Korean). Second-Year Annual Report GP2012-030-2. Korea Institute of Geoscience and Mineral Resources (KIGAM), Daejeon, Korea, 442 pp.

Kim, J.M., 2011. Integrated Prediction and Analysis of Performance of Target Geologic Formation Systems for Geologic Storage of Carbon Dioxide (in Korean). First-Year Annual Report 2010T100100500. Geological and Groundwater Engineering Laboratory, School of Earth and Environmental Sciences, Seoul National University, Seoul, Korea, 72 pp.

Kim, J.M., 2012a. Integrated Prediction and Analysis of Performance of Target Geologic Formation Systems for Geologic Storage of Carbon Dioxide (in Korean). Second-Year Annual Report 2010201020001A. Geological and Groundwater Engineering Laboratory, School of Earth and Environmental Sciences, Seoul National University, Seoul, Korea, 54 pp.

Kim, J.M., 2012b. Development of Integrated Prediction and Mitigation Technologies for Groundwater System Environment Changes Due to Geologic Storage of Carbon Dioxide (in Korean). Final Report 174-091-003. Geological and Groundwater Engineering Laboratory, School of Earth and Environmental Sciences, Seoul National University, Seoul, Korea, 252 pp.

Kim, S.J., Park, H.D., 2009. Development of software for mineral resoureestimation and 3D modeling using variogram (in Korean with English abstract). J. Korean Soc. Geosyst. Eng. 46, 151-159.

Knopf, S., May, F., Müller, C., Gerling, J.P., 2010. Neuberechnung möglicher kapazitäten zur CO_2-speicherung in tiefen aquifer-strukturen (Recalculation of potential capacities for CO_2 storage in deep aquifer structures) (in German). Energiewirtschaftliche Tagesfragen 60 (4), 76-80.

Koo, C.M., Jeon, S.W., 2005. Using conditional simulation to estimate rock mass properties and assess the uncertainty (in Korean with English abstract). J. Korean Soc. Rock Mech. 3, 81-95.

Koo, C.M., Hong, C.W., Jeon, S.W., 2006. Estimation of rock mass rating(RMR) and assessment of its uncertainty using conditional simulations (in Korean with English abstract). J. Korean Soc. Rock Mech. 16, 135-145.

Kopp, A., Probst, P., Class, H., Hurter, S., Helmig, R., 2009. Estimation of CO_2 storage capacity coefficients in geologic formations. Energy Procedia 1 (1), 2863-2870.

Lee, B.J., Choi, S.J., Chwae, U.C., Ryoo, C.R., 1999. Characteristics of the Quaternary faulting of the Wolpyeong, Yangsan, S.E. Korea (in Korean with English abstract). J. Geol. Soc. Korea 35 (3), 179-188.

Li, P., Zhou, D., Zhang, C., Chen, G., 2015. Assessment of the effective CO_2 storage capacity in the Beibuwan Basin, offshore of southwestern P. R.

China. Int. J. Greenh. Gas Control 37, 325-339. https://doi.org/10.1016/j.ijggc.2015.03.033.

Mallet, J.L., 1989. Discrete smooth interpolation. ACM (Association for Computing Machinery) Trans. Graphics 8 (2), 121-144. https://doi.org/10.1145/62054.62057.

Mallet, J.L., 1992a. GOCAD: a computer aided design program for geological applications. In: Turner, A.K. (Ed.), Three-Dimensional Modeling with Geoscientific Information Systems. NATO Advanced Study Institute (ASI) Series, Vol. 354. Kluwer Academic Publishers, Dordrecht, Netherlands, pp. 123-141. https://doi.org/10.1007/978-94011-2556-7_11.

Mallet, J.L., 1992b. Discrete smooth interpolation in geometric modelling. Comput.-Aided Des. 24 (4), 178-191. https://doi.org/10.1016/00104485(92)90054-E.

Mallet, J.L., 1997. Discrete modeling for natural objects. Math. Geol. 29 (2), 199-219. https://doi.org/10.1007/BF02769628.

Mann, C. J., 1993. Uncertainty in Geology. Computers in geology---25 years of progress. Oxford University Press, Oxford, England, UK, pp. 241-254.

McKay, M.D., Beckman, R.J., Conover, W.J., 1979. A comparison of three methods for selecting values of input variables in the analysis of output from a computer code. Technometrics 21 (2), 239-245. https://doi.org/10.2307/1268522.

Metz, B., Davison, O., de Coninck, H.C., Loos, M., Mayer, L.A. (Eds.), 2005. Intergovernmental Panel on Climate Change (IPCC) Special Report on Carbon Dioxide Capture and Storage. Cambridge University Press, Cambridge, UK, 431 pp.

NACAP, 2012. The North American Carbon Storage Atlas, first edition. Technical Report. North American Carbon Atlas Partnership (NACAP), National Energy Technology Laboratory (NETL), Pittsburgh, Pennsylvania, USA, 51 pp.

NETL, 2007. Carbon Sequestration Atlas of the United States and Canada. Technical Report. National Energy Technology Laboratory (NETL), Pittsburgh, Pennsylvania, USA, 87 pp.

NETL, 2008. Carbon Sequestration Atlas of the United States and Canada, second edition. Technical Report. National Energy Technology Laboratory (NETL), Pittsburgh, Pennsylvania, USA, 141 pp.

NETL, 2010. Carbon Sequestration Atlas of the United States and Canada, third edition. Technical Report. National Energy Technology Laboratory (NETL), Pittsburgh, Pennsylvania, USA, 161 pp.

NETL, 2012. Carbon Utilization and Storage Atlas of the United States, fourth edition. Technical Report. National Energy Technology Laboratory (NETL), Pittsburgh, Pennsylvania, USA, 129 pp.

NETL, 2015. Carbon Storage Atlas, fifth edition. Technical Report. National Energy Technology Laboratory (NETL), Pittsburgh, Pennsylvania, USA, 113 pp.

NGII, 2013. Digital Topographic Maps of Cheongha, Chilpo, Pohang, Hwanho, Daebo, Yeonil, Yongdeok, and Guryongpo Sheets, scale 1:25,000. Sheets 369141, 369142, 369143, 369144, 369153, 359021, 359022, and 359031 (DXF Files). National Geographic Information Institute (NGII), Suwon, Korea.

NPD, 2011. CO_2 storage atlas: Norwegian North Sea. Technical Report, 72 pp., Norwegian Petroleum Directorate (NPD), Stavanger, Norway.

Na, J.Y., Lee, S.W., Cho, K.D., 1991. A study on sea water and ocean current in the sea adjacent to Korea Peninsula - the vertical structure of temperatures in the East Sea of Korea (in Korean with English abstract). Bull. Korean Fish. Soc. 24 (4), 215-228.

Neele, F., Hofstee, C., Dillen, M., Nepveu, M., 2011a. Independent Storage Assessment of Offshore CO_2 Storage Options for Rotterdam - Summary Report. TNO Report TNO-060-UT-2011-00809. TNO (Geological Survey of the Netherlands), Utrecht, Netherlands, 48 pp.

Neele, F., Nepveu, M., Hofstee, C., Meindertsma, W., 2011b. CO_2 Storage Capacity Assessment Methodology. TNO Report TNO-060-UT-2011-00810. TNO (Geological Survey of the Netherlands), Utrecht, Netherlands, 45 pp.

Neele, F., ten Veen, J., Wilschut, F., Hofstee, C., 2012. Independent Assessment of High-Capacity Offshore CO_2 Storage Options. TNO Report TNO-060-UT-2012-00414/B. TNO (Geological Survey of the Netherlands), Utrecht, Netherlands, 93 pp.

Nicot, J.P., 2008. Evaluation of large-scale CO_2 storage on fresh-water sections of aquifers: an example from the Texas Gulf Coast Basin. Int. J. Greenh. Gas Control 2 (4), 582-593. https://doi.org/10.1016/j.ijggc.2008.03.004.

Ogawa, T., Nakanishi, S., Shidahara, T., Okumura, T., Hayashi, E., 2011. Saline-aquifer CO_2 sequestration in Japan - methodology of storage capacity assessment. Int. J. Greenh. Gas Control 5 (2), 318-326. https://doi.org/10.1016/j.ijggc.2010.09.009.

Paradigm, 2014. GOCAD (Geological Object Computer Aided Design) User Guide. Manual. Paradigm, Houston, Texas, USA.

Park, J., Park, H.D., 2016. An analysis of pore network of drilling core from Pohang Basin for geological storage of CO_2 (in Korean with English abstract). Tunnel Underground Space 26 (3), 181-191. https://doi.org/10.7474/TUS.2016.26.3.181.

Park, J., Lee, M., Wang, S., 2013. Study on the geochemical weathering process of sandstones and mudstones in Pohang Basin at CO_2 storage condition (in Korean with English abstract). Econ. Environ. Geol. 46 (3), 221-234. https://doi.org/10.9719/ EEG.2013.46.3.221.

Probst, P., 2008. Numerical simulations of CO_2 injection into saline aquifers: estimation of storage capacity and arrival times using multiple realizations of heterogeneous permeability fields. M.S. thesis, University of Stuttgart, Stuttgart, Germany, 78 pp.

Pruess, K., 2005. ECO2N: A TOUGH2 Fluid Property Module for Mixtures of Water, NaCl, and CO_2. Technical Report LBNL-57952. Lawrence Berkeley National Laboratory (LBNL), University of California, Berkeley, California, USA, 66 pp.

Pruess, K., Oldenburg, C., Moridis, G., 2012. TOUGH2 User's Guide, version 2.1. Technical Report LBNL-43134. Lawrence Berkeley National Laboratory (LBNL), University of California, Berkeley, California, USA, 197 pp.

Sohn, Y.K., Son, M., 2004. Synrift stratigraphic geometry in a transfer zone coarse-grained delta complex, Miocene Pohang Basin, SE Korea.

Sedimentology 51 (6), 1387-1408. https://doi.org/10.1111/j.1365 3091.2004.00679.x.

Sohn, Y.K., Rhee, C.W., Shon, H., 2001. Revised stratigraphy and reinterpretation of the Miocene Pohang basinfill, SE Korea: sequence development in response to tectonism and eustasy in a back-arc basin margin. Sediment. Geol. 143 (3-4), 265-285. https://doi.org/10.1016/S0037-0738(01)00100-2.

Sopher, D., Juhlin, C., Erlström, M., 2014. A probabilistic assessment of the effective CO_2 storage capacity within the Swedish sector of the Baltic Basin. Int. J. Greenh. Gas Control 30, 148-170. https://doi.org/10.1016/j.ijggc.2014.09.009.

Spencer, L.K., Bradshaw, J., Bradshaw, B.E., Lahtinen, A.L., Chirinos, A., 2011. Regional storage capacity estimates: prospectivity not statistics. Energy Procedia 4, 4857-4864. https://doi.org/10.1016/j.egypro.2011.02.453.

Su, X., Xu, W., Du, S., 2013. Basin-scale CO_2 storage capacity assessment of deep saline aquifers in the Songliao Basin, northeast China. Greenh. Gases Sci. Technol. 3 (4), 266-280. https://doi.org/10.1002/ghg.1354.

Szulczewski, M., Juanes, R., 2009. A simple but rigorous model for calculating CO_2 storage capacity in deep saline aquifers at the basin scale.

Energy Procedia 1 (1), 3307-3314. https://doi.org/10.1016/j.egypro.2009.02.117.

Szulczewski, M.L., MacMinn, C.W., Herzog, H.J., Juanes, R., 2012. Lifetime of carbon capture and storage as a climate-change mitigation technology. Proc. Natl. Acad. Sci. USA 109 (14), 5185-5189. https://doi.org/10.1073/pnas.1115347109.

Um, S.H., Lee, D.W., Bak, B.S., 1964. Explanatory Text of the Geological Map of Pohang Sheet, scale 1:50,000 (in Korean and English). Technical Report Sheet-7022-II (Map Sheet). Geological Survey of Korea (GSK), Seoul, Korea, 37 pp.

van der Meer, L.G.H., 1992. Investigations regarding the storage of carbon dioxide in aquifers in the Netherlands. Energy Convers. Manage. 33 (5), 611-618. https://doi. org/10.1016/0196-8904(92)90063-3.

van der Meer, L.G.H., Yavuz, F., 2009. CO_2 storage capacity calculations for the Dutch subsurface. Energy Procedia 1 (1), 2615-2622. https://doi.org/10.1016/j.egypro. 2009.02.028.

Vilain, D., 2010. 3D modelling and restoration of the Vargfors Basin, Certral Skellefte District, Northern Sweden, using gOcad and MOVE software. M.S. thesis, Lulea University of Technology, Lulea, Sweden, 19 pp.

Wang, G., Huang, L., 2012. 3D geological modeling for mineral resource assessment of the Tongshan Cu deposit, Heilongjiang Province, China. Geosci. Front. 3 (4), 1-9. https://doi.org/10.1016/j.gsf.2011.12.012

Wellmann, J.F., Horowitz, F.G., Schill, E., Regenauer-Lieb, K., 2010. Towards incorporating uncertainty of structural data in 3D geological inversion. Tectonophysics 490 (3-4), 141-151. https://doi.org/10.1016/j.tecto.2010.04.022

Yoon, S.H., 1994. The eastern continental margin of Korea: seismic stratigraphy, geologic structure and tectonic evolution. Unpublished Ph.D. thesis, Seoul National University, Seoul, Korea, 232 pp.

Yoon, S.H., 2013. Exploration Data Collection and Integration and Basin Analysis for the Pohang Basin (Yeongil Bay), Korea (in Korean). Technical Report GP2012-030-2-II-4. Environmental Geology Laboratory, Department of Earth and Marine Sciences, Jeju National University, Jeju, Korea, 21 pp.

Yoon, S.H. and Chough, S.K., 1993. Evolution of Neogene sedimentary basins in the eastern continental margin of Korea. Korean Jour. of Petrol. Geol. 1 (1), 15-27.

Yoon, S.H. and Chough, S.K., 1995. Regional strike slip in the eastern continental margin of Korea and its tectonic implications for the evolution of Ulleung Basin, East Sea (Sea of Japan). Geol. Soc. Am. Bull., 107 (1), 83-97.

Zanchi, A., Francesca, S., Stefano, Z., Simone, S., Graziano, G., 2007. 3D reconstruction of complex geological bodies: Examples from the Alps. Comput. Geosci. 35 (1), 49-69. https://doi.org/10.1016/j.cageo.2007.09.003

Zhou, Q., Birkholzer, J.T., Tsang, C.F., Rutqvist, J., 2008. A method for quick assessment of CO_2 storage capacity in closed and semi-closed saline formations. Int. J. Greenh. Gas Control 2 (4), 626-639. https://doi.org/10.1016/j.ijggc.2008.02.004.

국문 초록 (Abstract in Korean)

개별 기체, 액체, 초임계상 및 유체상 전체 이산화탄소 저장 용량을 확률론적으로 평가하기 위해 연계 방법론이 적용되었다. 개별 기체, 액체, 초임계상 및 유체상 전체 이산화탄소 저장 용량의 확률론적 평가를 위하여 격자 기반 지층 부피, 격자 기반 이산화탄소 밀도, 그리고 격자 기반 이산화탄소 저장 용량이 순차적인 삼차원 지질 모델링과 격자 기반 몬테카를로 시뮬레이션을 이용하여 평가되었다. 저장 대상 지층으로 포항분지의 사암이 지배적인 천해성 사암층(SMSS)과 하성 역암 및 사암층(FCSS) 두 대염수층이 선정되었다. 삼차원 지질 모델링 결과에서 여섯 개의 지층은 육지와 연안 모두에서 불규칙한 심도와 두께로 매우 복잡하게 분포하고 여덟 개의 주요 단층에 의해서 부분적으로 절개되고 갈라져 있음을 보여준다. FCSS 와 SMSS 두 대염수층은 모델링 영역 내의 유망 지역인 지역 1, 2, 3 에서 심도가 깊고 두께가 두껍다. 격자 기반 몬테카를로 시뮬레이션의 결과에서는 다음 세 가지 주요 사항을 보여준다. 첫 번째로 SMSS 와 FCSS 두 대염수층에서 이산화탄소는 심도의 압력과 온도에 따라 고유한 밀도 범위를 갖는 기체, 액체, 초임계상으로 존재하는 것으로 나타났다. 두 번째로 이론 개별 기체, 액체, 초임계상 및 유체상 전체 유체상 이산화탄소 저장 용량은 모두 비대칭 정규분포를 보인다. 반면에 유효 개별 기체, 액체, 초임계상 및 유체상 전체 유체상 이산화탄소 저장 용량은 모두 로그 정규분포를 보이며 그 값은 이론 개별 기체, 액체,

초임계상 및 유체상 전체 유체상 이산화탄소 저장 용량보다 훨씬 작다. 세 번째로 SMSS 에서는 격자 기반 이론 및 유효 유체상 이산화탄소 저장 용량은 지역 1(주로 초임계 및 액체상)에서 높게, 지역 2(주로 액체 및 기체상)에서 중간으로, 지역 3(주로 기체상)에서 낮게 나타난다. 그러나 FCSS 에서는 격자 기반 이론 및 유효 유체상 이산화탄소 저장 용량은 지역 2(주로 초임계 및 액체상)에서 높게, 지역 1(주로 초임계상)에서 중간으로, 지역 3(주로 기체상)에서 낮게 나타난다. 마지막으로 삼차원 지질 모델링과 격자 기반 몬테카를로 시뮬레이션 결과를 요약, 분석하여 최적의 이산화탄소 저장 위치를 정하거나 평가하는 네 가지 주요 기준(변수)을 결정하였다. 네 가지 주요 기준(변수)을 토대로 이산화탄소 지중 저장을 위한 지역 1, 2, 3 의 전반적인 적합성 순위가 각각 첫 번째, 두 번째 및 세 번째로 평가되었다.

주요어: 이산화탄소, 지중 저장, 대염수층, 유체상 저장 용량, 삼차원 지질 모델링, 격자 기반 몬테카를로 시뮬레이션, 확률론적 평가, 포항분지

학 번: 2013-22973